THE ZURICH ENVIRONMENTAL STUDY (ZENS) OF GALAXIES IN GROUPS ALONG THE COSMIC WEB. II. GALAXY STRUCTURAL MEASUREMENTS AND THE CONCENTRATION OF MORPHOLOGICALLY CLASSIFIED SATELLITES IN DIVERSE ENVIRONMENTS[*]

A. Cibinel[1], C. M. Carollo[1], S. J. Lilly[1], F. Miniati[1], J. D. Silverman[2], J. H. van Gorkom[3], E. Cameron[1],
A. Finoguenov[4], P. Norberg[5], Y. Peng[1], A. Pipino[1], and C. S. Rudick[1]

[1] Institute of Astronomy, ETH Zurich, CH-8093 Zurich, Switzerland; cibinel@phys.ethz.ch, marcella@phys.ethz.ch
[2] Kavli Institute for the Physics and Mathematics of the Universe (WPI), Todai Institutes for Advanced Study, The University of Tokyo, 5-1-5 Kashiwanoha, Kashiwa 277-8583, Japan
[3] Department of Astronomy, Columbia University, New York, NY 10027, USA
[4] Max-Planck-Institut für extraterrestrische Physik, D-84571 Garching, Germany
[5] Institute for Computational Cosmology, Department of Physics, Durham University, South Road, Durham DH1 3LE, UK

ABSTRACT

We present structural measurements for the galaxies in the $0.05 < z < 0.0585$ groups of the Zurich Environmental Study, aimed at establishing how galaxy properties depend on four environmental parameters: group halo mass (M_{GROUP}), group-centric distance (R/R_{200}), ranking into central or satellite, and large-scale structure density (δ_{LSS}). Global galaxy structure is quantified both parametrically and non-parametrically. We correct all these measurements for observational biases due to point-spread function blurring and surface brightness effects as a function of galaxy size, magnitude, steepness of light profile, and ellipticity. Structural parameters are derived also for bulges, disks, and bars. We use the galaxy bulge-to-total ratios (B/T) together with the calibrated non-parametric structural estimators to implement a quantitative morphological classification that maximizes purity in the resulting morphological samples. We investigate how the concentration C of satellite galaxies depends on galaxy mass for each Hubble type and on M_{GROUP}, R/R_{200}, and δ_{LSS}. At galaxy masses $M \geqslant 10^{10}\,M_{\odot}$, the concentration of disk satellites increases with increasing stellar mass separately within each morphological bin of B/T. The known increase in concentration with stellar mass for disk satellites is thus due, at least in part, to an increase in galaxy central stellar density at constant B/T. The correlation between concentration and galaxy stellar mass becomes progressively steeper for later morphological types. The concentration of disk satellites shows a barely significant dependence on δ_{LSS} or R/R_{200}. The strongest environmental effect is found with group mass for $>10^{10}\,M_{\odot}$ disk-dominated satellites, which are $\sim 10\%$ more concentrated in high mass groups than in lower mass groups.

Key words: galaxies: evolution – galaxies: groups: general – galaxies: structure – surveys

Online-only material: color figures

1. INTRODUCTION

We present the methodology used to derive structural measurements for the galaxies investigated in the Zurich Environmental Study (ZENS; Carollo et al. 2013b, hereafter Paper I). The resulting measurements are provided in the ZENS global catalog that we have published electronically with Paper I.[6]

ZENS is designed to address the question of which specific environment is most relevant for influencing the properties of different galaxy populations. Several definitions of environment have been commonly employed in the literature to study the relation between environment and galaxy evolution: the density of galaxies calculated out to a fixed or an adaptive distance (e.g., Dressler 1980; Hogg et al. 2003; Cooper et al. 2005; Baldry et al. 2006), the mass of the host group or cluster (Weinmann et al. 2006; Kimm et al. 2009), the distance from the group/cluster center (Whitmore & Gilmore 1991; Balogh et al. 1997; Lewis et al. 2002; De Propris et al. 2003; Hansen et al. 2009), or the location into larger structures such as cosmic filaments or superclusters (Einasto et al. 2007; Porter et al. 2008). Recently, the ability to separate galaxies into centrals and satellites within

their host group halos has produced mounting evidence that the environmental influence on the star-formation properties of galaxies may peak for satellite galaxies (van den Bosch et al. 2008; Peng et al. 2010, 2012; Knobel et al. 2013). There is cross-talk, however, between different definitions of environment, which may also relate to one another from a physical perspective. Therefore a key question is to identify what is the relative importance of different environmental conditions for well-defined galaxy populations of different masses, star formation activity levels, and structural/morphological properties (e.g., Blanton & Berlind 2007; Wilman et al. 2010; Peng et al. 2012; Muldrew et al. 2012; Woo et al. 2012).

In ZENS we aim to help clarify which of the many environments that a galaxy experiences has a larger impact on its evolution. We do so by using the same sample of suitably selected nearby galaxies to investigate the dependence of their properties, at fixed stellar mass, on four environment measurements: the host group halo mass, the radial segregation within the group, the large-scale density field on which the group halos reside, and the galaxy rank within its group halo, i.e., whether it is the central or a satellite galaxy within the gravitational potential of its host group. In computing our proxies for these different environments, we have attempted to minimize cross-talk between their definitions in order to better disentangle one from another of the physical conditions that galaxies experience (see Paper I).

---

* Based on observations collected at the European Southern Observatory, La Silla Chile, program ID 177.A-0680.
[6] The ZENS catalog is also downloadable from http://www.astro.ethz.ch/research/Projects/ZENS.

This paper focuses on the quantification of robust galaxy structural and morphological properties, which provide key information on the life histories of galaxies. The presence and properties of massive disks and spheroids highlight the occurrence of relatively slow and dissipative gas accretion (White & Rees 1978; Fall & Efstathiou 1980) or mergers (e.g., Toomre 1977; Barnes 1988; Schweizer et al. 1990; Naab & Burkert 2003), respectively. Inner cores or cusps (Ferrarese et al. 1994; Lauer et al. 1995; Carollo et al. 1997b, 1997a; Graham & Guzmán 2003; Graham et al. 2003; Trujillo et al. 2004; Côté et al. 2007; Kormendy et al. 2009) and tidal debris (Malin & Carter 1980, 1983; Forbes & Thomson 1992; van Dokkum 2005; Tal et al. 2009; Janowiecki et al. 2010) also trace the degree of dissipation involved in the evolution of galaxies (not surprisingly with some debate, Mihos & Hernquist 1994, 1996; Kawata et al. 2006; Feldmann et al. 2008; Hopkins et al. 2009). Bars and pseudo-bulges are smoking guns for either secular evolution processes (Kormendy 1979; Combes et al. 1990; Courteau et al. 1996; Norman et al. 1996; Wyse et al. 1997; Carollo 1999; Carollo et al. 1997c, 1998, 2001; Balcells et al. 2003; Debattista et al. 2004, 2006; Kormendy & Kennicutt 2004; Fisher & Drory 2008) or possibly for early bulge formation through instabilities in the proto-disks (Immeli et al. 2004; Carollo et al. 2007; Dekel et al. 2009a, 2009b). A robust determination of galaxy morphology is therefore essential for understanding whether this is linked to any of the environmental conditions above, how precisely it relates to the occurrence, enhancement or cessation of star formation activity, and for pinning down which physical processes drive galaxy evolution.

Determining galaxy structure is, however, notoriously a difficult task. Visual morphological classification is still a widely adopted method (e.g., Lintott et al. 2008; Nair & Abraham 2010a), despite its subjectivity and failure to provide quantitative measurements for different components, which are necessary to trace galaxy assembly over cosmic time. For these reasons numerous publications have been devoted to the development of methods and software for the automated quantification of structure on large galaxy samples. There are a number of approaches to the problem that can be broadly divided into two categories: those which employ parametric descriptors for the galaxy morphology, namely a set of analytical profiles used to model the bulge, disk, or bar component (e.g., Simard et al. 2002; Peng et al. 2002; de Souza et al. 2004), and those that instead use the observed properties of the light distribution, such as the degree of asymmetry, isolation of bright pixels, or decompositions into a set of basis functions (e.g., Abraham et al. 1996; Conselice 2003; Refregier 2003; Lotz et al. 2004; Scarlata et al. 2007). The two methods have different strengths. Parametric decomposition is useful to obtain measurements of characteristic sizes and to have an estimate of the relative importance of the bar, disk, and bulge components; it also easily includes the effects of seeing. Non-parametric estimators well describe the inhomogeneities in the light distributions of real galaxies, which typically display irregular, non axis-symmetric features generated by recent star-formation, dust, or galaxy interactions.

Both parametric and non-parametric measurements suffer from a number of observational biases, however, which must be corrected in order to perform comparisons between galaxies of different properties, and observed in different conditions. In particular, in ground-based surveys, the effect of atmospheric seeing is one of the major complications. Several studies have shown the strong impact of the seeing on the photometric and structural properties of galaxies, not only in the inner regions of galaxies, but also out to radii corresponding to several FWHM of the point-spread function (PSF; e.g., Schweizer 1979; Franx et al. 1989; Saglia et al. 1993; Trujillo et al. 2001; Graham 2001).

Another factor that affects the derivation of structural parameters is the inclination angle at which a galaxy is observed. The overlap, in projection, of multiple subcomponents, as well as physical factors such as the non-uniform distribution of inter-stellar dust—which causes a higher attenuation of short-wavelength light in the central regions of edge-on galaxies than in similar face-on galaxies (e.g., Driver et al. 2007; Shao et al. 2007)—can substantially bias the measurements of sizes, bulge-to-disk ratios, concentration, and even stellar masses (e.g., Maller et al. 2009; Graham & Worley 2008; Bailin & Harris 2008).

Finally, the background sky makes the detection of faint components difficult, a fact that introduces severe biases in the measurements of the galaxy properties, especially magnitudes and sizes (e.g., Disney 1976; Impey & Bothun 1997). The strength of the bias depends on galaxy size, inclination, and stellar light profile. Although a number of widely used measurement techniques, such as the computation of Kron aperture fluxes (Kron 1980) or the extrapolation of model galaxy surface brightness profiles (Sersic 1968), can help recover light below the isophotal limit, significant systematic biases remain in the low surface brightness regimes specific to each survey (e.g., Graham et al. 2005; Cameron & Driver 2007, 2009; Häussler et al. 2007).

In ZENS we attempt to correct, when possible, all measurements of galaxy structure for systematic biases as a function of PSF-size, and also galaxy magnitude, size, axis ratio, and radial shape of the light profile. We also quantify the size of systematic biases in regimes of parameter space where the (statistical) recovery of the intrinsic information is not achievable, e.g., at small galaxy sizes and low surface brightnesses. We also stress that in ZENS each galaxy is handled individually until self-consistent and both quantitatively and visually checked accurate measurements are achieved. This enables ZENS to tackle complementary questions regarding the galaxy-environments relationship relative to larger but less-detailed galaxy samples.

The paper is organized as follows. In Section 2, we briefly review the specifications and definitions for the four environments under scrutiny in ZENS. We then devote the first part of the paper to an overview of the structural measurements carried out on the ZENS galaxy sample. These measurements include isophotal analyses and bar detection/quantification (Section 3), analytical surface brightness fits and bulge+disk decompositions (Section 4), and derivation of non-parametric structural indices (concentration, Gini, asymmetry, M_{20}, smoothness; Section 5). In Section 6, we thoroughly investigate the sources of error in these measurements and derive a correction scheme that recovers the intrinsic structural parameters. In Section 7, we present the morphological classification of the ZENS galaxies based on a quantitative partition of the structural parameter space in regions that are associated with elliptical, bulge-dominated disks, intermediate bulge-to-total ratio disks, late-type disks, and irregular galaxies. In the same section, we also discuss the statistics of the structural properties for the various morphological classes. In Appendix A we describe in detail the data reduction and photometric calibration of the ESO B and I Wide Field Imager (WFI)/2.2 m imaging data for the ZENS groups that are introduced in Paper I. Appendices B and C present additional details on the tests performed on the analytical surface-brightness fits and supplementary information for the derivation of the corrections for the

structural parameters. Stamp images for galaxies in the different morphological classes are found in Appendix D. In the final part of the paper we use the corrected structural measurements to study, at constant stellar mass, the concentration of satellite galaxies as a function of Hubble type and environment (Section 8). We summarize the paper in Section 9.

This second ZENS publication is complemented by a companion paper (Cibinel et al. 2013, hereafter Paper III), in which we present the spectrophotometric properties of our galaxy sample and to which we refer for details on the derivation of, e.g., the galaxy spectrophotometric types, star formation rates, and stellar masses that we use in this and other ZENS papers.

The following cosmological parameters are adopted in all the ZENS publications: $\Omega_m = 0.3$, $\Omega_\Lambda = 0.7$, and $h = 0.7$. Unless otherwise specified, magnitudes are in the AB system and galaxy sizes are *semi-major* axis measurements. All derived luminosities are corrected for Galactic extinction using the maps of Schlegel et al. (1998).

2. A BRIEF SUMMARY OF ZENS

2.1. Data and Sample

ZENS is based on a sample of 1484 galaxies,[7] members of 141 galaxy groups extracted from the 2-degrees Field Galaxy Redshift Survey (2dFGRS; Colless et al. 2001, 2003), and specifically from the Percolation-Inferred Galaxy Group (2PIGG) catalog (Eke et al. 2004a). The 141 ZENS groups are a random selection of 2PIGG groups that are found in the very thin redshift slice $0.05 < z < 0.0585$ and have at least 5 confirmed members, down to a magnitude $b_J = 19.45$. New *B*- and *I*-band images were acquired for these groups with the WFI camera mounted at the Cassegrain focus of the MPG/ESO 2.2 m Telescope at La Silla over several observing runs between 2005 and 2009 (see Paper I for details). The data reduction and photometric calibration of these WFI data is reported in Appendix A. This paper describes in detail the structural analysis that we have performed on these WFI *B* and *I* images.

2.2. The Four Environments Investigated in ZENS

For each ZENS galaxy, Paper I discusses and publishes four estimates of environment: the group halo mass, the distance from the center of the group, the rank within the group (i.e., whether the galaxy is the central or a satellite), and the location on the large-scale structure (LSS). In particular:

1. Group masses (M_{GROUP}) are derived from the total group luminosities by assuming a mass-to-light ratio calibrated with mock catalogs (Eke et al. 2004b).
2. The ranking of galaxies in centrals and satellites factors in the errors on the galaxy stellar masses and includes a test of self-consistency requiring that a bona-fide central galaxy must, simultaneously, be consistent with being the most massive galaxy of the group, be located within a projected distance $<0.5R_{200}$ from the mass-weighted center of the group (with R_{200} the characteristic size of the group, as defined in Paper I), and have a relative velocity within one standard deviation from the group velocity.
3. The centers of the groups, on which the projected radial positions of satellite galaxies within the groups rely, are identified with the locations of the central galaxies. We

operationally divide the ZENS group sample into *relaxed* and *unrelaxed* groups, depending on whether a bona-fide central galaxy can be found according to the prescription above. In Paper I, we discuss the observational biases that may hamper the identification of the central galaxy in groups that are, in fact, dynamically relaxed. We therefore use our group classification scheme mostly to test that our results are not affected by the inclusion/exclusion of the unrelaxed groups from our studies, although we keep an eye on the possibility that there may be a physical origin, related to the dynamical evolution of the host groups, for differences observed in otherwise similar galaxies that inhabit the two classes of groups.

4. The LSS density at the ZENS group locations is defined using an Nth nearest-neighbor analysis that adopts the groups (not the galaxies) as the tracers of the LSS density. Specifically, we define $\delta_{LSS} = ((\rho_{LSS}(z) - \rho_m)/\rho_m)$ with $\rho_{LSS}(z)$ as the density of 2dFGRS groups in a projected circular area defined by the comoving distance of the 5th nearest-neighboring group around the ZENS group, and ρ_m is the mean projected density calculated over the global 2dFGRS area at the given redshift. Our choice results in identical δ_{LSS} values for all galaxy members of any given group and avoids the problems that are associated with using Nth-nearest neighboring galaxy algorithms (see Paper I and also Peng et al. 2012; Woo et al. 2012).

2.3. Galaxy Stellar Mass Completeness Limits for ZENS

In Paper III, we discuss the mass completeness limits of ZENS, which are determined by the 2dFGRS apparent magnitude selection. The strongest constraints are set by passively evolving galaxies, which have the larger mass-to-light ratio, for which the 85% completeness is reached above $10^{10}\,M_\odot$. This is the mass completeness threshold that we adopt for passive elliptical and S0 galaxies. Progressively more active star-forming galaxies have progressively lower mass completeness thresholds, with strong star-forming galaxies mass complete at $10^{9.2}\,M_\odot$ (see Paper III). Given the statistical mix of spectrophotometric types in the different morphological bins, the mass completeness thresholds of $10^{9.93}\,M_\odot$, $10^{9.78}\,M_\odot$, and $10^{9.55}\,M_\odot$ are statistically adequate, for, respectively, the morphological classes of bulge-dominated spirals, intermediate bulge-to-total disk galaxies, and late-type disk (or irregular) galaxies.

3. QUANTIFICATION OF GALAXY STRUCTURE. I. AN ISOPHOTAL ANALYSIS

Surface brightness profiles and isophotal parameters were obtained with the IRAF ELLIPSE routine. This well-tested algorithm fits the intensity at a given radius with the Fourier series $I(\theta) = I_0 + \sum(A_n \cos n\theta + B_n \sin n\theta)$ (Jedrzejewski 1987). Here, I_0 is the mean intensity within the isophote and A_n, B_n the high harmonic coefficients that quantify isophotal deviations from perfect ellipticity. We truncated the series after the fourth order so that, for each isophote, the fits return the mean intensity, position angle (PA), ellipticity (ϵ), and the amplitude of the fourth-order coefficients A_4 and B_4. The coefficient A_4 has been extensively used in the past to measure "boxiness" ($A_4 < 0$) and "diskyness" ($A_4 > 0$) of the isophotes (e.g., Bender et al. 1988; Franx et al. 1989; Naab et al. 1999).

In running ELLIPSE, we allowed the position angle and ellipticity to vary freely with radius, and we limited wanderings of the isophotal center to within three pixels from the center

---

[7] Note that only 1455 galaxies are listed as members of the 141 2PIGG groups; however, 29 of these single-entries are actually galaxy pairs/triplets, for which we measure the individual properties of both galaxies.

of the innermost isophotes. The PA and ellipticity determined by the SEXTRACTOR algorithm (Bertin & Arnouts 1996) served as initial guesses for the ELLIPSE algorithm. The semi-major axis of adjacent isophotes was increased in logarithmic radial steps of 0.1 in order to increase the signal-to-noise ratio (S/N) when measuring the external isophotes. We allowed the code to perform a two iteration 3σ clipping of the discrepant pixels during the fits and terminated the fitting procedure when >50% of the pixels in a given step of the calculation were flagged as discrepant.

The procedure was applied independently to the I and B images and returned independent surface brightness profiles in each of the two passbands. We also derived surface brightness profiles in the B filter using the isophotal parameters derived from the I images; this returned more reliable surface brightness profiles also at the shorter wavelength for those galaxies whose B light distributions were too irregular (because of dust absorption and star formation knots) for a reliable measurement directly on the B images.

3.1. Bar Identification and Quantification of Bar Strength

Changes in the radial profiles of PA and ellipticity were used as the first diagnostics to identify bars in the (disk) galaxies. The presence of a bar produces a characteristic signature on the isophotes shapes: within the bar region, the ellipticity increases smoothly to a maximum value with almost constant PA and then drops abruptly at the end of the bar where the PA also changes substantially.

We inspected the I-band ellipticity and position angle radial profiles of the disk galaxies in our sample (S0 and later, see Section 7 for the definition of the morphological types). We classified a disk galaxy as barred if its ellipticity grows to an absolute maximum greater than 0.2 and shows a variation in ellipticity and PA greater than 0.1 and $10°$, respectively. In the bar region, we furthermore request that the PA profile is flat within $\pm20°$. The size of the bar, a_{bar}, was defined to be the semi-major axis associated with the maximum value of the ellipticity profile, subject to the condition that it had to be at least twice the FWHM of the PSF, which is typically $\sim1''$. Note that galaxies with bar sizes smaller than this threshold are not considered barred systems. Therefore, our final sample of barred disks provides a conservative lower limit to the total number of such galaxies in the entire sample. Illustrative examples of the isophotal parameters profiles for a random selection of ZENS galaxies classified as barred and non-barred are shown in Figure 1.

The above mentioned criteria are widely used in the search for bars (e.g., Knapen et al. 2000; Menéndez-Delmestre et al. 2007 or Sheth et al. 2008) and are shown to provide robust results, but they can fail in identifying a bar if, e.g., the bar has a similar PA to that of the disk (see, e.g., Menéndez-Delmestre et al. 2007). For this reason, we also visually inspected all the disk galaxies and those that clearly showed a bar structure—and had an ellipticity profile consistent with it but no drop in PA—were included in the barred sample as well. Combining the ELLIPSE fitting method with the visual validation, we identified a clear bar signature in 148 disk galaxies.

To quantify the bar strength, we used the definition of Abraham & Merrifield (2000), i.e.,

$$f_{\text{bar}} = \frac{2}{\pi}\left[\arctan\left(\frac{b}{a}\right)_{\text{bar}}^{-\frac{1}{2}} - \arctan\left(\frac{b}{a}\right)_{\text{bar}}^{+\frac{1}{2}}\right],\qquad(1)$$
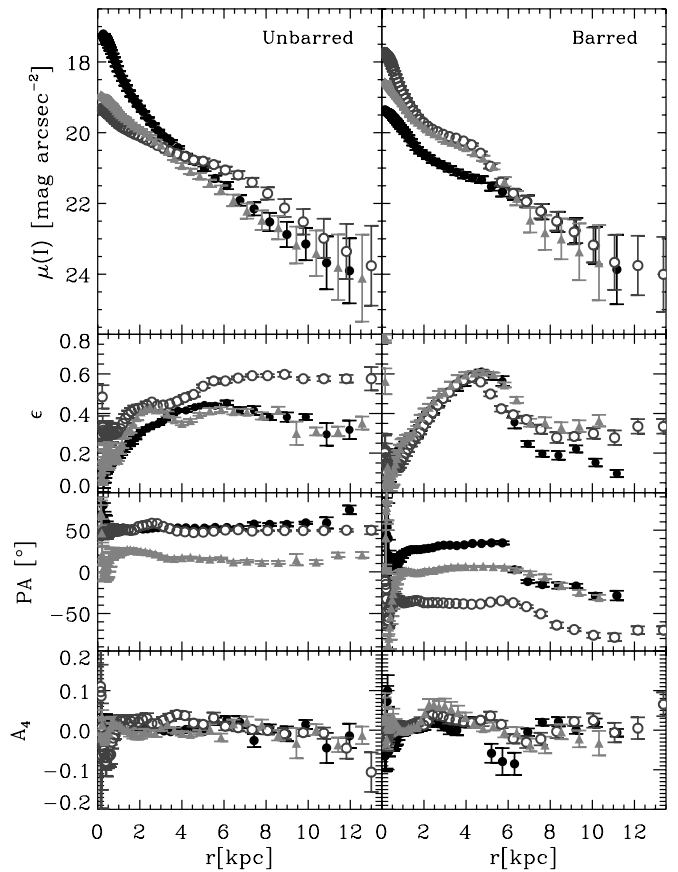

Figure 1. From top to bottom, the panels show the radial profiles of I-band surface brightness, ellipticity, position angle, and the high-order Fourier coefficient A_4 for three examples of ZENS disk galaxies classified as non-barred (left) and barred (right). Different symbols and gray shades are used to distinguish the profiles for the three individual galaxies.

where $(b/a)_{\text{bar}}$ is the intrinsic axial ratio of the bar. The bar strength ranges from zero to unity for unbarred galaxies and infinitely strong bars, respectively. The intrinsic axial ratio was derived from the observed one using the transformation of Abraham et al. (1999), i.e.,

$$\left(\frac{b}{a}\right)_{\text{bar}}^2 = \frac{1}{2}(X - \sqrt{X^2 - 4}),\qquad(2)$$

with

$$X = \sec^2 i\,[2\cos^2\phi\sin^2\phi\sin^4 i$$
$$+ (b/a)_{\text{inner}}^2(1 - \sin^2\phi\sin^2 i)^2$$
$$+ (b/a)_{\text{inner}}^{-2}(1 - \cos^2\phi\sin^2 i)^2]\,.$$

Here, i is the inclination angle obtained from the minor and major axis of the galaxy considered as a whole ($i = \arccos(b/a)_{\text{out}}$), $(b/a)_{\text{inner}}$ is the observed axis ratio of the bar, and ϕ is the twist angle between the bar and galaxy semi-major axis. For our sample, we computed $(b/a)_{\text{inner}}$ at the bar semi-major axis a_{bar} and we used the values of ellipticity and PA obtained from SEXTRACTOR (Bertin & Arnouts 1996) to calculate $(b/a)_{\text{out}}$ and ϕ.

Figure 2 shows the distribution of bar strength and bar sizes measured in the ZENS samples of bulge-dominated galaxies (including both S0 and bulge-dominated spirals), intermediate-type, and late-type disk galaxies. The median bar strength mildly
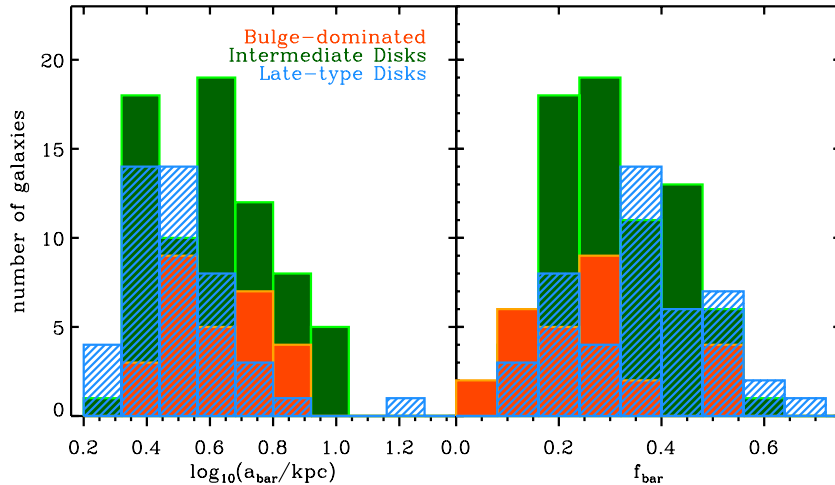
Figure 2. Distribution of bar semi-major axes (left) and strengths (right) for the ZENS galaxies which are classified as barred. Histograms are colored differently according to the disk galaxy type hosting the bar: dark gray (orange in the online version), S0/bulge-dominated spirals; gray (green), intermediate-type disks; black (blue), late-type disks.

(A color version of this figure is available in the online journal.)

increases with Hubble type, changing from a value of $\langle f_{bar} \rangle = 0.24^{+0.01}_{-0.02}$ for S0 or bulge-dominated spirals to $\langle f_{bar} \rangle = 0.31^{+0.02}_{-0.01}$ for intermediate-type disks and $\langle f_{bar} \rangle = 0.36^{+0.02}_{-0.02}$ for late-type disk galaxies. We also find a decrease in median bar size from late-type to early-type disks: $\langle a_{bar} \rangle = 3.95^{+0.44}_{-0.20}$ kpc for S0 and bulge-dominated spirals, $\langle a_{bar} \rangle = 3.78^{+0.31}_{-0.14}$ kpc for intermediate-type disks, and $\langle a_{bar} \rangle = 2.95^{+0.25}_{-0.07}$ kpc for late-type disks. For both the bar size and strength a Kolmogorov-Smirnov test rejects a common parent distribution between bulge-dominated galaxies and late-type disks with a probability of 99%. The correlation between bar properties and Hubble types (which could be a reflection of a correlation with galaxy stellar mass, e.g., Sheth et al. 2008; Cameron et al. 2010; Nair & Abraham 2010b) has been investigated in several works in the literature whose results are consistent with our measurements. For example, a weakening of bars in early type galaxies is reported by Laurikainen et al. (2007), Buta et al. (2005), Barazza et al. (2008), Aguerri et al. (2009), and an increase in bar size in early- relative to late-type disks is found by Erwin (2005).

4. QUANTIFICATION OF GALAXY STRUCTURE. II. PARAMETRIC CHARACTERIZATION

Two-dimensional fits to the surface-brightness distributions of all ZENS galaxy images were carried out with the Galaxy IMage 2d (GIM2D) software package (Marleau & Simard 1998; Simard et al. 2002). We used a single Sérsic profile to describe the total galaxy light distribution, i.e., $\Sigma_b = \Sigma_e \exp\{-k_n[(r/r_{1/2})^{1/n} - 1]\}$, where Σ_e is the surface intensity at the half-light radius $r_{1/2}$. The value of the parameter k_n is such to ensure that the flux within $r_{1/2}$ is half of the total flux and it is approximated to $k_n = 1.9992n - 0.3271$ (e.g., Caon et al. 1993; Graham & Driver 2005).

For the ZENS galaxies that are not classified as ellipticals (in Section 7), we also performed two-component bulge+disk decompositions of the two-dimensional galaxy light distributions. For this purpose we assumed a Sérsic profile for the bulge and a perfectly exponential disk represented by $\Sigma_d = \Sigma_0 \exp(-r/h)$, with Σ_0 as the central surface intensity and h as the disk scale length. Pure exponential models with no bulge component were furthermore generated for galaxies classified as late-type disks (see again Section 7). Table 1 summarizes the

range of values between which the model parameters were allowed to vary.

GIM2D convolves the theoretical models with the PSF before fitting them to the galaxy images. We modeled the PSF of each ZENS group with a two-dimensional Gaussian having FWHM equal to the mean of the full-widths measured on several unsaturated stars over the ZENS fields. A single PSF was used for a whole ZENS field as the WFI PSF varies only slightly across the field of view of the camera, showing in particular a mild ~10% increase of the PSF FWHM very close to the edges of the CCDs (as tested on SExtractor sources with stellarity class >0.9 in all ZENS fields). Due to statistical scatter and S/N variations, errors introduced by applying a correction for this effect are comparable to or even marginally larger than those resulting from the adoption of a single PSF for each field. Larger PSF variations in ZENS are instead observed between different fields (i.e., pointings); in this case, the PSF can change by as much as 0.6–0.7 arcsec (see Figure 24). This effect is taken into account not only during the model fitting, but also when applying the correction scheme that we develop in Section 6.

During the fitting procedure, the code was allowed to recompute the initial parameters from the image moments and to fit the sky background level in each individual postage stamp galaxy image; the postage stamps were sized proportionally to the SExtractor Petrosian radius of the galaxies, and set to be equal to three times the Petrosian radius. On a set of simulations calibrated on the GEMS survey (Rix et al. 2004), fixing the background to a locally defined value during the GIM2D fit was shown to improve the performances for low surface brightness galaxies (Häussler et al. 2007). Our alternative approach was to enable the local sky subtraction and to quantify any systematic bias in the GIM2D fits using a large set of artificial galaxy images that are specifically tailored to the ZENS observations (Section 6). The sky pixels were identified as those pixels in the galaxy postage stamps that were located outside an aperture equal to 1.5 times the SExtractor Petrosian radii of the galaxies. Bright star-forming clumps were masked during the fitting procedure. Finally, although GIM2D offers an option to correct for the effects of the disk optical thickness—which consists in adding to the disk total magnitude a geometric factor $2.5 \times \log(a/b)$, where a/b is the axis ratio—we decided not to use this feature and disks were assumed to be optically thin in

Table 1
Range of Allowed Values for the Parameters of the GIM2D Fits

Parameter	Double Component Fits			Single Sérsic Fits			Pure Exponential Fits		
	Initial Guess	min	max	Initial Guess	min	max	Initial Guess	min	max
$m_{T,B}/m_{T,I}$ (mag)	18/16.5	21.5/20	13/12	18/16.5	21.5/20	13/12	18/16.5	21.5/20	13/12
B/T	0.5	0	1	1	1	1	0	0	0
$R_{e,\text{bulge}}$ (kpc)	2.3	0.5	20	2.3	0.5	30	...	...	...
ϵ_{bulge}	0.5	0	0.7	0.5	0	1.0	...	...	...
ϕ_{bulge} (°)	45	−180	180	45	−180	180	...	...	...
h (kpc)	2.3	0.5	20	...	...	...	2.3	0.5	20
i_{disk} (°)	45	0	90	...	...	...	45	0	90
ϕ_{disk} (°)	45	−180	180	...	...	...	45	−180	180
Δx (pixels)	0	−2	2	0	−2	2	0	−2	2
Δy (pixels)	0	−2	2	0	−2	2	0	−2	2
n	2.1	0.2	10	2.1	0.2	10	...	...	...

Notes. Permitted ranges for the variation of model parameters used in the GIM2D fits. From top to bottom: total galaxy magnitude in B and I bands, bulge-to-total ratio (B/T), bulge half-light radius, bulge ellipticity, bulge position angle, disk scale length, disk inclination angle, disk position angle, x and y galaxy center offset from the SEXTRACTOR center (further refined by using the IRAF imcntr task), and Sérsic index.

order to fit the actual observed light distribution without a prior assumption about the dust distribution.

4.1. Details of the Variable-n Single Sérsic Fits and n = 1 Pure Exponential Fits

To be able to detect color gradients, for the variable-n single Sérsic fits as well as for the $n = 1$ pure exponential models, the B- and I-band images were fitted independently without imposing the structural parameters of one filter to the other band. The position angles and ellipticity derived from the B- and I-band images agree well, with differences being limited to 15° and 0.15, respectively. We find differences that are larger than this in only 2% of the galaxies with a maximum change in ellipticity ∼0.2 and a maximum change in position angle ∼30°. Generally speaking, we thus conclude that the single component fits are robust and strong twists between the B- and I-band isophotes are not a problematic issue when performing independent fits for the two passbands.

To verify the validity of the GIM2D single-component fits, we ran the task ELLIPSE on all the GIM2D models, keeping the isophotes fixed at the radii, position angle, and ellipticity of the ELLIPSE fits to the real galaxy images described in Section 3. The comparison between the total magnitudes and the ELLIPSE profiles derived for the GIM2D models and those derived for the real galaxies, as well as the inspection of the residual images between the GIM2D models and the real galaxies, enabled us to reject unphysical GIM2D models.

Overall, we could obtain reliable Sérsic fits for 96% of the B-band and I-band images. A similar fraction of successful fits is obtained for the pure exponential models of late-type disks (95%). The distribution of stellar masses (from Paper III), sizes, and morphological types for the 4% of ZENS galaxies with no single Sérsic fits is shown in Figure 28 and Table 5 of Appendix B. In this appendix we also present, for the subset of ZENS galaxies for which the information is publicly available from the NYU-VAGC (Blanton et al. 2005), a comparison of our estimates of the Sérsic parameters with those published in this other catalog. The comparison shows a good agreement between our *uncorrected* measurements and the previously published data. However, we show below that, in some regimes of parameter space, these measurements require further corrections to be cleaned by residual observational biases, indicating

that measurements in the quoted and other public catalogs necessitate similar attention.

4.1.1. Comparison between Single-component B- and I-band Models

The comparison between the structural parameters obtained from the single Sérsic fits with variable-n in the two available passbands is shown in the left and central plots of Figure 3. The single component fits in the two different pass-bands generally provide consistent measurements with little scatter. In particular, half-light radii measured in the two pass-bands are in very good agreement with each other. The I-band fits, however, result in slightly steeper profiles: at this wavelength, galaxies have n indices, which are bigger by 17% with respect to those measured in the B-band. This is not unexpected in an "inside-out" galaxy formation process, as younger stellar populations at large radii would lead to this effect.

Another difference is observed between I- and B-band disk scale lengths of large late-type galaxies, as derived from the pure exponential fits (right-hand side plot in Figure 3): disk scale lengths h derived from $n = 1$ fits to relatively large late-type disk galaxies are smaller at the longer wavelength by ∼10%–20%. We have checked that the I magnitude distribution of these late-type disks is not biased toward faint values that would raise concerns on surface brightness detections. As we show in detail in Section 6.3, the I-band GIM2D sizes that we derive for relatively large $n \sim 1$ galaxies are not severely affected by observational biases. We thus interpret this result again as mostly due to a genuine color gradient in large late-type disks. Note that the average difference in the I and B disk scale lengths in the pure exponential fits of late-type disk galaxies is consistent with a similar difference reported for a sample of local late-type galaxies by de Jong (1996) and Barden et al. (2005).

Summarizing, the larger h values from $n = 1$ fits and smaller Sérsic indices from variable-n fits of late-type disks in the B band relative to the I band are consistent with being the joint result of the segregation of young stars in the galaxy outskirts and, also, of light absorption from the center of the galaxies by interstellar dust, as discussed in a number of observational and theoretical works (e.g., Byun et al. 1994; Beckman et al. 1996; Cunow 2001; Möllenhoff et al. 2006).

The more pronounced variation of disk scale length in the pure exponential fits with respect to the half-light radius in the Sérsic
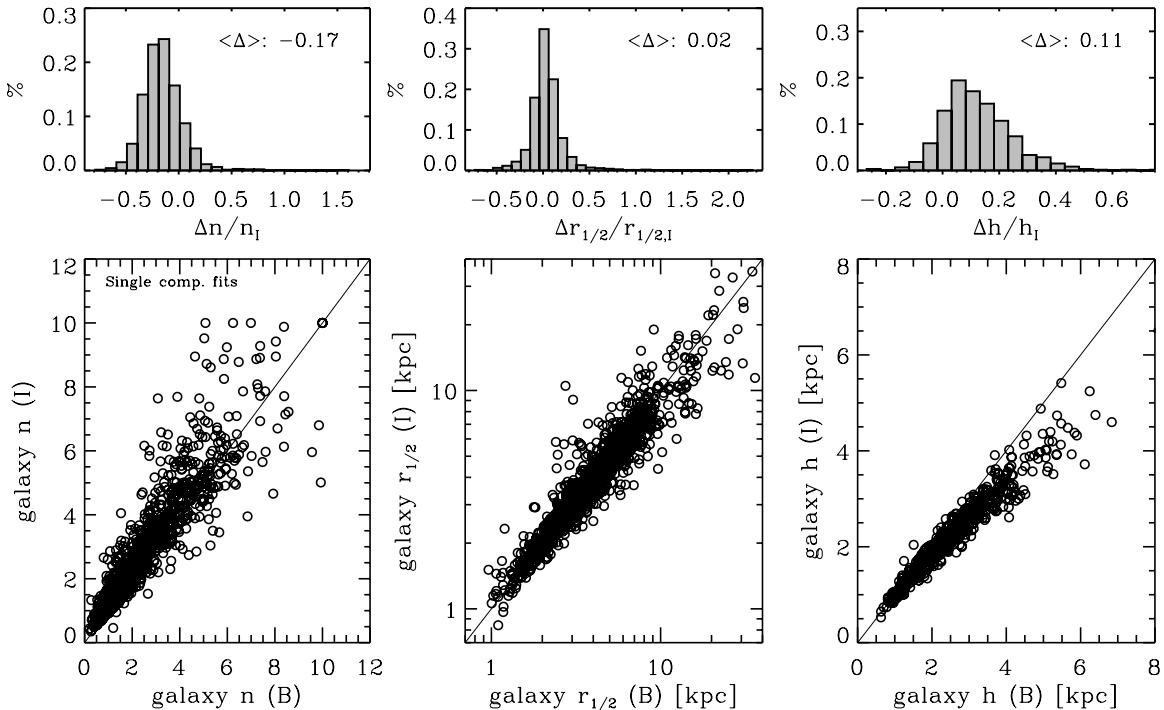
Figure 3. Comparison between half-light radii (left) and Sérsic indices (center) obtained from the GIM2D single Sérsic fits to the *I*- and *B*-band data. The upper histograms show the distributions of the parameter differences in the two filters (*B*-band minus *I*-band), normalized to the *I*-band measurements. The median value of the structural variation between the *I* and *B* bands is given inside these upper panels. Values are presented for the *uncorrected* GIM2D measurements, i.e., before applying our correction scheme for systematic biases described in Section 6.3. The rightmost panels show the comparison between the disk scale lengths obtained from the pure exponential fits in the two pass-bands to galaxies classified as late-type disks. In the *I* band, variable-*n* Sérsic fits result in ~17% larger *n* values than those measured for the same galaxies in the *B* band. Furthermore, the *I*-band scale lengths of $n = 1$ pure exponential fits to relatively large late-type disks are ~10%–20% smaller than those derived from similar fits to the *B*-band images.

fits for the late-type galaxies can be readily understood. Whereas in the variable-*n* single Sérsic fits, a lower central concentration of light can be modeled with a smaller value of the Sérsic index *n* and a relatively small change in the effective radius, fixing the index to $n = 1$ in the pure exponential fits forces an increase of the characteristic scale length in order to obtain a milder radial decline in surface brightness in the *B* band. This is consistent with the fact that the largest variation in *n* values between the *B*- and *I*-band variable-*n* Sérsic fits to late-type disks are observed for those galaxies which also have the largest variations in scale length *h* when fitted with an $n = 1$ profile.

Finally we note that a self-consistent correction for dust effects would require radiative transfer simulations of the light scattered and re-emitted by the dust grains (e.g., Byun et al. 1994; Cunow 2001; Tuffs et al. 2004); this is beyond the scope of this paper. Moreover it remains difficult to disentangle dust effects from genuine radial segregation in the stellar populations. For these reasons, instead of attempting a correction for dust absorption, we choose the empirical approach of employing the less dust-sensitive *I*-band data as the fiducial reference for our structural measurements and to discuss separately possible dust-reddening effects when relevant, e.g., in studying color profiles and star formation rates (see Paper III).

4.2. Details of the Bulge+Disk(+Bar) Decompositions

Double component, bulge+disk decompositions were also performed on both the *B*- and *I*-band images of all galaxies which are not classified as ellipticals or irregulars (Section 7). For the *I* band, our reference filter for structural measurements, no a priori constraints on the bulge and disk parameters were imposed during the fitting procedure, except for the wide limits

listed in Table 1. In the *B* filter, each galaxy was instead fitted in four different ways: (1) by performing a separate decomposition to the *B* band letting the structural parameters completely unconstrained (unconstrained model fit, hereafter *UF*), (2) by fixing the disk and bulge position angles, ellipticity and inclination to those of the *I* band (constrained model fit number one, hereafter *C*1), (3) by also fixing the bulge half-light radius and Sérsic index *n* (constrained model *C*2), and (4) by keeping all the parameters tied to those of *I* band except for the B/T and total flux (constrained model *C*3). In all the models we allowed a maximum wandering of 2 pixels for the disk and bulge components from the SEXTRACTOR center.

There are clear advantages and disadvantages in performing either independent or constrained fits to the two bands: by fixing the *B*-band structural parameters to the *I* band, one ensures that bulge and disk colors are measured consistently over the same regions; this however prevents the detection of structural differences and color gradients. For this reason we decided to adopt a mixed approach to determine the bulge and disk parameters to the *B* band.

First, not all models returned by the GIM2D fits are physically meaningful bulge+disk decompositions. We hence adopted a filtering scheme to reject unreliable or unphysical models to all GIM2D models, i.e., the fiducial *I*-band models for each galaxy, and the four versions of the *B*-band models. Our filtering scheme is described in Appendix B.

We then followed a quantitative procedure to select, amongst the physically valid alternatives for the *B* bulge+disk fits for each galaxy, our fiducial (i.e., in our judgment, the most reliable) bulge+disk *B*-band decomposition. In brief, we required that all *B*-band disk and bulge fits always have bulge and disk position angles, disk inclinations, and bulge axis ratios
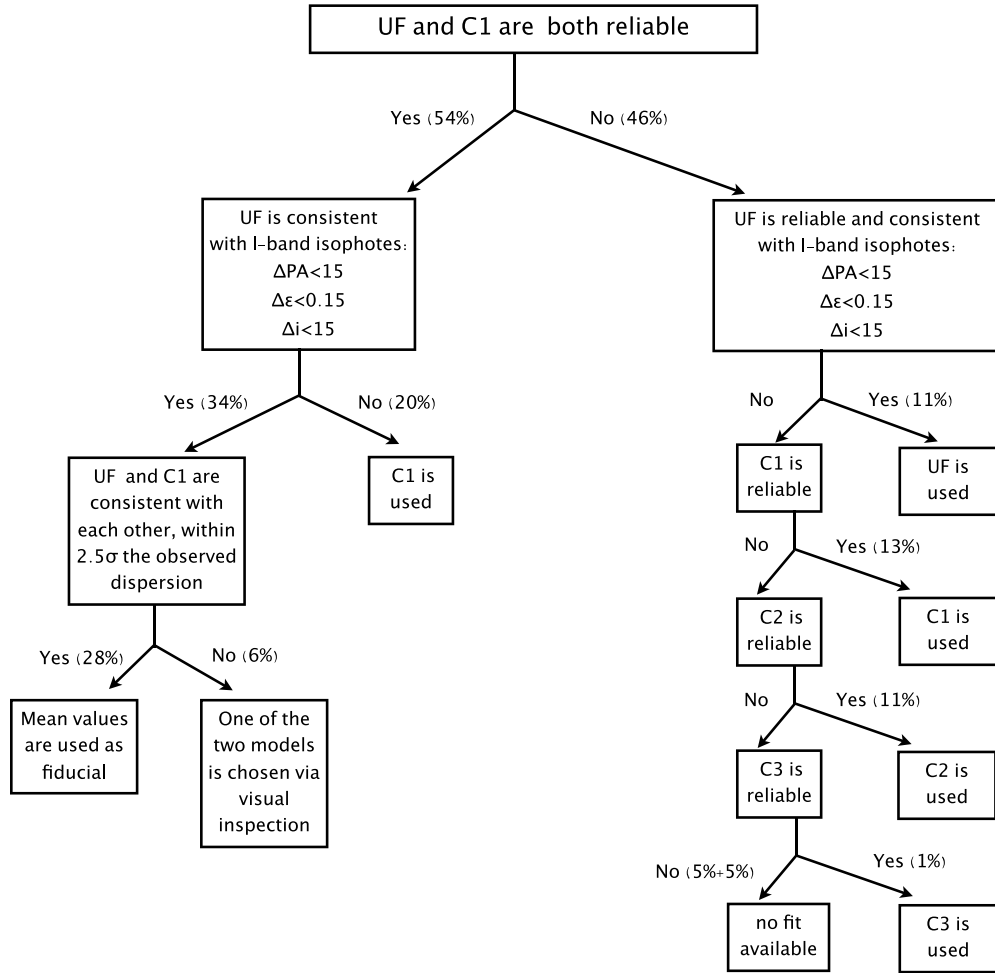
Figure 4. Flow chart describing our scheme for selecting the fiducial GIM2D bulge+disk B-band models. UF, $C1$, $C2$, and $C3$ are the four fits that we performed on the B images, respectively by keeping the B bulge and disk parameters completely unconstrained, fixing their position angles and ellipticities to those derived from the I-band fits, adding to the I-band-fixed parameters the bulge half-light radius and Sérsic index n, and finally by tying to the I-band values also the B disk scale lengths. Numbers in parentheses give the fraction of B-band bulge+disk decompositions that fall in each category; note that sub-branches sum up to the fractions listed on the previous level. The fractions refer to disk galaxies with a detected bulge component in the ZENS sample, i.e., to S0, bulge-dominated spirals, and intermediate-type disks. The two numbers for the models with no bulge+disk decomposition in the B band give the fraction of galaxies for which either an I-band fit is available but no good B-band fit can be achieved (5%), or the fraction of galaxies for which neither an I nor a B bulge+disk decomposition can be achieved (5%).

consistent, within a sensible range,[8] to those of the I-band fits. When this was achieved with unconstrained fits to the B-band images, these unconstrained fits were retained as a fair description of the B bulge+disk decompositions. This choice maximizes the detection of possible wavelength-dependent structural differences and color gradients. For galaxies in which such a consistency requirement was not achieved with the unconstrained B fits, we adopted as fiducial B-band fits those which satisfied such requirement with the minimum number of B parameters tied to the I-band fit parameters (i.e., in order of priority, the $C1$, $C2$, and $C3$ fits).

In cases where both the $C1$ and UF models were in principle both potentially good representations of the bulge+disk properties of considered galaxy, we applied the following decision scheme: if the two models gave disk and bulge size, B/T and Sérsic indices within 2.5σ of the dispersion measured around the identity from all the model falling in this latter category, then both models were validated as reliable, and we adopted as our fiducial bulge+disk parameter estimates the mean of the

structural parameters returned by these two fits. If these two fits returned discrepant values, both were inspected and a judgment was made on which model to use, on the basis of the residual images and the difference in total magnitude between the galaxy and the model. Only 6% of the bulge+disk B fits needed this further visual validation. This entire procedure is schematized in Figure 4.

It is important to notice that while disk scale length and bulge-to-total ratios are quite consistently returned by all four fits to the B images, bulge sizes and Sérsic indices show much larger variations from one fit to the other. This is illustrated in Figure 5, where we compare the different measurements obtained for the B-band in the four cases UF, $C1$, $C2$, and $C3$. The robust dispersion around the identity line in the four fits is ~0.2 kpc and 8% for h and B/T, and ~0.6 kpc and 1.6 for the bulge half-light radii and Sérsic indices n, respectively. Especially for the bulge n values, models with the isophote's position constrained and unconstrained can indeed provide very different results. Similar conclusions on the reliability of the bulge and disk parameters are drawn from tests on simulated galaxies which we discuss in Section 6.6.

Not surprisingly, the success rate for the bulge+disk decomposition is lower than the one for the single component. The

---

[8] The allowed ranges of variations for B and I bulge and disk position angles, disk inclination angles and bulge ellipticities were respectively $15°$, $15°$, and 0.15.
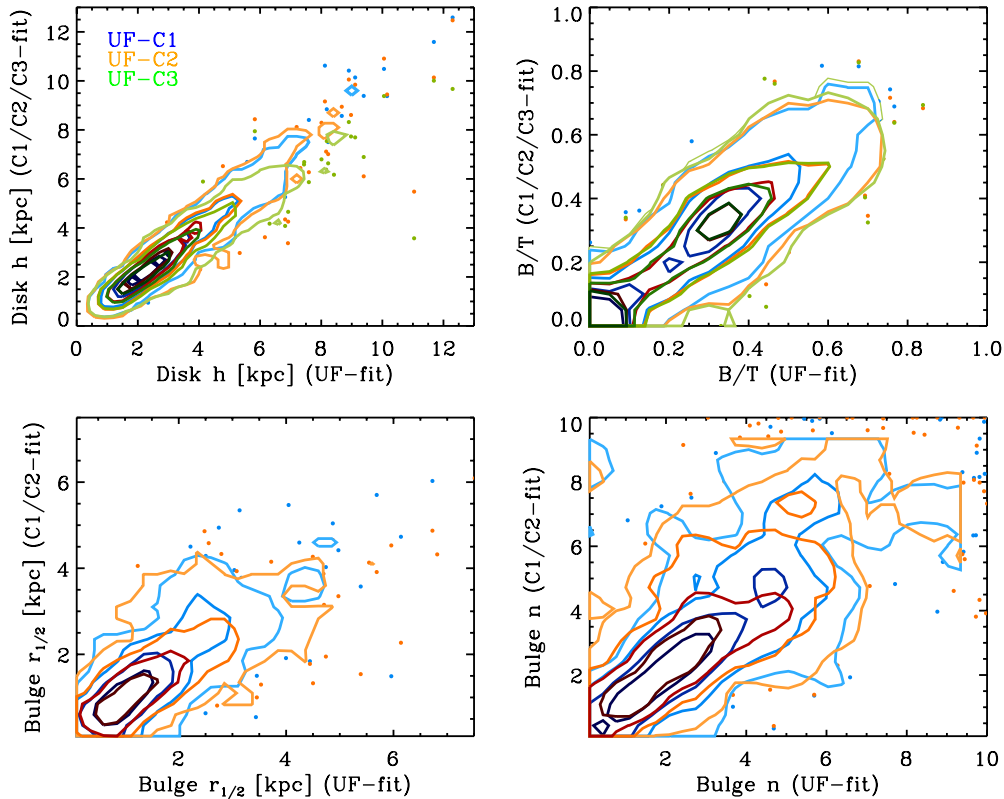
Figure 5. Comparison between the bulge and disk structural parameters obtained with GIM2D in the four different B fits described in Section 4.2. These four B fits vary between being totally unconstrained (UF) and fully tied too the I-band best fit parameters ($C3$). From top to bottom and left to right we show the disk scale-length, bulge-to-total ratio, bulge effective radius, and bulge Sérsic index. The contours identify isodensity regions containing 25%, 50%, 75%, and 95% of the data. The points show the models that are not encompassed by the contours. The three different colors highlight the comparison between the unconstrained B fits (UF) with the B models in which the position angles, ellipticity, and inclination angle are tied to the I band ($C1$, blue contours), with those in which also the bulge half-light radius and Sérsic index are kept fixed ($C2$, orange contours), and with the models which are fully tied to the I-band structural parameters ($C3$, green contours). The green curves are shown only for disk scale lengths and bulge-to-total ratios, as model $C2$ and $C3$ have the same bulge parameters.

single component fits return robust measurements for ∼95% of S0, bulge-dominated spirals, and intermediate-type disk galaxies in the both the B and I bands (see Appendix B for a detailed summary for the individual morphological classes). Bulge+disk decompositions in both B and I bands are available for ∼80% of these galaxies.

For galaxies with a reliable decompositions in both bands, Figure 6 presents the parameters obtained in the two pass-bands. Partly by construction, the scatter around the identity line for the bulge-to-total ratio is less than 0.1 in the vast majority of the cases, as shown on the top left panel of the figure. Given that our morphological classification is based on the I-band bulge-to-total ratios, this means that our classification would not change substantially if we had used the B-band measurements instead. The disk sizes obtained in the two filters agree well with each other, although disks are more extended in the B band than in the I band, as also discussed above. As anticipated, the bulge radii and indices have instead a broader scatter. Note that despite the scatter, in the vast majority of cases the Sérsic indices for the bulge are consistent with either a "concentrated" or a "diffuse" central bulge component in both filters; truly discrepant results are obtained in a small number of cases (∼5%).

Finally, in Appendix B we show the comparison of our bulge+disk GIM2D fits with similar fits obtained with the package GALFIT (Peng et al. 2002), and also with bulge+disk+bar fits; the latter provide an estimate for the impact of a bar component on the bulge (and disk) parameters for disks which host such a third component.

4.2.1. Comparison between Galaxy Half-light Radii Estimated from Single Sérsic Fits and from Bulge+Disk Fits

As discussed extensively in Section 6.3, the calculation of a galaxy size radius is made difficult by a number of observational biases, which can lead to substantial uncertainties. Here we additionally show how the estimation of the galaxy half-light radius depends on the choice of the specific model to the galaxy light by comparing the global galaxies half-light radii derived from the single Sérsic fits with those obtained from the bulge+disk decomposition. This is shown in Figure 7 for the I band, but similar results are obtained in the B band. It is clearly seen that for about 10% of the galaxies with formally "reliable" bulge+disk decomposition and single component fits, half-light radii from the single Sérsic models are larger by more than a factor 1.5 than the sizes inferred from the bulge+disk decompositions. As illustrated in the inset in Figure 7, the majority of the discrepant galaxies have steep light profiles with Sersic index $n > 2$. We note that for all these galaxies both the single and double component fits were inspected to confirm their formal reliability. Furthermore, the magnitude difference between the model galaxy and the real ZENS image within an aperture equal to 1.5 times the Petrosian radius is <0.3 mag for both the single and double component fits.

For these galaxies we decided to keep both radii estimates in our ZENS catalog (published with Paper I) but, to keep memory of the discrepancy, to add to the formal errors an uncertainty equal to half the difference between the two radii estimates. As an indication that these difference in the measured radii are
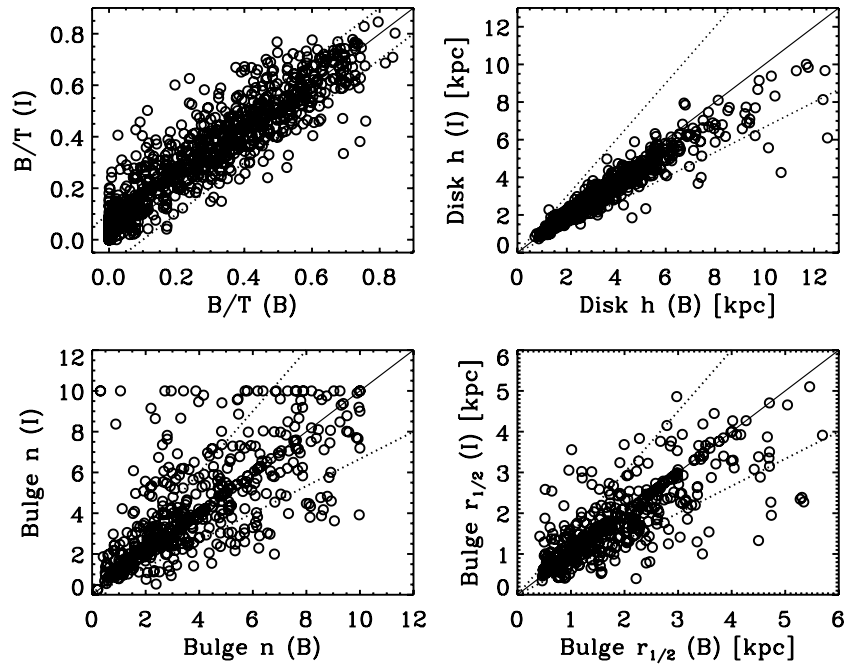
Figure 6. Comparison between the `GIM2D` double-component *I*-band fit parameters and the corresponding parameters in the finally adopted, fiducial *B*-band fits. Specifically, the upper panels show the comparison between the bulge-to-total ratios and disk scale lengths in the two filters. The lower panels show the comparison between the bulge half-light radii and bulge Sérsic indices. In the upper left panel, values are plotted only for galaxies which have detected bulge and disk component in both bands. In the other panels, galaxies are further constrained to have $B/T > 0.1$ when considering bulge parameters. The dashed lines in the upper left panel indicate a positive and negative variation of 0.1 in the bulge-to-total ratio with respect to the identity line; in the other three panels, they indicate a relative change of a factor of 1.5.

not peculiar to the ZENS sample or to the `GIM2D` software, we remark that other recent publications have found evidence of an overestimation of the half-light radius when a single Sérsic fit is performed on a galaxies that have intrinsically a bulge and a disk component for simulations reproducing SDSS noise properties and also using different fitting algorithms (Meert et al. 2012; Mosleh et al. 2013).

5. QUANTIFICATION OF GALAXY STRUCTURE. III. NON-PARAMETRIC ANALYSIS

We further used the *Zurich Estimator of Structural Types Plus* (ZEST+), an upgrade of the ZEST approach published in Scarlata et al. (2007), to derive non-parametric measurements of structure for the ZENS galaxies. Such estimates add further information on the structural properties of the galaxies, are useful in cases where no parametric fit could be performed, and enable comparisons with other published samples.

ZEST+ is a `C+`-based code for the study of galaxy structure and it is designed for automated morphological classification of galaxies through either a principal component analysis or a support vector machines technique. It also features several improvements relative to the ZEST algorithm and implementation of Scarlata et al. (2007; see for example Cameron et al. 2010 for a first application to the COSMOS field; Scoville et al. 2007). The classification scheme uses both user supplied parameters and/or a set of non-parametric morphological coefficients computed by ZEST+ itself. For the ZENS galaxies we employed ZEST+ only to derive the structural coefficients rather than using the morphological classification option since, given the limited size of our sample, we were able to perform visual and quantitative checks on the reliability of the classification for each galaxy individually, which we mainly based on the available bulge-to-disk ratios (see Section 7).
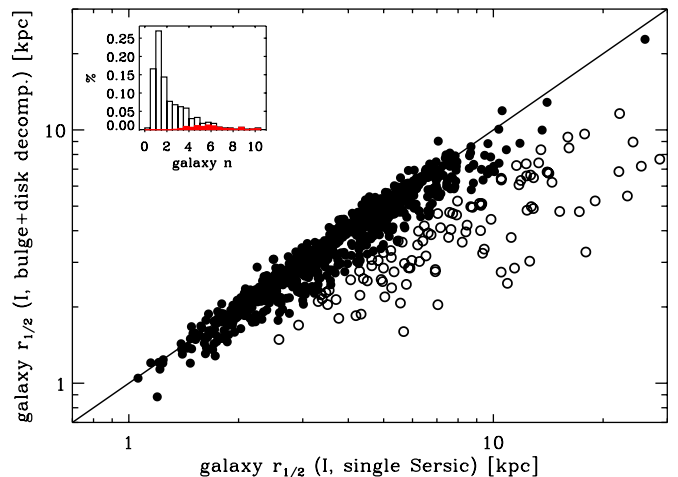

Figure 7. Comparison between *I*-band galaxy half-light radii obtained from single Sérsic fits and bulge+disk decompositions. The empty circles highlight those galaxies for which the two size estimates differ by more than a factor 1.5. The distribution of galaxy Sérsic indices for such discrepant cases are shown in grey (red in the online version) in the inset on the top left corner of the plot, in comparison with the indices for the rest of the sample, shown in black.

(A color version of this figure is available in the online journal.)

The measurements provided by ZEST+ are galaxy concentration (C), asymmetry (A), Gini and M_{20} coefficients, and smoothness (S). These parameters are widely used in the literature to study galaxy structure and morphology (e.g., Conselice 2003; Lotz et al. 2004; Scarlata et al. 2007; Zamojski et al. 2007). For sake of brevity, in the following we will refer to the C, A, Gini, M_{20}, and S set of measurements as to the "*CASGM*" parameters.

The concentration $C = 5 \log(r_{80}/r_{20})$ was defined as the ratio of elliptical radii containing 80% and 20% of the total flux of

the galaxy, which is provided as input by the user. For ZENS, the SEXTRACTOR Kron flux (FLUX_AUTO) was employed.

The asymmetry index A gives information on the degree of rotational symmetry of the galaxy light. This is parameterized through the difference between the original galaxy image and a $180°$-rotated version of it. To account for the effect of background noise, ZEST+ uses the procedure introduced by Zamojski et al. (2007), which involves the calculation of the asymmetry for both the original image $A_0 = (1/2)((\sum_{i,j} |I(i,j) - I_{180}(i,j)|)/\sum_{i,j} |I(i,j)|)$ and for a smoothed version of it, $A_{0,S} = (1/2)((\sum_{i,j} |I^S(i,j) - I^S_{180}(i,j)|)/\sum_{i,j} |I^S(i,j)|)$, where I is the intensity of the image on the pixel (i,j) and I_{180} the intensity of the rotated image. The final asymmetry value is given by $A = A_0 - ((A_0 - A_{0,S})/(1 - 1/\sqrt{5}))$, where the last term corresponds to the background correction factor.

The Gini coefficient G introduced by Abraham et al. (2003) contains information on how uniformly the light is distributed within the galaxy: if the flux is equally distributed among all pixels, then G is equal to zero, whereas if all the light is concentrated in just one pixel, the coefficient G is equal to unity. We defined it as in Lotz et al. (2004): $G = (1/\bar{I}n(n-1)) \sum_i^n (2i - n - 1)\bar{I}_i$, where $\bar{I}$ is the mean of the flux of the galaxy pixels, sorted in increasing order.

The parameter M_{20} is the normalized second-order moment of the brightest 20% of the galaxy pixels. It describes the spatial distribution of bright substructures within the galaxy, such as spiral arms, bars or bright nuclei. The computation of M_{20} involves the following steps: (1) galaxy pixels are ordered by flux, (2) for the 20% brightest pixels, the sum of moments $\Psi = \sum_i^{n_{20}} I_i[(x_i - x_c)^2 + (y_i - y_c)^2]$ with respect to the light-center in the Petrosian ellipse x_c, y_c is computed, and (3) the latter is normalized by the total sum of moments to give $M_{20} = \log_{10}(\Psi/M_{tot})$, with $M_{tot} = \sum_i^{n_{tot}} M_i$.

Finally, the smoothness S is a measure of the degree of clumpiness of the galaxy light distribution, and is thus useful to trace patches in the light profile such as star-forming regions. To calculate S, a smoothed version of the original image, obtained by convolving it with a Gaussian filter of FWHM equal to 0.25 times the Petrosian radius R_p, was subtracted from the image itself. Clumpy regions were then identified from the residual image as those pixels for which the intensity I_{res} is k times higher than the background standard deviation in the residual image σ_{bkg}. We used a default threshold factor of $k = 2.5$. The pixels so identified were then used to calculate $S = (\sum_{i,j} I_{res}(i,j)/\sum_{i,j} |I(i,j)|)_{I_{res}(i,j) > 2.5\sigma_{bkg}}$. A region of radius $0.25 * R_p$ from the center was masked out during the calculation to avoid including the highly concentrated centers of the galaxies which will boost the final value of the smoothness. The Gini, M20, A and S indices were all calculated within one Petrosian ellipse.

Along with the structural indices, ZEST+ also gives an estimate for the "elliptical aperture" galaxy half-light radius, based on the user-provided total flux. These are the measurements we refer to when discussing ZEST+ half-light radii for our ZENS galaxy sample.

6. CORRECTIONS FOR SYSTEMATIC BIASES IN THE STRUCTURAL PARAMETERS

The careful inspection and filtering of the measurements thus far presented, although necessary, does not provide a quantification of systematic errors in the derived structural parameters.

In ZENS, and more generally in ground-based imaging galaxy surveys, the major contributors to such errors can be identified in the noise of the night sky, and in the PSF width. In ZENS, the median I-band PSF FWHM is $1''$, which is about 30% of the median half-light radius of the galaxy sample. Both analytical surface brightness fits and non parametric algorithms are affected by these observational limitation and none is completely free from pitfalls: the ZEST+ measurements are not PSF-deconvolved and, to obtain a consistent measure of structure on the different ZENS fields, an homogenization to a common resolution of the *CASGM* parameters is necessary. In contrast, GIM2D uses the provided PSF to derive, in principle, seeing-corrected quantities, and indeed biases related to PSF-blurring are less severe in GIM2D-based measurements; however, systematic uncertainties remain, especially in low surface brightness regimes, where both aperture photometry and two-dimensional fits are well known to underestimate galaxy sizes and fluxes (e.g., Bernstein et al. 2002a, 2002b; Benítez et al. 2004; Häussler et al. 2007; Cameron & Driver 2007).

We asses here the impact of these effects specifically for our ZENS measurements through tests on artificial galaxy images. In particular, we derive recipes to correct the observed galaxy structural parameters (e.g., sizes, concentrations, ellipticities, etc.) for biases in the observations. In areas of parameter space where we cannot recover the true values of the given parameters, we provide an estimate for the systematic uncertainty that affects the measurements.

We perform this analysis on the I-band, which provides a view of the intrinsic galaxy structure less affected by dust or young stars thus is used as our fiducial band to classify galaxies structurally and morphologically. The corrections in the B-band are then derived from those obtained for the I measurements, suitably rescaled to the B-band luminosity and PSF.

6.1. Methodology

The derivation of the corrections is done by applying the entire process of object extraction, followed by parametric and non-parametric photometric/structural measurements with SEXTRACTOR/ZEST+ and GIM2D, in exactly the same way as on the real data, to a set of artificial galaxy images for which the intrinsic structural/photometric properties are know precisely by construction. The difference between the model input and output parameters provides an estimate of the uncertainties in the measurements.

A self-consistent study of the errors in the quantification of the galaxy structural properties must be a function of five parameters: the galaxy luminosity (magnitude, *mag*), the galaxy size (half-light radius $r_{1/2}$), the inclination (ellipticity ϵ), the steepness of the light profile (Sérsic index n or concentration C) and the PSF under which the galaxy was observed. The effects of each of such parameters on the quantification of structure, including galaxy sizes, are tightly interconnected and hence need to be considered simultaneously. It is immediately clear that, as an example, the impact of the PSF is stronger—with all other parameters fixed—for highly concentrated galaxies than for those with shallow light profiles, and for galaxies with sizes comparable to the seeing than for more extended ones.

We thus adopt a sampling approach in which we construct many thousand artificial galaxy models to fully explore the observed parameter space of galaxies in the ZENS data set, and such to have, for each combination of the five parameters $mag - r_{1/2} - \epsilon - n(\text{or } C) - PSF$, a sufficient number of models on which to test the measurements. This approach is also used

in Carollo et al. (2013a) on a higher-redshift sample of galaxies extracted from the COSMOS survey.

Two cautionary remarks need to be made: first, our artificial galaxies are generated to populate *uniformly* a broad grid in the five-dimensional $mag - r_{1/2} - \epsilon - n(\text{or } C) - PSF$ space. Real galaxies are not uniformly distributed in this parameter space and this is not taken into account in our corrections. Second, we deliberately ignore dust or stellar population segregation effects, as our models are created smooth and neglect dust attenuation. In the following we will test the robustness of our corrections toward the specific design of the simulations.

6.2. Generation of the Artificial Galaxy Images

To derive our correction functions for the structural parameters of ZENS galaxies we created both Sérsic models and bulge+disk artificial galaxies on which we tested the corresponding GIM2D fits. In both cases, models were constructed on a grid of points in the ellipticity, magnitude, size, and Sérsic index (or B/T ratio) parameter space. Specifically, in the single component case, galaxies were simulated around the following regions: $r_{1/2} = [0.4, 0.7, 0.9, 1.3, 1.5, 2, 3, 8, 20]$ kpc, $I_{AB} = [13, 14, 15, 16, 17, 18, 19, 20]$, $\epsilon = [0.1, 0.3, 0.6, 0.9]$, and $n = [0.5, 1, 1.5, 2.5, 3.5, 4.5, 7.5]$. For each grid node 30 models were generated randomly to have: radii and Sérsic indices within $\pm 30\%$ of the nominal radius and index n at the grid point, magnitude within ± 0.25 mag and a difference in ellipticity equal to ± 0.05. This makes a total of $\sim 60{,}000$ single-component model galaxies.

For the double component model galaxies, which span a wider range of combination of bulge and disk parameters and are also computationally more expensive, we used a coarser sampling of the parameter space, creating models in the following way: given a value of the magnitude for the *entire* galaxy randomly generated around the points $I_{AB} = [13.7, 15.4, 16.8, 18.2, 19.6]$ and a disk scale length h similarly chosen within $\pm 30\%$ from the positions $[0.5, 1, 1.5, 3, 6, 15]$ kpc, artificial galaxies were constructed in three bins of bulge-to-total ratios centered at values of $B/T = 0.15, 0.4, 0.65$ and of width $\Delta(B/T) = 0.15$, hence allowing a maximum $B/T = 0.8$. The bulge half-light radius was selected on the same grid used for the disk scale length, but imposing that $R_e < 1.678 \times h$. The bulge Sérsic index was allowed to have values $n = 0.5, 1, 2.5, 4, 8$ with a scatter of $\pm 30\%$ and three bins of disk ellipticity (i.e., galaxy inclination) $\epsilon_{disk} = 0.1, 0.4, 0.7 \pm 0.1$ were employed. We furthermore assumed that bulges cannot be very elongated and hence explored only two values of the ellipticity for the bulge component, namely $\epsilon = 0.1$ and $\epsilon = 0.6$, so to bracket any other value in between.

All model galaxies described above were then convolved with three PSF sizes for a total of 180,000 single component models and $\sim 90{,}000$ double-component models. The three PSF sizes were taken to reproduce the best, medium, and worst ZENS seeing in the I band (respectively $0\farcs7$, $1''$, and $1\farcs5$). The PSF-convolved models were inserted with Poisson sampling into sky-subtracted empty regions extracted from the real ZENS fields. To mimic noise in the reconstruction of the PSF in the real data, when performing the GIM2D fits on the simulated galaxies we provided as input to the code a rotated version of the PSF originally used to convolve the artificial image.

For brevity, we focus in the following on the results obtained for the simulations convolved with the median ZENS PSF, which are hence representative of the bulk of the ZENS observations. In Appendix C, a full account of the results derived with the

best and worst PSF can be found (see Figures 29–32), showing correction matrices that are consistent with those presented here. Note that the corrections to each ZENS galaxy were obtained through linear interpolation, at the PSF size value relevant for any given galaxy, of the correction matrices describing PSF sizes that bracketed the PSF in question.

6.3. Implementing the Derived Corrections to Galaxy Sizes and Magnitudes

We start the description of the resulting correction functions by focusing on those parameters that our approach can self-consistently correct without recurring to additional information, namely galaxy sizes and magnitudes. We show in Section 6.4 how for other structural properties, such as the concentration coefficient, the recovery of the "true" values is instead less straightforward, and depends on the intrinsic distribution of parameters in the simulated sample (and requires therefore a different approach).

Our fiducial measurements of galaxy sizes in ZENS are those that we derive from the GIM2D analytic fits, which are less prone to systematic biases then those inferred with ZEST+, as we show below. It is nonetheless worthy to discuss here also the results for the ZEST+ measurements, given that these measurements are used for the few ZENS galaxies for which no reliable GIM2D fit could be achieved.

After the extraction/fitting process on the artificial galaxies was completed, we produced "calibration maps" for sizes and magnitudes as shown in Figures 8 and 9 (see also Carollo et al. 2013b for further details on this calibration approach). The arrows in the maps show, at any point of the *observed* $r_{1/2} - mag - \epsilon - n(\text{or } C)$ plane, the direction and strength of the correction which is needed to recover the "intrinsic" galaxy size and magnitudes from the observed values; these correction arrows are obtained by taking the median difference between the model nominal input parameters and the parameters measured with ZEST+/GIM2D of all artificial galaxies in the given point in the grid. The correction matrices are binned in three separate panels of concentration/Sérsic index and three separate panels of ellipticity. The colors of the arrows gives the amount of scatter shown by the individual models around the median correction: in green are grid points where all corrections are coherent in strength, in red are shown those which have a high scatter and hence our correction is representative on average but not for the single models. We use these maps to derive corrections for observed magnitude and sizes in the real ZENS galaxy sample. The choice of a discretized but dense grid allows us to pinpoint the correction/uncertainty maps at well localized positions on the considered planes. As indicated above, the corrections for any given real ZENS galaxy are obtained by interpolation at the position of the ZENS galaxy in the *observed* $\epsilon - mag - r_{1/2} - n(C) - PSF$ space.

To discuss Figures 8 and 9 it is useful to identify three regions in the $mag - r_{1/2}$ plane: (1) the region populated by models that are close to the surface brightness limit of the ZENS study (indicated with the dashed black lines in the plot), (2) the region of well-resolved high signal-to-noise ratio measurements, and (3) the region close or below the size of the PSF (highlighted with a gray horizontal line).

Above the detection and resolution limit and at low ($C < 2.5$, $n < 1.5$) to intermediate ($C \simeq 3$, $n \simeq 2.5$) concentrations, both GIM2D and ZEST+ perform fairly well and only small corrections are needed for both $r_{1/2}$ and magnitude.
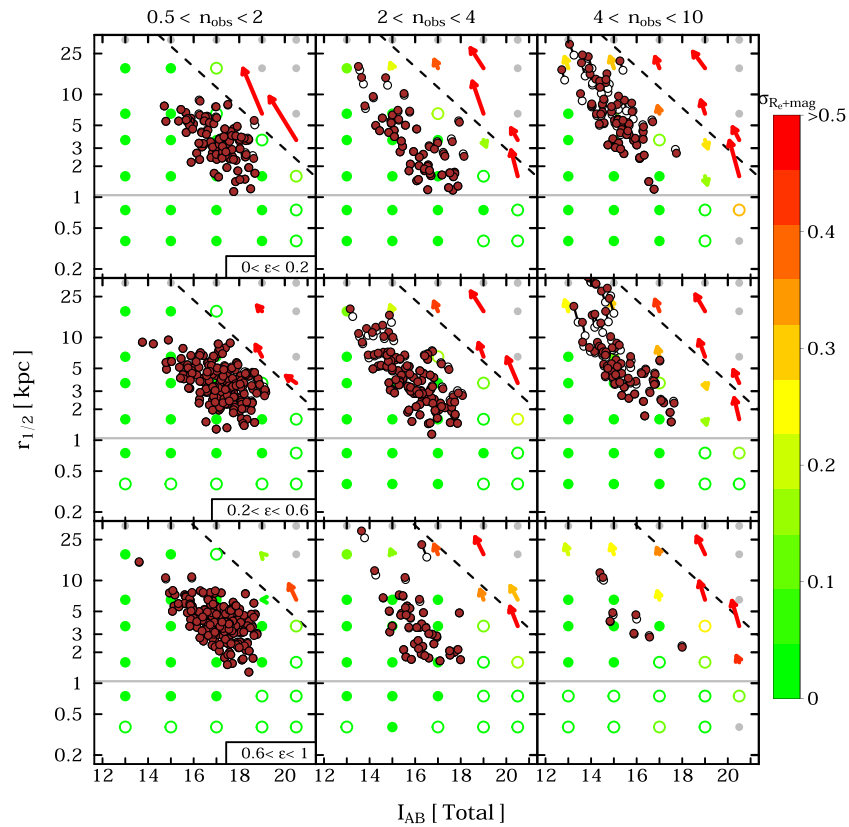
Figure 8. Size–magnitude plane with arrows illustrating the strength of the correction vector that must be applied at each grid point to recover intrinsic total magnitudes and sizes from the observed magnitude and sizes (as measured by GIM2D in the ZENS I-band imaging). The corrections are based on single Sérsic fits to single Sérsic galaxy models; they are shown binned in three different panels of observed Sérsic index (from left to right) and three panels of observed galaxy ellipticity (from top to bottom). Arrows represent the direction and strength of the corrections at each grid point; they are obtained as the median difference in magnitude (Δm) and radius ($\Delta r_{1/2}$) between the input models and the measured parameters at the given grid point. Colored circles show positions in the plotted parameter space in which no corrections to magnitudes and sizes are required; these are defined as grid points in which 80% of the models have a correction in radius and magnitude which are, respectively, <20% and <0.3 mag. The colors of the arrows and circles indicate the amount of scatter in the individual contributing models relative to the shown median correction. The scatter increases from green to red and is defined as the quadratic sum of the median absolute deviations of $\Delta R_i/R_i$ and $\Delta F_i/F_i$, with ΔR_i and ΔF_i the size and flux differences between each individual model at the corresponding median value. The precise values of the scatter around the medians at any color is given in the color chart on the right-hand side of the figure. Empty colored circles represent regions in the $mag - r_{1/2}$ plane where the recovery of the models' ellipticity and Sérsic index is subject to large uncertainties; precisely, empty colored circles show those grid points in which at least 25% of the models have a difference between input and output ϵ or n which is larger than 0.08 and 15%, respectively. The gray horizontal line marks the value of the typical PSF FWHM for the ZENS observations; the dashed black line highlights the surface brightness limit of our images. Gray dots highlight regions of incompleteness in the observed space, i.e., which are populated by less than 10 model galaxies. Corrected radii and magnitudes for the real ZENS galaxies that were observed with a seeing ~1″ are plotted as small brown circles; for galaxies with magnitude-radii measurements falling on grid points with a correction arrow, we show as empty circles their pre-correction, raw measurements; corrections up to ~40% had to be applied, in particular to galaxies with steep light profiles.

(A color version of this figure is available in the online journal.)

Not surprisingly, below the sky noise surface brightness, basically no galaxy can be recovered by both ZEST+ and GIM2D, as models are a priori not detected during the SEXTRACTOR source extraction (necessary to define the total galaxy flux and the initial guess for the size needed as input by ZEST+ and GIM2D). For galaxies with low concentration/Sérsic index, the detection rate falls rapidly to zero when the surface brightness limit is reached (no model with $I_{AB} \sim 19$ and $r_{1/2} \sim 10$ kpc is recovered). Conversely, the centrally peaked light distribution in galaxies with higher concentration pushes the detection limit to slightly fainter surface brightnesses. Close to the surface brightness limit, magnitude and sizes are severely underestimated for both GIM2D and ZEST+ fits: sizes are typically smaller by more than a factor of two (three) and magnitudes are dimmer by half (one) magnitude for GIM2D (ZEST+) measurements.

At $C > 3$, the ZEST+ "aperture" measurements suffer from a strong underestimation of sizes and magnitudes at any signal-to-noise. This is a consequence of the well known tendency to miss a substantial fraction of the flux from the faint wings

in steep light profiles when performing aperture photometry measurements. Integration to total light mitigates this effect in the GIM2D models, which nonetheless results in sizes which are about 30% smaller than the intrinsic ones for extended galaxies with steep light profiles ($r_{1/2} \gtrsim 10$ kpc).

When moving close to the resolution limit of the survey, we notice further differences between the performance of ZEST+ and GIM2D. Thanks to the PSF deconvolution, the analytical fits are able to reliable recover the sizes also for models with sizes below the PSF FWHM. Systematic effects become visible only at the worst observing condition (see Figure 30 in Appendix C). ZEST+ suffers from much stronger biases in this regime, causing an artificial increase of the size of models with $r_{1/2} < PSF$ for any value of the seeing. We note however that our approach, being based on idealized, regular galaxy light distributions produced with GIM2D, may return in general an optimistically good performance of GIM2D than when recovering the parameters for real galaxies with irregular, clumpy light distributions. Our corrections are thus to be considered as the
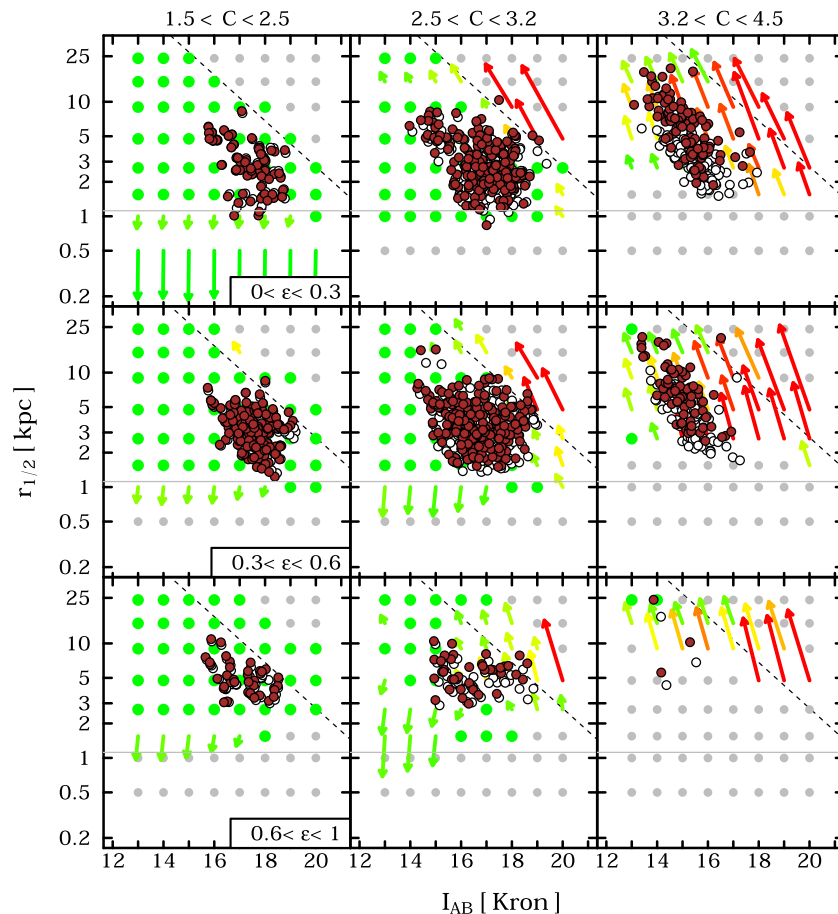
Figure 9. Same as Figure 8 but for measurements obtained with ZEST+. In this case, models and observed galaxies are binned in three panels according to the measured concentration index C. Colors and symbols are as in Figure 8. Note that the corrections are, as expected, more substantial than those shown in Figure 8 for the GIM2D-based measurements.

(A color version of this figure is available in the online journal.)

"minimal" correction functions that must be applied to the data to put the structural measurements on a comparable grid.

6.4. The Impact of the PSF on Concentration and Ellipticity Measurements

Another clear effect observed for the ZEST+-based parameters is a lack of recovered parameters in the galaxy half-light radius $r_{1/2}$ versus magnitude plane at high concentrations and small radii (see right most panels of Figure 9); this becomes increasingly more severe at higher ellipticities and larger PSF FWHM (see also Figures 31 and 32). A similar trend is observed for the GIM2D fits in the worst seeing conditions and at small radii (Figure 30). Note that, consistently, the distribution of the real ZENS galaxy measurements based on ZEST+ in Figure 9 presents the same bias.

The origin of such effect is investigated in Figure 10, which illustrates where the artificial galaxies, created in a given region of the parameter space, are placed in the *observed* space. In this map, the arrows indicate the direction in which models generated with a certain ϵ and C are displaced relative to their intrinsic concentration and ellipticity: an upward-pointing arrow indicates that models are observed on average as less elongated, and a left-pointing arrow indicated that they are observed at lower concentrations. Intrinsic concentrations are calculated analytically from the original models Sérsic indices and refer to the ratio of the radii containing 80% and 20% of the *Petrosian*

flux (see, e.g., Graham et al. 2005). In the same figure, red-to-yellow squares indicate points in the grid in which at least 50% (up to 100% for full red squares) of the artificial galaxies that are *observed* at that location originate from a different intrinsic concentration or ellipticity grid point. Green points in the figure indicate grid nodes that are not affected by either scattering of galaxies into the grid point from different intrinsic concentration/ellipticity panels or by scattering of galaxies out of the grid point into a different panel of observed ellipticity and/or concentration.

It is clearly seen in Figure 10 that model galaxies which were originally generated at high concentrations and ellipticities have a high probability to be scattered into lower ϵ and C bins by the aperture-based ZEST measurements; this bias is exacerbated at sizes $\lesssim 2$–3 kpc. This is caused by the effect of the PSF convolution which artificially lowers a galaxy concentration and circularizes their axis ratio. Consequently, this ZEST+ region of the $mag - r_{1/2}$ plane out to ~ 2 PSF radii is highly degenerate, being populated by both galaxies which have intrinsic parameters in that location of parameter space, and by galaxies which are scattered into it from higher ellipticity and/or concentration regions. Given this degeneracy, it is important to verify to which extent the corrections for radii and magnitude that we discussed above depends on the precise way in which the simulation grid is populated. If model galaxies that are "scattered in" and those which have intrinsic parameters in that location of parameter space required different
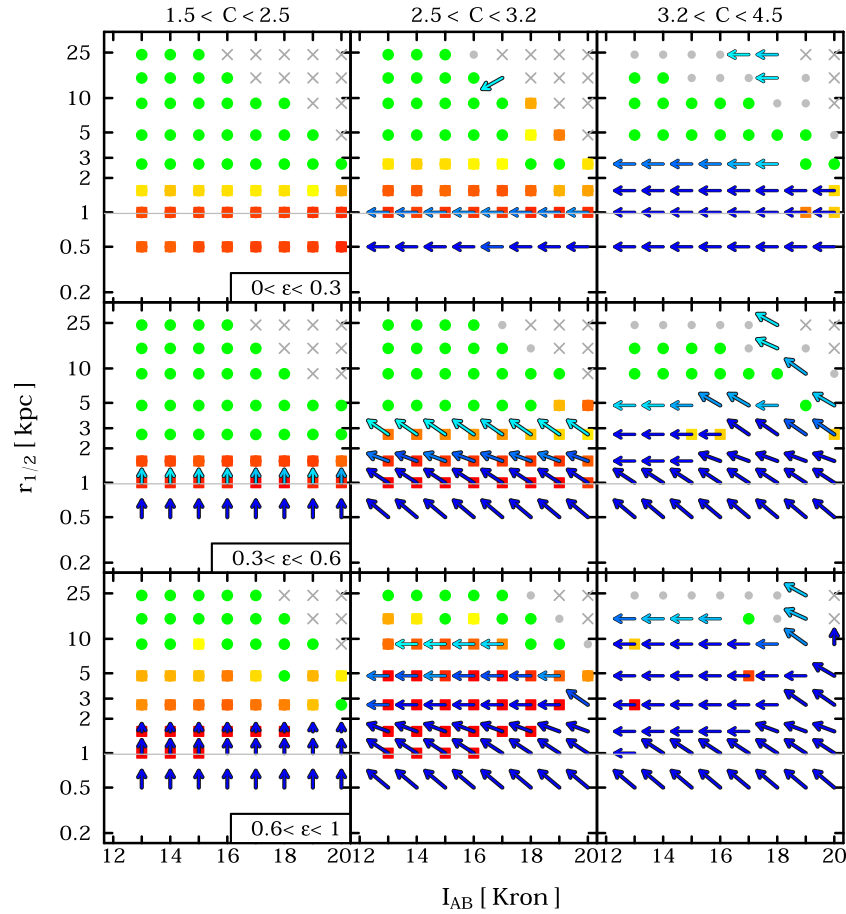
Figure 10. Size vs. *I*-band magnitude plane on which we show the effect of measurement biases on the recovery of galaxy concentration and ellipticity calculated with ZEST+. Colored arrows and squares indicate, respectively, the scattering of model galaxies out of their intrinsic C and ϵ panels, and into a different panel of measured C and ϵ: e.g., an upward-pointing arrow indicates that model galaxies with intrinsic parameters in that grid point are observed in a higher b/a ratio panel, while a left-pointing arrow indicates that the model galaxies are observed in a panel of lower concentration. An arrow is drawn on a grid point if at least 50% of the models that are generated at that given $r_{1/2} - mag - \epsilon - C$ point are scattered out of it into a different concentration or ellipticity panel. To draw the horizontal (vertical) component of the arrow, we further require that at least 25% of the scattered models change, when observed, panel of concentration (ellipticity). Blue colors become darker with increasingly larger fractions of objects scattered out of a given panel. The length of the arrows is arbitrary, set for plotting purposes, and has no specific meaning. With yellow squares we show the points of the $r_{1/2} - mag$ grid in which at least 50% of the *observed* model galaxies were generated in a different panel of intrinsic concentration or ellipticity (up to 100%, shown with full red squares). Green points indicate grid nodes in the observed C or ϵ parameter space which do not suffer from strong scattering of intrinsic model galaxies either into it or out of it. Gray crosses and dots respectively highlight the grid points which are below the surface brightness limit of the ZENS study, and in which galaxy models with intrinsic C and ϵ in those grid points are recovered by ZEST+ at a different radius and/or magnitude, but within the same concentration/ellipticity panel (i.e., at a different grid point within the same panel).

(A color version of this figure is available in the online journal.)

corrections, then a precise modeling of the relative fractions of such galaxies in the given grid point would be needed. To test this, we created magnitude and sizes correction maps using either only artificial galaxies that were scattered into the given $\epsilon - C$ bin or only galaxies born in situ. We show the outcome of such an experiment for the median PSF in Figure 33 in Appendix C. Both realizations resulted in very similar corrections for size and magnitudes, indicating that these are robust independent of the intrinsic concentration/ellipticity of the galaxies.

On the other hand, models which are scattered into lower C or ϵ bins require by definition stronger corrections in ϵ and C themselves than those which were generated within the bin. Although for ellipticity it is reasonable to assume that also real (disk) galaxies would have an uniform distribution, and we hence can consider our corrections to be representative, the correction for concentration depends on the relative fraction of truly low concentration galaxies with respect to galaxies with a high intrinsic concentration. Given that we have a no priori

knowledge of the true distribution of concentrations for the real galaxies, and to avoid introducing biases associated to the choice of the simulation grid, we choose to follow a different method to correct the non-parametric structural estimators, which uses the available information on the Sérsic index. For data sets that do not have an as comprehensive set of measurements as ZENS, this approach could not be applied and a statistical modeling of the underlying distribution of galaxies will be needed. These results should be taken as a cautionary note in using solely the concentration index as a morphological discriminant for galaxy types, especially if galaxies are close to the resolution limit of the given survey and if no correction to this parameter is attempted.

Conversely to the ZEST+ measurements, an equivalent map as in Figure 10 but for Sérsic indices and ellipticities measured by GIM2D (not shown) demonstrates instead only a marginal contamination/scattering of galaxy models across the broad ellipticity and n bins, thanks to the PSF-deconvolution performed by the GIM2D fitting algorithm. For this reason, we apply to

the ellipticities and Sérsic indices the corrections obtained by interpolating between the relevant grid points of the previously discussed vector maps, which we regard as statistically representative of the average correction. We stress however that systematic effects are observed for model galaxies convolved with the worst PSF of ZENS: in this case, models with high Sérsic indices and sizes smaller than ∼1–1.5× the PSF size are scattered to lower n. Interestingly, GIM2D tends to overestimate the ellipticity of such galaxies as opposed to what is observed for the measurements performed with ZEST+. Furthermore, although under typical observing conditions the errors on ellipticity and Sérsic index measured with GIM2D are small enough to keep model galaxies within the same bin in these parameters, moving closer to the resolution or detection limit of the ZENS WFI images increases the randomicity in the measurements; inferred ellipticities and Sérsic indices have a typical scatter of ∼0.1 and 20%–30%, respectively. We highlight these problematic regions with empty symbols in Figure 8. We finally note that a PSF correction is often included—typically as a convolution-kernel in surface brightness fitting algorithms—in structural studies based on other ground-based datasets, including the SDSS (whose typical PSF width is similar to the worst ZENS PSF; see, e.g., Blanton et al. 2003; Lackner & Gunn 2012). As we show above, it is possible however that further residual (size-, magnitude-, ellipticity-, and concentration-dependent) corrections to the structural parameters may be needed, depending on the specific PSF, signal-to-noise, and redshift of the studied samples.

6.5. Corrections of Non-parametric Structural Indices

To overcome potential biases associated with calculating a correction for the *CASGM* parameters which may depend on the distribution of intrinsic structural properties, we use the Sérsic indices of the galaxies from the GIM2D fits as a prior. Sérsic indices are robustly determined in the vast majority of the models and are less prone to systematic biases, as discussed in the previous section.

The corrections for concentration, Gini and M_{20} indices are thus derived by splitting the artificial and real galaxies in similar bins of magnitude, radius, ellipticity, and PSF as those employed for the size corrections (see Figure 9). In this case, however, we characterize the galaxy structure according to the observed Sérsic index rather than observed concentration, dividing the samples in three broad bins of $0.2 < n_{obs} < 1.5$, $1.5 < n_{obs} < 3.5$, and $3.5 < n_{obs} < 10$, respectively.

Following the same approach as for sizes and magnitudes, the corrections for non-parametric structural estimators are then defined as the median difference between the models' intrinsic indices and those calculated with ZEST+ at the given position in the observed $mag - r_{1/2} - \epsilon - n - PSF$ parameter space. The intrinsic concentration is computed analytically from the input Sérsic index, as specified above, while for the Gini and M_{20} indices we use the measurements performed on "pure" models that are neither PSF-convolved nor degraded with the ZENS typical noise. Given that our analysis is based on intrinsically smooth and axisymmetric models, we do not attempt to correct the asymmetry and smoothness index. These quantities will nonetheless be affected (the smoothness possibly by the largest amount), and this caveat should hence be kept in mind. For the few ZENS galaxies for which no GIM2D fit is available, we applied an average correction obtained as the median of the correction for the ZENS galaxies having GIM2D fits and similar observed concentrations.

6.6. Robustness of the Bulge-to-disk Decompositions

A similar approach as the one employed for the single Sérsic fits was used to test the reliability of the GIM2D bulge+disk (B+D) decompositions. All the B+D model galaxies were processed in exactly the same way as the real galaxies, i.e., after the decomposition, the output models were filtered to reject the unphysical fits and to identify acceptable B+D decompositions (see Appendix B.2). Consistently with the approach used for the real galaxies, only these were used for deriving the correction functions for the B+D parameters.

The correction maps for the B+D parameters are shown in Figures 11 and 12, for the three PSFs. For bulges, we present the results for all disk inclinations together, as no strong dependence on the model axis ratio was detected.

Both scale lengths and magnitudes of disks are very well recovered by the GIM2D code for most of the cases. Systematic deviations from the input parameters are observed only for very small disks (i.e., $h \sim 0.5 \times$ PSF), especially for the largest PSF size and in the low surface brightness limit where disk scale lengths are underestimated by a factor of about two and the measured magnitudes are systematically fainter than the input ones, as already discussed above. Globally, in only ∼10% of the cases the normalized difference between input and output disk sizes is larger than ∼50%, and predominantly in the low surface brightness regime.

The bulge parameter is instead subject to much larger uncertainties, as illustrated in Figure 12. Although in many regions of the magnitude-size relation there are no systematic corrections and the scatter of measured bulge sizes around the input ones is generally large, typically ∼30%–40% for the measured bulge half-light radii. The strongest differences between input and output model parameters are measured for bulges with high Sérsic indices ($n \gtrsim 4$) in which case a substantial over-estimation of bulge-effective radii is observed. Low Sérsic index bulges (leftmost panels in the figure) suffer from smaller measurement errors. Below the resolution limit and for the worst PSF, sizes are overestimated for bulges with $n < 4$ whereas the effect is less evident for the best or intermediate PSF.

These uncertainties in bulge sizes reflects in (or are possibly generated by) a general difficulty in recovering the correct bulge Sérsic index. As an illustration of this fact, we plot the comparison between input and measured bulge Sérsic indices for the median PSF in the top panel of Figure 13. It can be noticed how the measured Sérsic index, especially below $n \simeq 2$, can deviate substantially from the model intrinsic values. This is particularly severe for bulges with half-light radii that are close to the PSF size: small bulges with low index n can be misclassified as bulges with larger half-light radii and steeper light profiles.

Although the structural properties of the bulges are subject to relatively large uncertainties, the fractional contribution of the bulge to the total light is generally well measured by the GIM2D decompositions, as shown on the middle panel of Figure 13. In the bottom panel we plot, for a given value of the observed bulge-to-total ratio, the fraction of input models that were originated with a B/T that differed less than 0.15 from the measured one, between 0.15 and 0.3 and more than 0.3 (black, gray, and red lines respectively). In ∼80%–85% of the cases the bulge-to-total ratio is recovered within a scatter of 0.15 and really catastrophic failures ($\Delta(B/T) > 0.3$) happen in $\lesssim$10% of the models. It is worth to notice that the fraction of galaxies for which the B/T is robustly recovered is largely independent of the value
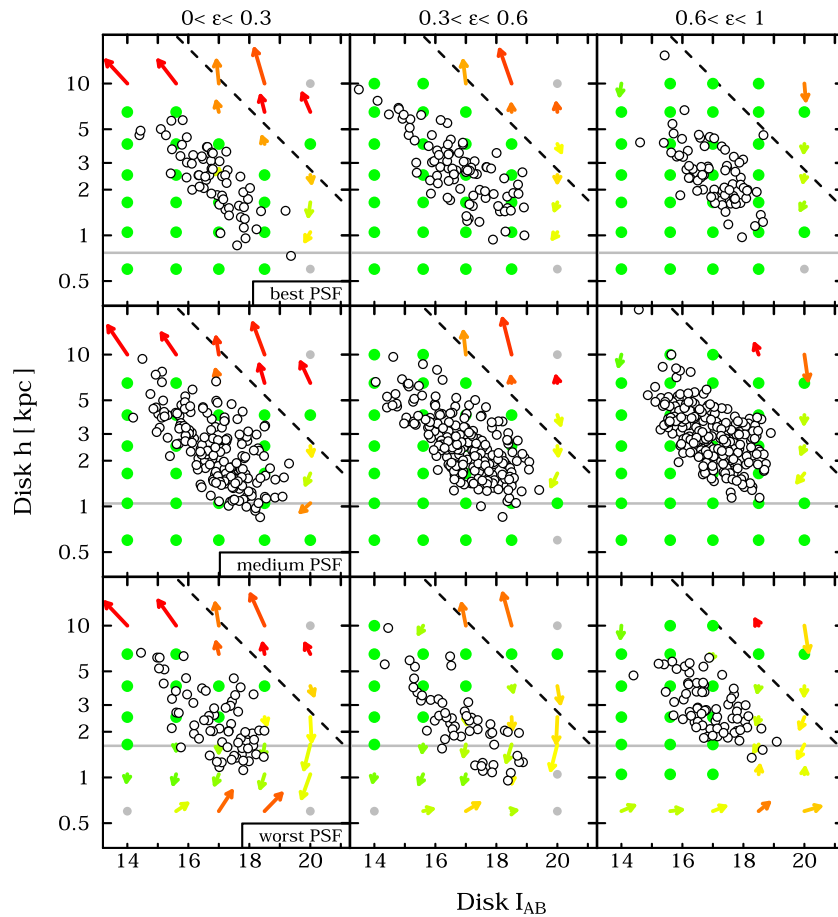
Figure 11. Disk scale length h vs. disk I-band magnitude plane with highlighted the error vectors illustrating the systematic errors on the disk scale length and I magnitude recovered by GIM2D relative to the intrinsic values. These vector maps are the results of our extensive simulations described in Section 6. Only models with measured bulge-to-disk ratio $B/T < 0.80$ are considered in this figure. From top to bottom, the panels refer to the best, median, and worst ZENS PSF. Results are presented from left to right in three bins of disk ellipticity. Colors and symbols are as in Figure 8. Small black empty circles indicate the real measurements for the disk components of ZENS galaxies.

(A color version of this figure is available in the online journal.)

of B/T itself, and the typical scatter around the input bulge-to-total ratio is of order ~0.1. Problematic fits which results in large differences in B/T are again mostly associated with flat ($n < 2$) and small ($r_{1/2} < 1\,\mathrm{kpc} \simeq$ PSF) bulges for which it is difficult to disentangle the disk component from the small, disk-like bulge.

In the light of these results, we decided *not* to apply any corrections to the bulge and disks structural parameters: on the one hand, disk sizes are well recovered by the GIM2D fits so no substantial correction is needed; on the other hand, the large scatter in the recovered bulge half-light radii and Sérsic indices make the derived corrections noisy and dependent on the specific sampling of parameter space with our simulations. For this reason, we prefer to use the direct output from GIM2D for the bulge half-light radii, but with associated a typical uncertainty of 30%, as estimated from our tests.

6.7. Testing the Robustness of the Applied Corrections

We present a number of diagnostic tests that we performed to verify the reliability of the corrections for the structural parameters that are described in Sections 6.3 and 6.5.

As a first sanity check we run our correction scheme, in exactly the same fashion as for the real galaxies, on the measured properties for the models themselves. The outcome of this

exercise is illustrated in the upper panels of Figure 14 for sizes obtained with GIM2D and ZEST+, for models convolved with the median PSF. The intrinsic (input) and corrected radii for the model galaxies agree very well and systematic biases that are present in the uncorrected sizes are largely cured by our correction scheme. Furthermore, the large discrepancies between the ZEST+ and GIM2D raw measurements disappear in the corrected data.

The bottom panels in Figure 14 show the comparisons of ZEST+ and GIM2D half-light radii, ellipticities, and I-band magnitudes before and after the application of our correction schemes for the real ZENS galaxies. The raw sizes derived by ZEST+ are systematically smaller than those obtained by the GIM2D fits by up to a factor of ~2–3 in the worst cases. Our correction scheme nicely brings the two estimates into a very good agreement. As a consequence of the PSF convolution, galaxies are also measured to be rounder in ZEST+ than in GIM2D, especially at low radii, a bias which is largely cured by the implementation of the correction scheme. The latter also mitigates the underestimation of the total fluxes in ZEST+.

The comparison between uncorrected and corrected I-band C, Gini, and M_{20} indices is shown in Figure 15. Specifically, to test whether our corrections deal properly with PSF-induced biases, we compare, for corrected and uncorrected measurements,
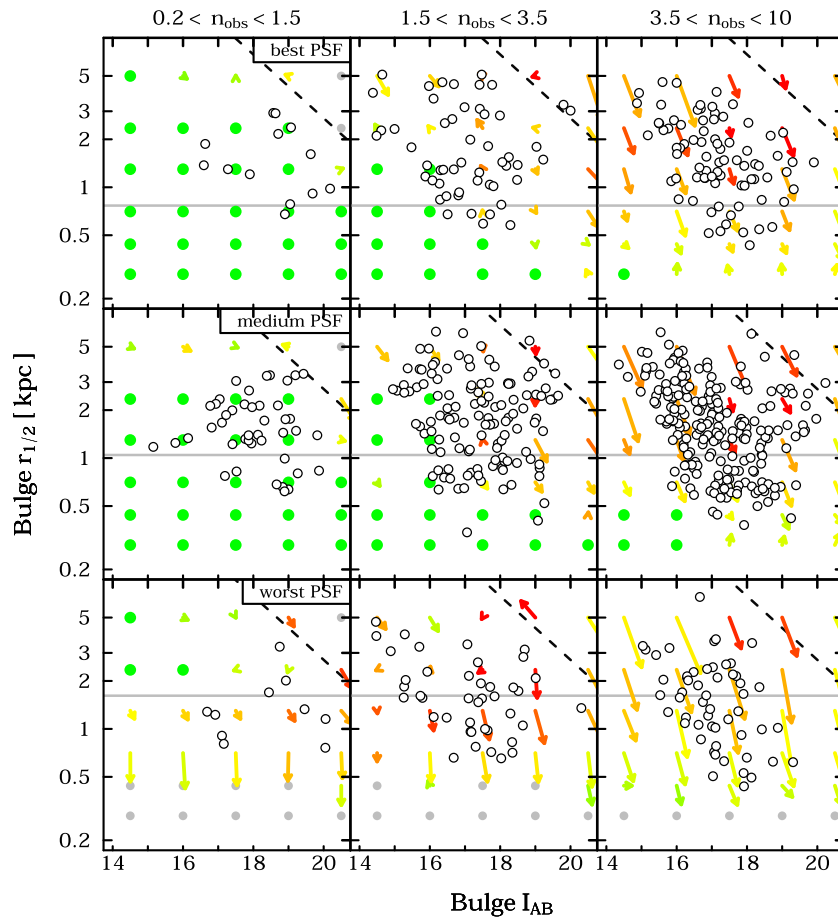
Figure 12. Bulge half-light radius $r_{1/2}$ vs. bulge I-band magnitude plane with highlighted error vectors illustrating the systematic errors on the bulge radii and magnitudes recovered by GIM2D relative to the intrinsic values. Only models with measured bulge-to-disk ratio $0.1 < B/T < 0.80$ are considered in this figure. From top to bottom, the panels refer to the best, median, and worst ZENS PSF. Results are presented from left to right in three bins of Sérsic indices. Colors and symbols are as in Figure 8. Small black empty circles indicate the real measurements for the disk components of ZENS galaxies.

(A color version of this figure is available in the online journal.)

the distributions of these parameters for two bins of PSF size, i.e., PSF FWHM $< 0\rlap{.}''9$ and $> 1\rlap{.}''1$, respectively. The uncorrected indices show different distributions for galaxies observed with small or large PSF's FWHM. The effect is mostly evident for the concentration parameter, for which a two-sided Kolmogorov–Smirnov test rejects the possibility that the low and high FWHM samples are drawn from the same parent distribution at the 99% confidence level. A similar effect is also noticeable for the M_{20} index; the Gini coefficient is instead less sensitive to PSF blurring. All such biases disappear once our corrections are applied, as shown in the lower panels of the same figure. The inspection of the distributions of Figure 15 furthermore shows that the corrections recover the peak of high C values for the early-type galaxies, which would otherwise be absent from the raw measurements. Similarly, the peak at "more negative" values is recovered in the corrected M_{20} distributions.

This is also highlighted in Figure 16, where we show the comparison between corrected and uncorrected non-parametric structural estimators and the corrected Sérsic indices. The upper-left panel shows the comparison for the concentration index: the solid red line marks the expected values of the concentration inside the Petrosian radius for a perfect Sérsic profile of a given index n. It is clear that before correction, the measured concentration flattens rapidly at values ~ 3–3.5 for $n \geqslant 3$, lying far away from the theoretical line. After applying our correction, the measured points match this line well. A similar adjustment is

also observed for the M_{20} index, while, as already mentioned, the Gini coefficient is measured quite robustly and needs virtually no corrections. The upper-right inset shows the dependence on ellipticity of uncorrected concentration and M_{20} parameters for galaxies classified as disks in Section 7; the spurious lack of high concentration galaxies at high elongation is largely ameliorated by our correction scheme.

We stress in concluding that all our corrections are clearly "statistical." For example, individual models can retain an underestimation of the radius of up to a factor 30%, especially models close to the surface brightness limit of the ZENS observations. Nevertheless, in a statistical sense, our correction schemes return well-calibrated measurements that can be robustly compared with each other.

6.8. A Comparison with Previous Work

In Figure 17 we show a comparison between the mass-size relation obtained for the ZENS galaxies, both before and after applying the corrections outlined in Section 6.3, and the relation derived by Shen et al. (2003) in SDSS. Shen's sizes are from the Sérsic fits of Blanton et al. (2003) and are thus similar to the sizes of the VAGC catalog (see Appendix B for a one-to-one comparison between our measurements and the Blanton et al data). Circularized apertures are used in this comparison, to match the Shen et al. definition. Not surprisingly,
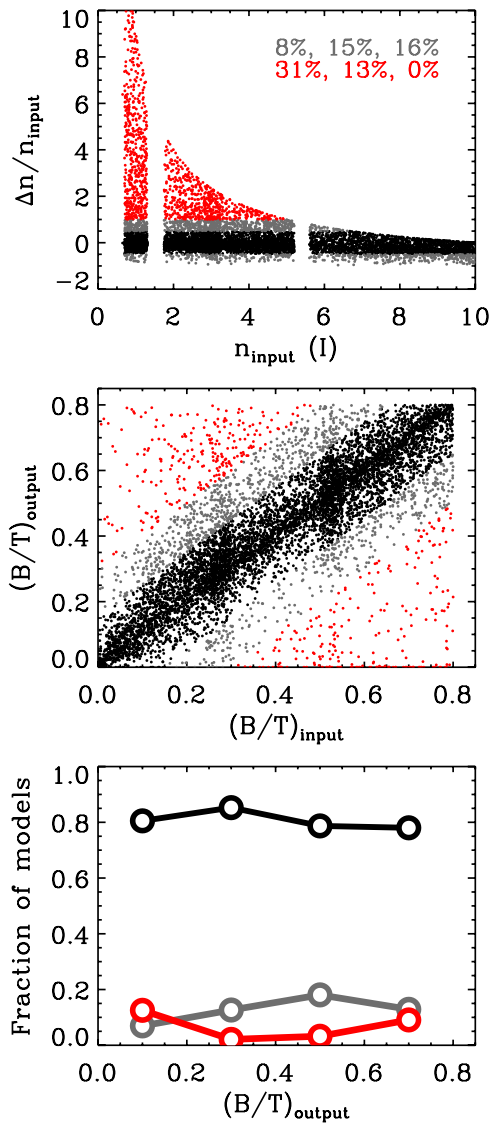
Figure 13. In the top panel we show the comparison between the intrinsic bulge Sérsic indices for the set of simulated galaxies used to test the reliability of GIM2D bulge+disk decompositions, and those recovered by GIM2D. The variation Δ corresponds to the difference between the intrinsic and measured values. With black points, we highlight models for which the structural parameters are well recovered, i.e., have relative error $<50\%$. In dark gray are the points that have a fractional error between 50% and 100%, and in gray (red in the online version) are the extreme outliers with errors which are $>100\%$. The reported fractions are the fraction of discrepant models relative to the total in the three bins of Sérsic index n shown in the figure. In the central panel we show the comparison of intrinsic and measured bulge-to-total ratios (B/T) for the model galaxies. Black shows models for which $|\Delta(B/T)| < 0.15$, dark gray those with $0.15 < |\Delta(B/T)| < 0.3$, and gray (red in the online version) is for models for which the measured B/T deviates more than 0.3 from the intrinsic value. The fraction of models within each of the three types, as a function of the *observed* B/T, is shown in the bottom panel.

(A color version of this figure is available in the online journal.)

given the global robustness of the structural parameters of disks, and more generally low Sérsic index galaxies, the Shen et al. (2003) size-mass relation for the late-type galaxies is in excellent agreement with our relation. Shen's sizes for the early-types are however systematically underestimated relative to our measurements, a difference further increased after the application of our corrections. In this respect, we note again that the SDSS data were typically acquired with a typical

r-band PSF of $\sim 1\rlap{.}{''}5$, which is comparable to the worst seeing in the I-band ZENS data, and no residual corrections as a function of size, magnitude, concentration, and inclination effects (as done in this paper) were attempted in the SDSS analysis. Using our uncorrected sizes, the difference in size estimates is $\sim 15\%$ at $> 10^{11}\,M_\odot$ and increases toward lower galaxy masses, up to $\sim 20\%$–25% at $\sim 10^{10}\,M_\odot$. The median size of the Shen et al. early-type galaxy at this latter mass scale is 1.8 kpc, while our corresponding ZENS estimate is 2.2 (2.4) kpc before (after) the application of our corrections.

We attribute the difference in size estimates between our analysis and Shen's to the combination of three factors: (1) in ZENS the half-light radii are obtained using elliptical apertures, in contrast with the circular apertures used in the SDSS study. Although we have partly corrected for this difference in a post-processing mode, by circularizing our measurements for the comparison in Figure 17, residual differences may remain. These differences are likely more relevant at relatively smaller sizes and relatively higher Sérsic indices; (2) the use of different upper limits for the Sérsic index in the SDSS and ZENS fits, see Appendix B.1; (3) different morphological mixes in the two samples, since Shen et al. use a simple split in Sérsic index to define their morphological classes; and (4) finally, of course, to the fact that the Shen et al measurements were not corrected by observational biases as we do for our ZENS sample.

7. A QUANTITATIVE MORPHOLOGICAL CLASSIFICATION FOR THE ZENS GALAXIES

7.1. Classification Criteria

The availability of a large suite of structural diagnostics for the ZENS galaxies enables us to perform an accurate and quantitative morphological classification, eliminating biases and dilution of signal in studies of galaxy properties as a function of morphology.

We classified the ZENS galaxies into six morphological classes, primarily based on the prominence of the bulge component in the I-band. These classes are, respectively, ellipticals, bulge-dominated disks—further divided into S0 and bulge-dominated spirals—intermediate-type disks, late-type disks, and irregular galaxies. The stamp images of the galaxies of different morphological types are shown in Figures 34–41 in Appendix D. A flow-chart schematic description of the steps applied in our morphological classification scheme is shown in Figure 18, in which we also list the fraction of each morphological type in the ZENS database.

In detail, our classification criteria are as follows. Ellipticals are required to be well fitted by a single Sérsic profile with *corrected* Sérsic index $n > 3$ and normalized residuals smaller than 10% out to the sky level of the image (see, e.g., Kormendy et al. 2009). We present the I-band surface brightness profiles for all elliptical galaxies in Figure 35: by definition, the light distribution of such galaxies is perfectly represented by a single (corrected) $n > 3$ Sérsic model.

The distinction among different disk types is based on the following criteria: galaxies with $B/T(I) < 0.2$ are assigned to the late-type disk class, those with $0.2 \leqslant B/T(I) < 0.5$ are classified as intermediate-type disks, and those with $B/T(I) \geqslant 0.5$ as bulge-dominated galaxies. For many reasons, including a good degree of mixing of physical classes in the visual classification of the Third Reference Catalog (RC3, de Vaucouleurs 1963), we will refrain from using its popular nomenclature. We note however that, albeit with scatter, our
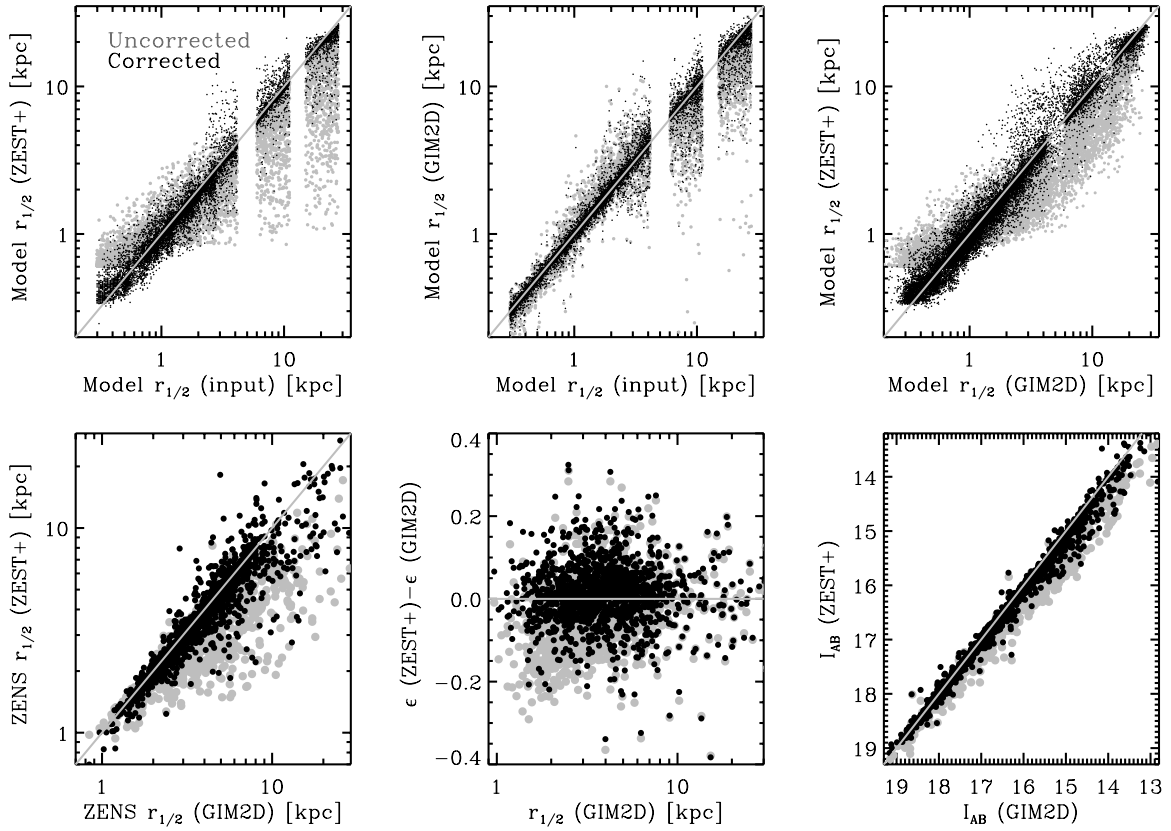
Figure 14. Tests of the correction scheme outlined in Section 6 both for the GIM2D and ZEST+ measurements on simulated (top panels) and real ZENS data (bottom panels). In all panels, black symbols are the corrected measurements and gray the raw, uncorrected measurements. The top panels specifically show the comparison between intrinsic (input) half-light radii of simulated galaxies vs. half-light radii recovered with ZEST+ (left) and GIM2D (center), and the comparison between ZEST+ and GIM2D half-light radii (right). The identity lines (shown in gray) are well matched by the corrected sizes, with systematic shifts largely cured by our correction scheme. The bottom panels show the application of our corrections to the real ZENS data. Specifically, we show the comparison between ZEST+ and GIM2D half-light radii measurements, the ellipticity differences between ZEST+ and GIM2D as a function of (corrected) GIM2D half-light radius, and the comparison between *I*-band magnitudes recovered by ZEST+ and GIM2D. Also in these case, large discrepancies observed in the raw measurements vanish once we apply our correction scheme.
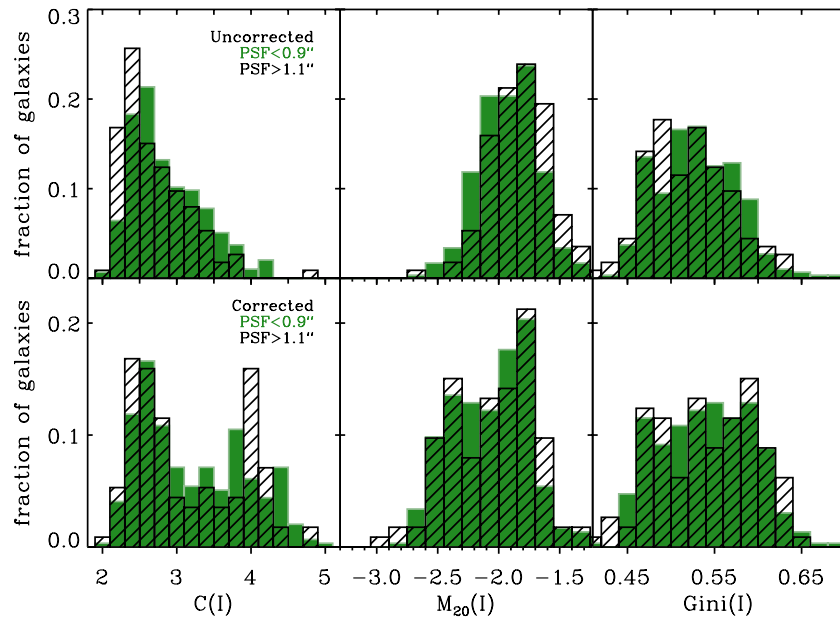
Figure 15. Comparisons of the distributions of ZEST+ concentration (left), M_{20} (center), and Gini (right) *I*-band parameters before (top row) and after (bottom row) the application of our correction scheme to eliminate PSF-induced biases. The distributions are shown for two separate bins of PSF FWHM, i.e., FWHM $<0''9$ (gray histograms, green in the online version) and FWHM $>1''1$ (black histograms). Galaxies observed with smaller PSF appear more concentrated than those observed with a larger seeing, a consequence of the blurring of the structural features caused by the PSF size. Also, the effect of PSF-blurring is to move high-concentration, highly negative M_{20} galaxies to lower concentration, less negative M_{20} regions of parameter space. Both biases are eliminated by our correction scheme.

(A color version of this figure is available in the online journal.)
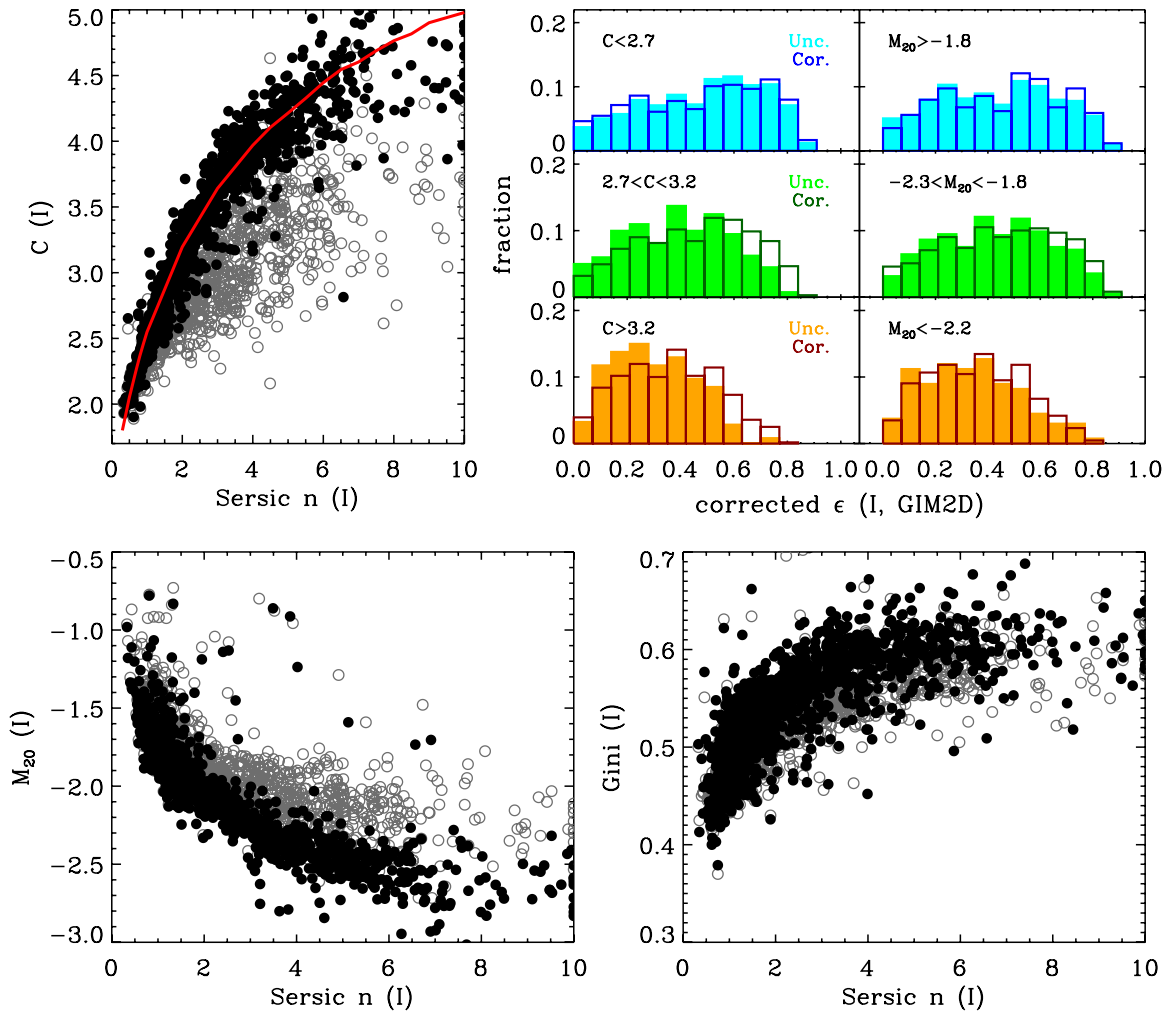
Figure 16. Relation between the *I*-band Sérsic index *n* and non-parametric structural quantities, i.e., C, M_{20} and Gini coefficients before and after applying our correction scheme described in Sections 6.5 and 6.3 (top left panel and bottom panels). Gray points show the uncorrected measurements and black points the corrected measurements. In the upper left panel, the solid gray (red in the online version) line marks the values of the concentration index that are theoretically expected for a pure Sérsic profile of a given *n*. Both C and M_{20} require substantial corrections while the Gini coefficient is largely unaffected by observational biases. The upper central and right panels finally show, for galaxies classified as disks in Section 7 (S0 and later-types), the dependence of uncorrected and corrected concentration and M_{20} parameters on ellipticity. Specifically, we present the distribution of ellipticity for galaxies divided in three bins of concentration and M_{20}, as indicated by the Figure legend. The filled light histograms are for the uncorrected parameters, the dark empty ones for the corrected indices. The uncorrected C and M_{20} values show a bias with ϵ which is removed by our correction procedure.

(A color version of this figure is available in the online journal.)

bulge-to-total separation for disk galaxies roughly corresponds to a division in types S0 plus S0a/Sa, Sab/Sbc, and Sc/Sm, in order of decreasing B/T range.

Both S0 and spiral galaxies with large bulges fall in the bulge-dominated galaxies category. The distinction between the two is based on the *B*-band smoothness parameter ($S_{B\text{-band}}$), which is set to <0.01 for S0 and larger than this value for early-type spirals, except in those cases where faint spiral arms—not prominent enough to cause a variation of the smoothness parameter—are clearly seen in the visual inspection of the images. For nearly edge-on systems, it is obviously impossible to determine the presence or absence of spiral arms and the difference between S0 and bulge-dominated spiral galaxies becomes more challenging. Given that we have no means to securely distinguish these morphological types at these high inclinations, we assigned to the bulge-dominated spiral class those galaxies which satisfy the B/T criterion above and either present a dust lane in the disk plane or have a high *B*-band smoothness parameter ($S_{B\text{-band}} > 0.01$). As seen in Figures 36

and 37, a large fraction of the highly inclined galaxies are classified as bulge-dominated spirals, and only those which clearly do not have a dusty disk are defined as S0. The contamination of S0 galaxies into the bulge-dominated spiral class is hence likely non-negligible at the highest inclinations; a comparison between the relative fractions for face-on galaxies estimates this contamination at the 33% level.

The distinction between S0 and elliptical galaxies is also non-trivial, this time especially in face-on systems. To attempt to distinguish between these two classes we inspected all the residuals of the single component fits and any sign of a faint disk component was used as a discriminant diagnostic. Finally the *B*-band smoothness *S* parameter was used to further validate the separation between the two types by requiring that for S0 $S_{B\text{-band}} > 0.003$, a condition which is however secondary to the fact of S0 not being perfectly fit by a single Sersic model.

We note that for ∼15% of all ZENS galaxies that were not classified as ellipticals or irregulars, and that would therefore be assigned a "disk" classification, it was not possible to obtain a
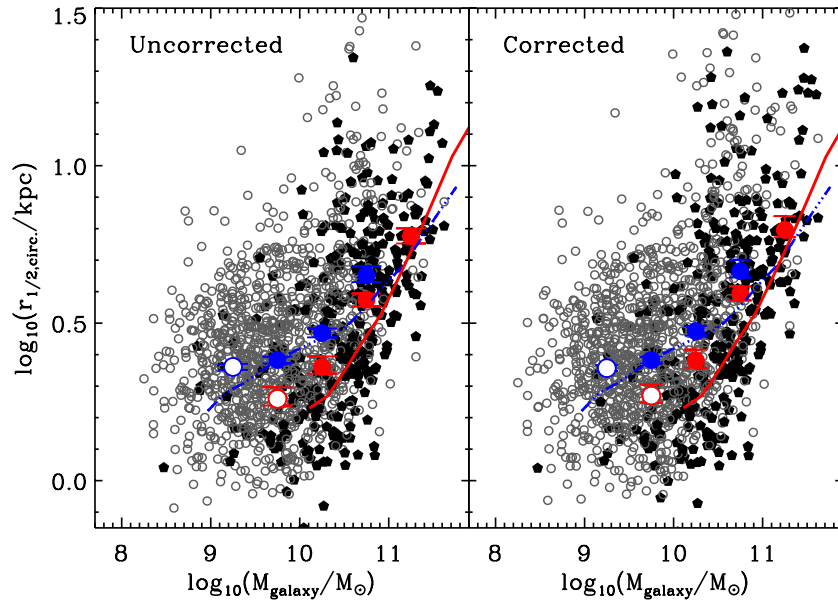
Figure 17. Comparison of the mass–size relation between our ZENS sample and the early- (solid line, red in the online version) and late-type (dashed-dotted line, blue in the online version) samples of Shen et al. 2003. Shen's solid and dashed-dotted lines connect median values of sizes in the corresponding stellar mass bins (adapted from their Figure 11). The left panel shows results before applying to our data the corrections described in Section 6.3; our corrected sizes are shown in the right panel. Empty gray circles are ZENS galaxies classified as intermediate- and late-type type disks; filled pentagons are ZENS ellipticals, S0s, and bulge-dominated spirals. The median values for these two broad ZENS morphological samples are shown with large circles (E, S0, and bulge-dominated spirals grouped together; red in the online version) and large triangles (intermediate-type and late-type disks group together; blue circles in the online version). White large symbols indicate ZENS data in mass bins below the ZENS mass completeness for the relevant morphological types. The major axis ZENS radii are circularized in post-processing mode in this figure for a better comparison with the SDSS sample.

(A color version of this figure is available in the online journal.)
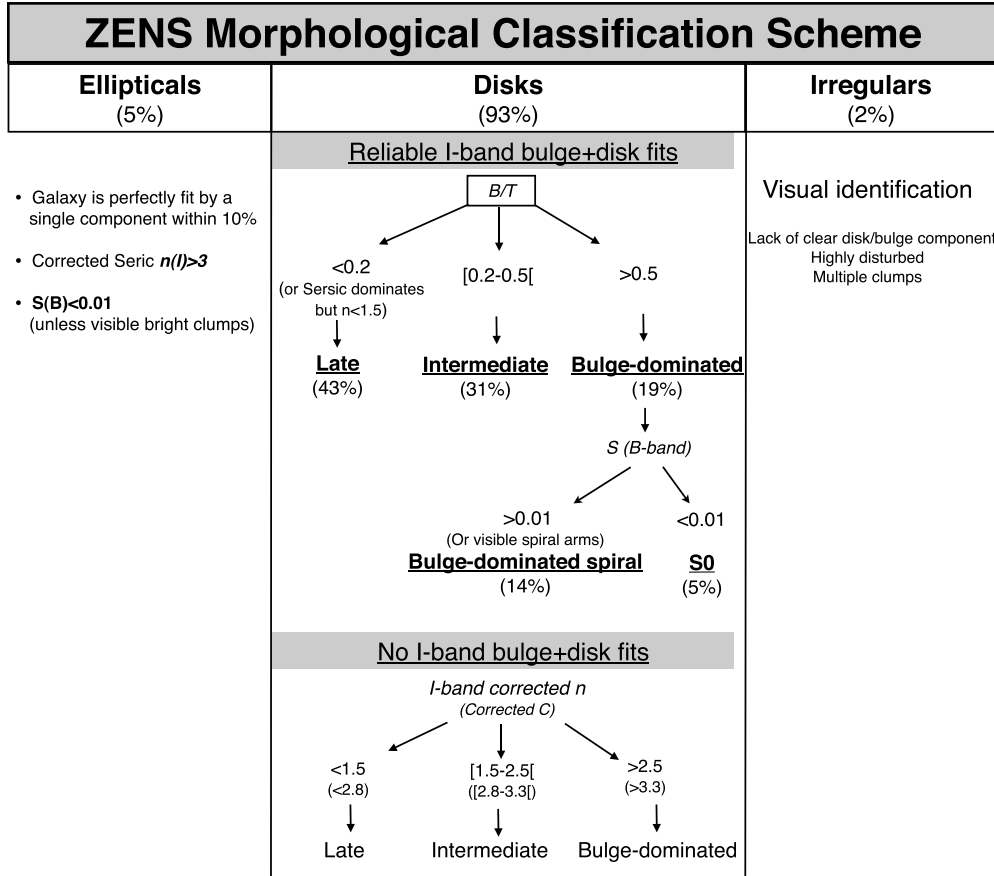
Figure 18. Schematic description of the steps adopted for the ZENS morphological classification. The numbers in parenthesis provide the fraction of galaxies assigned to the different morphological classes with respect to the total ZENS sample.
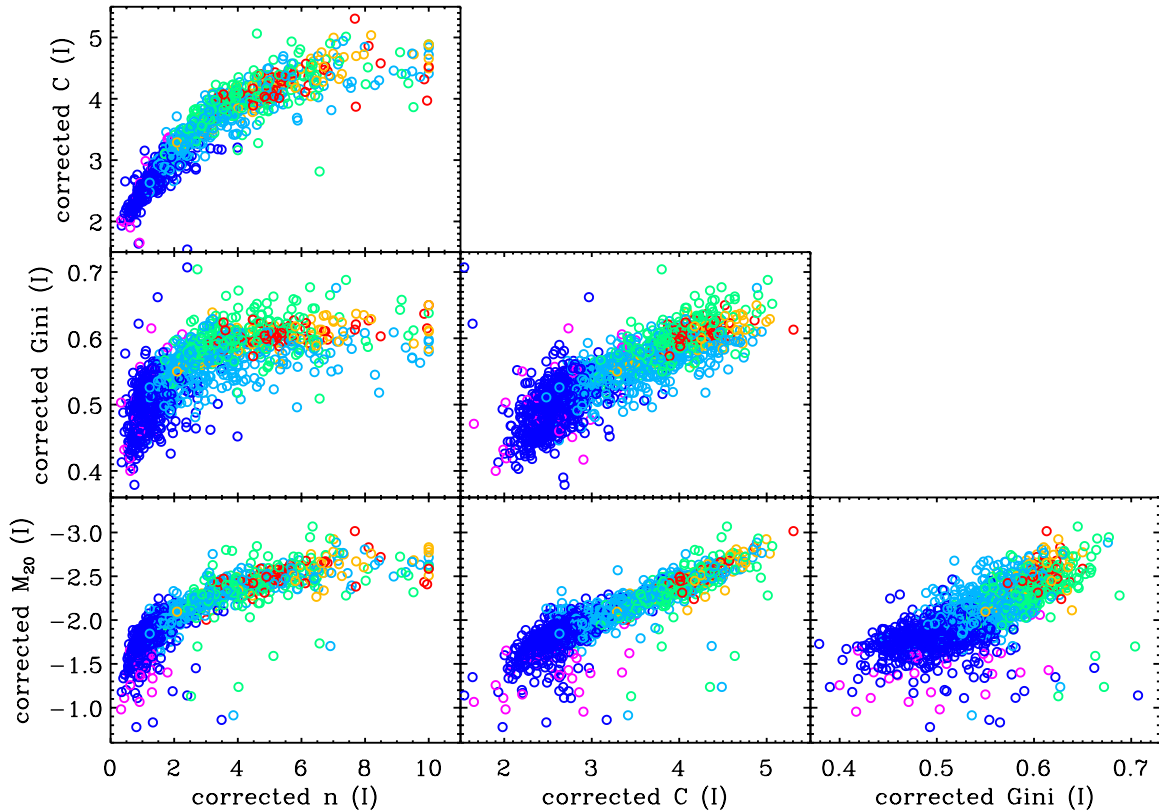
Figure 19. Location of the different morphological classes in the $C - Gini - M_{20} - n$ planes. The colors highlight the five morphological classes: red, ellipticals; orange, S0; green, bulge-dominated spirals; cyan, intermediate-type disks; blue, late-type disks; and magenta, irregulars.

reliable *I*-band bulge+disk decomposition (see Appendix B). In these cases the classification is based on the corrected Sérsic indices from the single component fits, as shown in the right hand side of Figure 18. For the very few galaxies (∼1%) for which we could not obtain any reliable bulge+disk decomposition or Sérsic index, we used the *corrected* ZEST+ parameters (in particular the concentration) to define their morphological class. Specifically, in such few cases, galaxies with $C < 2.8$ were assigned to the late-type disk class, those with $2.8 < C < 3.3$ to the intermediate-type disks, and galaxies with $C > 3.3$ to the bulge-dominated spiral class. The precise values of these cuts were determined through the relation between *n* and *C* in Figure 19.

Irregular (i.e., thus possibly disturbed by mergers/ encounters) galaxies are identified in the ZENS sample by visual inspection; in this category we included those galaxies which have no clear disk/bulge component or have a highly disturbed morphology characterized by multiple clumps, as shown in Figure 40.

There are furthermore 26 galaxy-pairs or triplets in the ZENS sample that are also possible merger candidates, of which we show stamp images in Figure 41. These galaxy pairs are identified as single objects in 2dFGRS, and appear as single members in the group catalog, i.e., they have only one redshift measurement in the 2dFGRS catalog. For nine of these systems, we confirmed with SDSS (York et al. 2000) spectral or photometric redshifts, or with spectroscopic data available in the NED database, that the two galaxies are at the same redshift, strengthening the hypothesis that they are undergoing a merger event. There are 17 remaining galaxy pairs, for which no such information is available. We note that five pairs/triplets show tidal features and disturbed morphologies,

supporting the merger scenario; the remaining 12 pairs display less clear signs of interaction, and so a chance projection cannot be excluded for them. We will nonetheless include the latter in the sample of merger galaxies and, when necessary, test our results with and without these systems. These are flagged as "possible projections" in our ZENS catalog.

For consistency with the original 2dFGRS and 2PIGG catalogs, we count merging galaxies as a single galaxy pair system in the sample of 1455 galaxies, but we compute and provide photometric/structural properties for the individual members (thus making 1484 total entries in the public ZENS catalog). In the "normal" disk population, there are also some galaxies that present clear tidal features and disk distortions; such galaxies are flagged has having plausibly undergone a recent galaxy–galaxy interaction or merger. Finally we also flag as candidate mergers those ZENS galaxies which, although identified as individual objects in the parent 2dFGRS/2PIGG catalog, are found at a distance from another confirmed group member smaller or equal to the maximal separation observed in the above 26 galaxy pairs (i.e., 48″, roughly 50 kpc at the average ZENS redshift) and have a velocity difference from it $\Delta v \leqslant 500$ km s^{-1}. The properties of merger galaxies in the ZENS sample and the connection with the local and large-scale environment are investigated in a forthcoming publication (A. Pipino et al. 2013, in preparation).

7.2. Structural Properties of the Different Morphological Classes

Our morphological classification scheme is primarily based on a bulge-to-total ratio separation. We inspect in Figure 19 the distributions of the *corrected C, n*, Gini, and M_{20} for the various morphological classes, and we summarize in Table 2 the median

Table 2
Median Values of the Corrected Structural Diagnostics for the Different Morphological Classes in Bins of Ellipticity

Type	$\langle C \rangle$	$\langle \mathrm{Gini} \rangle$	$\langle M_{20} \rangle$	$\langle S \rangle$	$\langle n \rangle$	$\langle B/T \rangle$
E	4.11/ ⋯ / ⋯	0.60/ ⋯ / ⋯	−2.45/ ⋯ / ⋯	0.005/ ⋯ / ⋯	4.93/ ⋯ / ⋯	⋯ / ⋯ / ⋯
S0	4.24/4.19/ ⋯	0.60/60/ ⋯	−2.48/−2.49/ ⋯	0.006/0.0064/ ⋯	5.19/ 4.64	0.62/0.63/ ⋯
Bulge-dom. Spiral	3.88/3.94/3.92	0.59/0.59/0.61	−2.30/−2.37/−2.41	0.033/0.043/0.096	3.90/3.94/3.39	0.59/0.58/0.60
Interm.-type Disk	3.54/3.42/3.16	0.56/0.55/0.56	−2.20/−2.15/−2.11	0.020/0.043/0.10	2.91/2.52/2.01	0.36/0.35/0.31
Late-type Disk	2.58/2.60/2.56	0.48/0.49/0.51	−1.80/−1.79/−1.81	0.040/0.050/0.087	1.14/1.14/1.09	0.04/0.07/0.03

Notes. The median values of the corrected non-parametric diagnostics measured in the three ellipticity bins $\epsilon < 0.33$, $0.33 < \epsilon < 0.55$, and $\epsilon > 0.55$ from the lowest to the highest ellipticity. Note that ellipticals and S0s have only one and two bins of ellipticity, respectively. Note also that the dependence on ellipticity of non-corrected C and M_{20} values for disk galaxies shown in Figure 16 is largely eliminated by our correction scheme.

values of these corrected non-parametric diagnostics for each morphological class, separately in three bins of ellipticity (i.e., inclination for disk galaxies). Note that the six morphological classes largely segregate in specific region of the structural planes. Again we stress that this consistency between B/T and non-parametric diagnostics is reached only after correcting the latter as described in Section 6. The raw measurements before the implementation of the corrections would substantially mix different galaxy populations (e.g., through biased concentration and M_{20} estimates, see Figures 15 and 16)—a bias which could affect other published analyses based on (uncorrected) non-parametric diagnostics.

There are of course some noticeable deviations that remain, even after correcting the non-parametric diagnostics. A small number of galaxies classified as intermediate- or late-type disks have low M_{20} indices for their concentration or Gini values, overlapping with the region of the plane which is mostly occupied by irregular galaxies. We visually inspected all these galaxies and verified that the M_{20} deviations are mostly caused by the presence of bright clumps in the galaxies outskirts, but that a clear and ordered disk structure is present (we highlight these galaxies with a "*" in Figures 38 and 39).

Also, some intermediate-type disk galaxies have relatively high concentration values ($C(I) > 4$). This demonstrate that concentration is *not* necessarily a proxy for the fractional contribution of the bulge component to the stellar light, as also pointed out by other authors (e.g., Scodeggio et al. 2002). There is, of course, a correlation between B/T and C characterized by a linear correlation coefficient of $\mathcal{R} = 0.86$. However, the scatter is large and a given concentration value can be associated with a broad range of B/T ratios, as illustrated in the top right panel of Figure 20. We emphasize that the *uncorrected* values of concentration lead to a much larger scatter, which results in a weaker correlation between B/T and uncorrected C with $\mathcal{R} = 0.78$.

We highlight with colors in Figure 20 two regions of parameter space worth noticing, i.e., galaxies with $B/T < 0.35$ and $C > 3.5$ (red points) and those with $C < 3.5$ and $B/T > 0.45$ (blue points). As illustrated in the bottom panels of the same figure, highly concentrated galaxies with low B/T ratios are found below the bulk of the population in the relation between the bulge half-light radius and the disk scale length; the Sérsic indices of their bulges are, in most of the cases ($\sim 70\%$), above 2.5. Such objects host dense but small bulges, which are causing an increase in the concentration value but do not give a major contribution to the total galaxy light. The blue points at low C and high B/T, in contrast, are galaxies with typically extended bulges with low Sérsic index (i.e., pseudo-bulge-like structures, see, e.g., Carollo 1999; Carollo et al. 1998, 2007;

and Kormendy & Kennicutt 2004 for a review and further references).

In Figure 21 we show the different corrected structural indices for the morphological classes as a function of the galaxy inclination. The distribution of corrected parameters for each individual class are fairly flat with ellipticity, as they should be (in contrast with the non-corrected parameters, which we have shown to have a bias with ellipticity; see Section 6.7 and Figure 16). Note that galaxy smoothness maintains a substantial dependence on inclination by increasing toward higher inclinations; this parameter has not been corrected, since we used only smooth galaxy models to determine our correction matrices. Part of the dependence of S on ellipticity might thus be a residual observational bias; part might however be a consequence of the prominence of dust lanes in edge-on galaxies.

Dust absorption in the disk could also, in principle, artificially lower the derived bulge-to-total ratios for edge-on galaxies (see, for example, Driver et al. 2007), and thus introduce a bias in the B/T-based morphological classification. We expect this effect to be minimal in our analysis, since we use the relatively unaffected I band to derive our fiducial B/T estimates, but it is nonetheless worthwhile to test whether there are indications of biases among the morphological classes given that some attenuation of the disk (and bulge) light is certainly occurring.

In the lower right panel of Figure 21, we plot the distributions of ellipticity for disk galaxies with bulge-to-total ratio <0.2 (blue histogram), $0.2 < B/T < 0.5$ (green histogram), and $0.5 < B/T < 0.8$ (red histogram). For $\epsilon \lesssim 0.6$, we find a reasonable constancy with ellipticity of the relative contribution of three disk types to the total disk population, indicating that there are no major biases in this regime. At higher axis ratios, there is a depletion of $B/T > 0.2$ galaxies and an increase of the "bulgeless" disk galaxies, which we interpret mostly to be a consequence of a true change in the morphological mix rather than of strong dust absorption. The presence of a bulge component, even in highly inclined disks, produces a rounding of the isophotes and thus of the measured axis ratio. Therefore, the decrease in the number of bulge-dominated galaxies and intermediate-type disks at $\epsilon \gtrsim 0.6$ likely reflects this correlation between "morphology" and measured ellipticity. Likewise, the peak of $B/T < 0.2$ disk galaxies at $\epsilon \simeq 0.7$ can be explained by the "rounding" of isophotes due to PSF effects in these galaxies and the intrinsic galaxy thickness. Indeed no galaxy is observed at $\epsilon > 0.90$, and the fraction of $B/T < 0.2$ disk galaxies with $0.6 < \epsilon < 0.90$ relative to the total sample of disk galaxies is $\sim 25\%$, i.e., if they were (infinitely thin disks and) equally distributed up to $\epsilon = 1$, each of the four 0.1-wide bins between $0.6 < \epsilon < 1$ would contain 6% of the
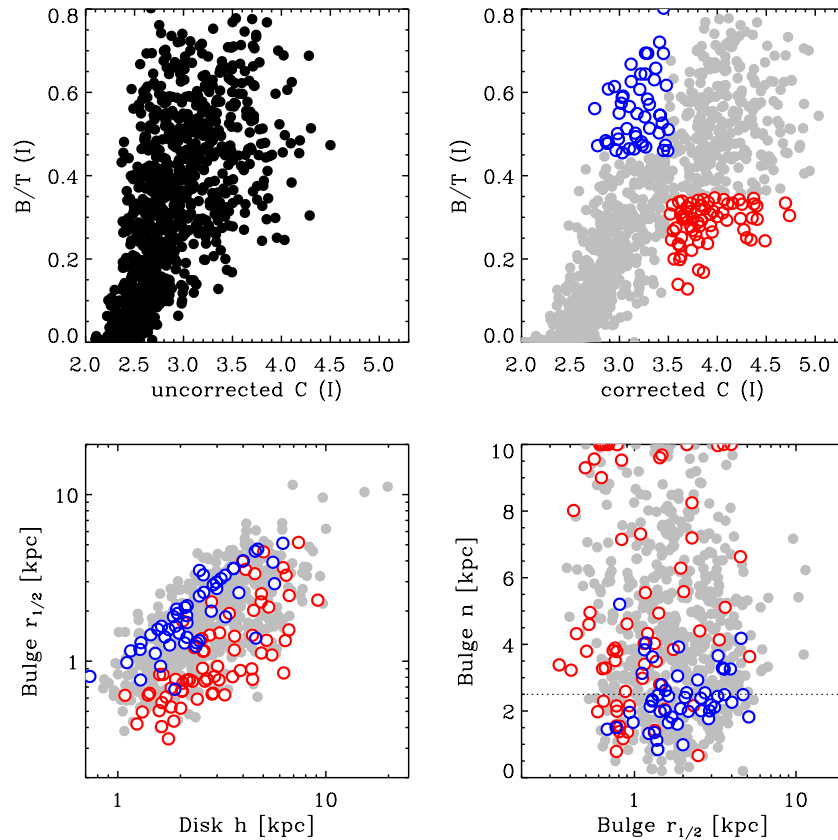
Figure 20. *I*-band relation between bulge-to-total ratio and uncorrected (top left panel) and corrected (top right panel) concentration for the ZENS disk galaxies with bulge-to-disks analytical fits. In the plot with corrected-*C* values, galaxies that are concentrated ($C > 3.5$) but have a low bulge-to-total ratio ($B/T < 0.35$) are highlighted with circles (red in the online version). Galaxies that have low concentration ($C < 3.5$) and high $B/T > 0.45$ are highlighted with filled squares (blue in the online version). Note the large scatter in the corrected-*C* vs. B/T relationship, which makes *C* a poor morphological indicator. Note also that uncorrected-*C* values are, as expected, even worse representatives of the galaxy B/T (and thus physical morphology) properties. The two bottom panels show, from left to right, the *I*-band bulge half-light radius vs. disk scale length plane and the *I*-band bulge Sérsic index vs. bulge half-light radius plane. The symbols (colors) in these plots represent the galaxy populations highlighted in the B/T vs. corrected-*C* plane.

(A color version of this figure is available in the online journal.)

samples, which is the average number observed at lower axis ratios.

To further test whether the estimates of galaxy bulge-to-total ratio are strongly affected by dust extinction, we compare in the bottom panel of Figure 21 the difference between the B/T values measured in the *B* band and those measured in the *I* band as function of the galaxy ellipticity. In grey we show the full ZENS sample; other colors for the results for galaxy samples split in the three B/T classes are discussed above. The *I*-band B/T values are typically larger by about 5% than those in the *B* filter, which is consistent with larger dust absorption effects at the shorter wavelengths. There is, however, no clear variation with ϵ of the difference $B/T(I) - B/T(B)$ within each of the three morphological classes. We thus conclude that dust effects are generally a modest contribution to the total error budget for the B/T measurements, which is dominated by other sources of random and systematic errors (see Figure 13 and the corresponding discussion in the text).

We note that other authors have combined empirical disk attenuation–inclination relations with theoretical dust models in order to derive inclination-dependent corrections for dust absorption in bulge and disk fluxes (e.g., Driver et al. 2007, 2008). Using the *I*-band parameters in Table 1 of Driver et al. (2008) together with their Equations (1) and (2), we estimate a correction of order of $\Delta B/T \simeq 0.1$ to the ZENS

I-band B/T values, comparable with or even smaller than the typical uncertainty on the B/T measurements. While such corrections could be important in some contexts, they inherit the uncertainties on the adopted dust models and would not cause a significant shift of morphological class in the ZENS sample. We hence choose not to apply any such (model-dependent) dust correction, and to adopt the dust-uncorrected `GIM2D` measurements of B/T as our fiducial estimates for this parameter.

In summary, the above considerations and the constancy of the median B/T ratio for the different morphological classes in three ellipticity bins shown in Table 2 lead us to conclude that our B/T measurements are largely independent of the axis ratio and that our morphological classification is thus largely unaffected by inclination effects.

As a final remark, we note that the *n* Sérsic indices of intermediate-type disks also show a residual (but marginal) dependence on ellipticity. This is, of course, the morphological class for which the likely similar light contribution of bulge and disk components along the line-of-sight is the most difficult to disentangle. Nevertheless, the *n* values spanned by this morphological class at the different ellipticities are consistently in the "intermediate" range of $n \sim 2$–2.8 (see Table 2), providing a consistent characterization of these systems across the whole ellipticity range.
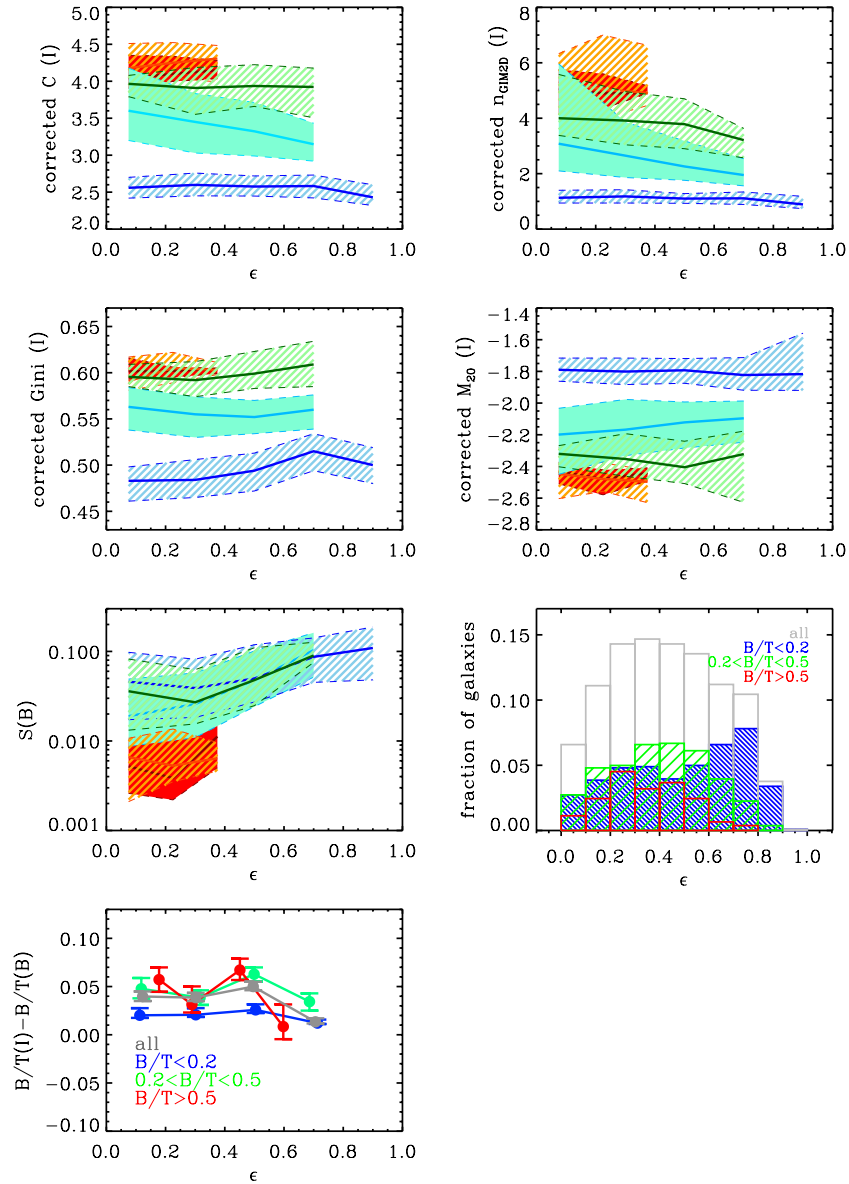
Figure 21. Shaded areas show the distribution of structural parameters (concentration, Sérsic index, Gini coefficient, M_{20} index, and smoothness) as a function of measured ellipticity ϵ for galaxies of different morphological types. The color scheme reflects the morphological class: red, elliptical galaxies; orange, S0; green, bulge-dominated spirals; cyan, intermediate-type disks; and blue, late-type disks. The distributions are calculated in bins of 0.15 in ellipticity for ellipticals and S0—which span a smaller range of ellipticity—and in bins of 0.2 for all the other morphological types. The thick solid lines mark the median values and the shaded areas the 25th and 75th percentiles. Note the good segregation in parameter space achieved by different morphological classes based on a B/T criterion; this is the result of our correction scheme, which eliminates observational biases (especially PSF-induced biases) from the measurements of the non-parametric estimators of galaxy structure. The panel on the bottom-right presents the distribution of ellipticities for galaxies with I-band $B/T < 0.2$ (blue histogram), $0.2 < B/T < 0.5$ (green histogram), and $0.5 < B/T < 0.8$ (red histogram) normalized to the total number of galaxies with available I-band B+D decompositions, for which the global distribution is shown in gray. Finally, the bottom-left panel shows the difference between the I-band and B-band B/T in four bins of ellipticity. Colors are as above; the points are located on the x-axis at the median ellipticity of each given bin. The good agreement between the I- and B-band B/T measurements gives confidence that the B/T estimates are largely unaffected by inclination effects.

8. THE CONCENTRATION OF SATELLITES GALAXIES OF DIFFERENT HUBBLE TYPES IN DIFFERENT ENVIRONMENTS

The main goal of ZENS is to study galaxy properties, at fixed stellar mass and Hubble type, as a function of several environmental parameters derived self-consistently for the same galaxy sample, i.e., the host halo mass, the large-scale density $\log(1 + \delta_{\mathrm{LSS}})$, and the projected group-centric distance. We furthermore split the ZENS galaxy sample in central galaxies into their host group halos and satellite galaxies, which orbit the central galaxies within those halos (see Paper I for the precise definition of central and satellite galaxies, and for the environmental parameters). Several analyses are underway that use the ZENS database, including the structural and morphological information derived in this paper, to investigate how galaxy structural and morphological properties vary across the different environmental regimes.

In this second paper in the ZENS series, we want to show a first utilization of the structural measurements presented above to answer, from a purely observational perspective, a simple question, namely how the concentration of *satellite galaxies* depends, at fixed stellar mass, on (1) Hubble type and (2) on group mass, group-centric distance, and LSS density.
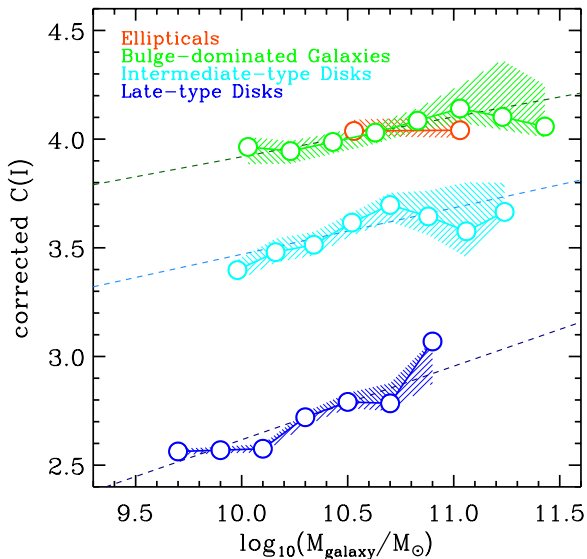
Figure 22. Corrected concentration C vs. galaxy stellar mass (from Paper III), for satellite galaxies and different Hubble types defined in Section 7 (S0 and bulge-dominated spirals are joined together in the broad bulge-dominated galaxies class). The points connected with lines show the median galaxy concentration, calculated over a running box of width 0.3 dex in mass for intermediate-type and late-type disks, and of width 0.4 dex for the earlier types. The dashed lines are the best linear fits to the observed relations over the mass range probed by all morphological types, i.e., for masses above $10^{10} M_\odot$. The shaded areas correspond to the 1σ error bars on the median values.

(A color version of this figure is available in the online journal.)

8.1. The Role of Hubble Type at Fixed Stellar Mass

Galaxy structure, as described by the concentration parameter, is a strong function of galaxy mass (e.g., Kauffmann et al. 2003; van der Wel 2008). As we have discussed above, concentration is however a relatively poor indicator of galaxy morphology (when this is defined according to a more physical parameter such as the bulge-to-total ratio, as we do for the ZENS galaxies). Furthermore, morphology also is a function of stellar mass (see Paper III and also, e.g., Pannella et al. 2006; Bamford et al. 2009; Oesch et al. 2010; Bernardi et al. 2010; Vulcani et al. 2011). With available robust (corrected) concentration values and a B/T-based morphological classification, we thus investigate how much of the concentration versus galaxy stellar mass correlation is to be ascribed to a variation in the Hubble type of galaxies and how much is actually driven by a real change in concentration within each individual morphological type. Stellar masses are taken from Paper III. The results of this analysis will also help us interpret the analysis of satellites' concentration in the different environmental parameters, for which, in order to gain statistics, we will use broader morphological classes.

Figure 22 shows the corrected concentration as a function of galaxy stellar mass. The points connected with lines are the median concentrations for satellite galaxies divided according to the morphological types (note that S0 and bulge-dominated spiral galaxies are joined together into a single broad morphological bin of "bulge-dominated" galaxies). The medians were calculated using a running box above the mass completeness of each morphological type (the results are noisier but consistent when using independent mass bins). The inspection of this figure shows an increase in concentration with increasing galaxy stellar mass at fixed morphological type for disk galaxies. Specifically, our elliptical satellites' sample covers a small range of stellar mass ($\sim 10^{10-10.5} M_\odot$), over which the

concentration is observed to remain constant. For all types of disk galaxies where the range of masses covered is larger, a trend of concentration with stellar mass is clearly observable, separately for each morphological disk type (the latter defined according to the galaxy bulge-to-total ratios as described in Section 7). We note that residual bulge-to-disk variations with stellar mass *within* each morphological disk class are possible, since our morphological classification was done independent of galaxy stellar mass, and each morphological bin covers a relatively broad range of bulge-to-total ratios. Quantitatively, however, the a posteriori computation of the median bulge-to-total ratios vary, between the mass bin centered at $10^{10} M_\odot$ and the mass bin centered at $10^{10.7} M_\odot$, only from 59% to 60%, 34% to 36%, and 7% to 12%, respectively, for bulge-dominated, intermediate-type, and late-type disk galaxies. Thus, we conclude that the known concentration–mass correlation is not solely driven by a correlation between morphological type and stellar mass, but is at least partially driven also by a genuine increase in concentration of galaxies of similar Hubble type, i.e., of similar bulge-to-total ratio.

We fit the observed trends of corrected concentration versus galaxy stellar mass with a linear relation, $C = \alpha + \beta \log(M/M_\odot)$, in the mass range that is probed by all morphological types, i.e., for those bins which are above $10^{10} M_\odot$ for their full width. The global $C-M$ relation for the late-type disks shows a break around $\sim 10^{10} M_\odot$, below which mass the relation flattens; a linear fit is, however, a good approximation at $M > 10^{10} M_\odot$ where we can make a meaningful comparison with the other types. The slopes β for the four morphological classes above this threshold mass are, respectively, $\beta_{\text{bulge-dom}} = 0.18 \pm 0.04$, $\beta_{\text{interm.-type}} = 0.21 \pm 0.07$, and $\beta_{\text{late-type}} = 0.34 \pm 0.15$. Satellite elliptical galaxies are consistent with no dependence of concentration on the galaxy mass, i.e., $\beta_{\text{ellipticals}} = 0$. However, as commented above, the lack of dependence of C on stellar mass for the ellipticals is established only across a relatively limited mass range. Generally speaking, this finding follows the global trend, established on the disk galaxies, of a flattening of the C versus galaxy stellar mass relation from the later to the earlier morphological type.

8.2. The Dependence of (Disk) Satellite Concentration on LSS Density, Group-centric Distance, and Group Halo Mass

At the masses of our study, there are essentially no irregular satellite galaxies; furthermore, elliptical galaxies contribute only 5% to the total number of satellites in the ZENS sample at these masses. The small number of elliptical satellites does not enable us to perform a statistically significant analysis of their dependence on environment. Since the vast majority ($\sim 95\%$) of satellites in the sample are disk galaxies, we choose to maximize morphological "purity" in our analysis of the dependence of satellite concentration on the different environmental parameters by limiting it to the sample of *disk* satellites only.

In Figure 23 we present the (corrected) concentration versus galaxy stellar mass relation for disk satellite galaxies, split into two broad morphological bins of "bulge-dominated" galaxies and "disk-dominated" galaxies by adding together S0s and bulge-dominated spirals in one bin, and intermediate-type and late-type disks in the other. The relation is plotted separately as function of group mass M_{GROUP}, LSS (over)density δ_{LSS}, and group-centric distance R_{R200} (from top to bottom). The broad bulge-dominated galaxies bin is split into three bins of galaxy stellar mass, i.e., $\log(M/M_\odot) \in [9.5, 9.9[, [9.9, 10.45[,$
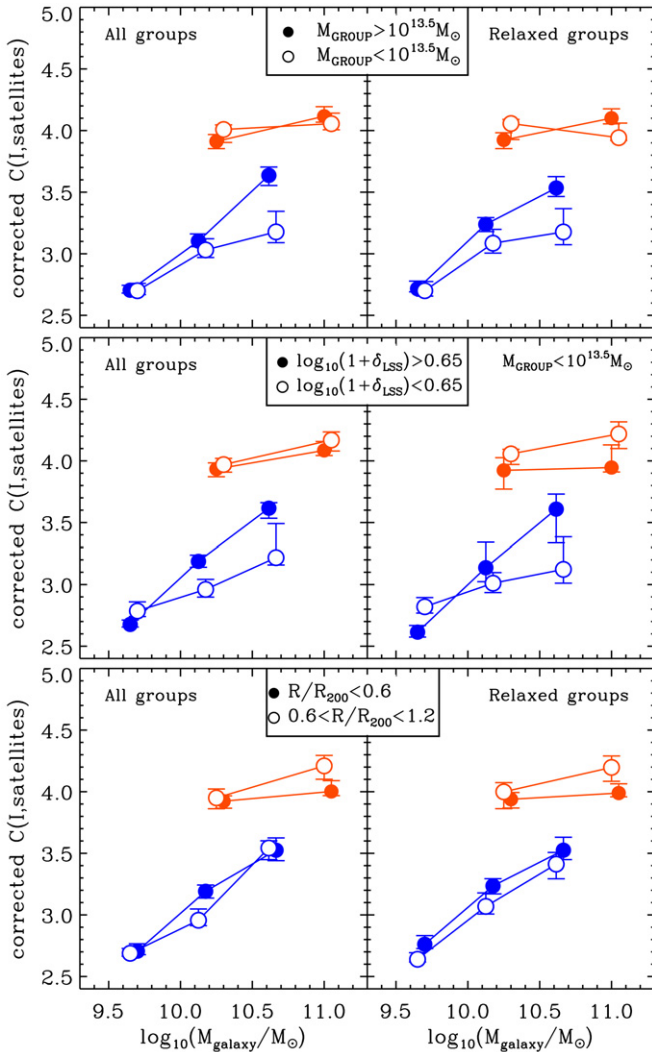
Figure 23. Panels show the corrected concentration parameter C as a function of galaxy stellar mass, split in bins of environments as follows: top panels show the dependence on group mass M_{GROUP}; central panels on LSS (over)density δ_{LSS}; and bottom panels on group-centric distance (R/R_{200}). Only disk satellites are shown in this analysis. These are split in two broad bins of morphologies, specifically bulge-dominated galaxies (which include bulge-dominated spirals and S0 galaxies; grey circles, red in the online version) and disk-dominated galaxies (which include intermediate-type and late-type disks; black squares, blue in the online version). For all three environmental indicators, filled symbols show results for the "denser" bin and empty symbols for the "lighter" bin. In the top and bottom panels, left plots are for all ZENS groups and right plots for relaxed groups only (see text). In the central panels, the left plot shows again results for all groups, but this time the right plot shows results for groups with $M < 10^{13.5} M_\odot$ only, to avoid spurious effects with group mass when studying the effects of the LSS density field. Galaxies located at a radial position $R > 1.2R_{200}$ are excluded from the analysis. Symbols are positioned at the center of any given mass bins with a small offset between denser/lighter environments applied for visual clarity.

(A color version of this figure is available in the online journal.)

[10.45, 10.88]; we use only two bins of galaxy stellar mass for the broad bulge-dominated galaxies bin, i.e., $\log(M/M_\odot) \in$ [10., 10.6[, >10.6.

Before discussing the results, we present some considerations on the biases and uncertainties which may affect the analysis. First, we remind that trends with group mass that we measure are, intrinsically, possibly even stronger. As discussed in Paper I, the uncertainty on our group mass estimates tends to "wash out" trends with this environmental quantity; quantitatively, real

trends with group mass have slopes $\approx$1.3–1.4 steeper on average than what we can measure in the ZENS sample.

In Paper I we furthermore discuss a classification of the ZENS groups into "relaxed" and "unrelaxed" groups according to whether a self-consistent solution for a central galaxy can be found (relaxed groups) or not (unrelaxed groups). The latter are expected to be a combination of genuinely dynamically young, merging structures contaminated by physically relaxed groups for which several observational biases prevent us from properly identifying their central galaxy. In the spirit of checking that our results are not affected by the inclusion of the unrelaxed groups in our studies, in Figure 23 we show the results for all ZENS groups (left panels) and for the subset of relaxed groups only (right panels) when studying the dependence of the C-mass relation on either M_{GROUP} or R_{R200}.

We furthermore exclude from the following analysis those galaxies which are located at group-centric distances $R > 1.2R_{200}$. In some of the ZENS groups relatively massive galaxies are found to lie in the outskirts of the group. As discussed above, this is partially a consequence of observational limitations but it may also be the signature of on-going accretion of sub-haloes. The sample selection at $R < 1.2R_{200}$ thus helps minimize the contamination at these large radii of in-falling substructures and maximize the "purity" of galaxies that are satellites within a single common halo.

In Paper I we also comment on the fact that, at group masses above $\sim10^{13.5} M_\odot$, group mass M_{GROUP} and LSS (over)density δ_{LSS} are correlated by nature, since massive groups are found by definition only in dense regions of the LSS. In contrast, groups of masses $<10^{13.5} M_\odot$ are found at any value of δ_{LSS}. It is thus possible to disentangle the effects of M_{GROUP} and δ_{LSS} by limiting the studies as a function of δ_{LSS} to group masses below this threshold. We adopt this strategy here as well, and, in order to search for a dependence of the C-mass relation for satellites on δ_{LSS}, we test that the results obtained when including all groups in the analysis with δ_{LSS} (left central panel) hold also when restricting the group sample to groups with $M_{GROUP} < 10^{13.5} M_\odot$ (right central panel).

Having established that the concentration parameter is a function of both galaxy stellar mass and morphological type (see Figure 22), it is important to keep dependencies of both factors with the environment under control in order to proceed in this analysis. In Paper III we discuss the variation of the stellar mass of each broad morphological type with our environmental indicators and show that in our sample galaxy, mass is largely independent of environment at a fixed morphological type.

Here we note that for the broad disk-dominated galaxies bin, biases in the median mass with any of the environments are not an issue, as for this class we can afford a fine galaxy mass bin splitting, and compare the C-mass relation for different environments within relatively small galaxy mass bins. For the broad bulge-dominated galaxies bin, however, given the fairly broad ranges covered by each of the two galaxy stellar mass bins, a difference in the median galaxy stellar mass (and, more generally, of the galaxy stellar mass distributions) between some of the different environments could, in principle, be present. This could induce a spurious dependence on such environments of the C versus stellar mass relations plotted in Figure 23. To keep this potential bias under control, we computed the median galaxy stellar masses within each environmental bin and found that for all three environments under study, the median stellar mass of galaxies in the broad bulge-dominated galaxies morphological bin changes by less than 0.1 dex between the environmental bins

under comparison (i.e., low/high M_{GROUP}, δ_{LSS}, and inner/outer group regions).

We also verified whether the morphological mix changes substantially with environment. The fractional contribution of intermediate-type disk galaxies to the total intermediate-plus late-type disk populations that compose the broad disk-dominated galaxies' morphological bin defined above varies at most by 5% between the low/high M_{GROUP} samples. To be precise, in the three bins of galaxy stellar mass defined for the broad disk-dominated galaxies' morphological bin, this fractional contribution, i.e., $(N_{interm.}/(N_{interm.} + N_{late-type}))$, equals, respectively, 35%, 55%, and 85% for $M_{GROUP} < 10^{13.5} M_{\odot}$ and 36%, 56%, and 82% for $M_{GROUP} > 10^{13.5} M_{\odot}$. The fractional contribution of S0s to the broad bulge-dominated galaxies' morphological bin is also almost identical between the samples of $M_{GROUP} < 10^{13.5} M_{\odot}$ and $M_{GROUP} > 10^{13.5} M_{\odot}$, and equal to $\sim$15% at $M_{galaxy} \sim 10^{10} M_{\odot}$ and $\sim$30% at $M_{galaxy} > 10^{10.5} M_{\odot}$. Likewise, at $M \gtrsim 10^{10} M_{\odot}$, the maximal variation in the fraction of intermediate galaxies within the disk-dominated galaxies class is 5% across the two δ_{LSS} bins. On the other hand, variations of $\sim$20% are detected in the contributions of S0s to the broad bulge-dominated morphological bin between samples at small/large group-centric distances and low/high LSS (over)densities at $M \sim 10^{11} M_{\odot}$; hence we use caution in interpreting, for this broad morphological type, possible differences in the C versus galaxy stellar mass relation at these mass scales.

The first thing to realize from Figure 23 is that there are, at most, weak trends with the different environments of the concentration versus stellar mass relation for disk satellite galaxies. Two environmental trends are however potentially important.

1. There is a global trend at and above galaxy masses of the order of $10^{10} M_{\odot}$ for satellites with a bulge-dominated morphology to be, albeit at the 1–2σ-level, systematically more concentrated, by about 5%–10%, at low environmental densities (large group-centric distances and low LSS densities) than at high environmental densities (small group-centric distances and high LSS densities). This difference could be at least partially driven by a change in the mix between S0 and bulge-dominated spirals within the broad bulge-dominated morphological bin.

2. In contrast, the disk-dominated population shows a systematic increase in median concentration at fixed galaxy stellar mass above $10^{10} M_{\odot}$, with increasing group mass and LSS density. In this case the similar contributions of intermediate-type disks and late-type disks to the broad disk-dominated morphological bin suggest that there is a genuine environmental effect at work. The difference in concentration between low and high mass groups is $\Delta C \simeq 0.3$; furthermore, the effect is robust toward the inclusion/exclusion of the sample of unrelaxed groups. The significance of this concentration difference, as assessed through a t-test on the two samples, gives a probability of >91% that the two populations have truly different median concentrations (or a Kolmogorov–Smirnov test gives a 95% probability of a common parent distribution). On the other hand, the trend with δ_{LSS} becomes weaker when only groups with $M_{GROUP} < 10^{13.5} M_{\odot}$ are considered for the LSS analysis. As discussed in Paper I, the effect observed with δ_{LSS} when the most massive groups are included is likely a spurious reflection of the dependence of concentration on halo mass.

As indicated above, a full investigation of the implications of either of these trends is beyond the scope of this paper. We will study these effects in more detail, also within the framework set by other independent analyses of the satellite population, in a future ZENS analysis.

9. SUMMARY AND CONCLUDING REMARKS

We have presented detailed structural analyses performed on the 1455 galaxies in the 141 ZENS groups introduced in Paper I. We remark that the corresponding ZENS catalog has, however, 1484 galaxy with valid entries, since we measure parameters for individual galaxies that are members of 26 galaxy pairs given as one single entry in the parent 2dFGRS galaxy catalog.

The parametric and non-parametric structural measurements presented here, together with the detailed environmental parameters from Paper I and the photometric (including stellar masses) measurements presented in Paper III, set the basis for a number of forthcoming publications that use the ZENS data to explore which environmental scales are relevant for the evolution of morphologically different galaxy populations at different mass scales. The measurements are published in the global ZENS catalog with Paper I. In detail, the measurements that we have presented here are:

1. strength of bars in disks quantified through an isophotal analysis (Section 3);
2. single- and double-component (bulge+disk) Sérsic fit parameters both in the B and I bands, including model-based galaxy sizes (Sections 4.1 and 4.2), as well as bulge+disk+bar fits for disks with a noticeable bar component (Appendix B.3);
3. non-parametric structural indices of concentration, asymmetry, smoothness of the light distribution, Gini and M_{20} coefficients, and "aperture photometric" size estimates (Section 5); and
4. morphological classes based on a quantitative bulge+disk criterion, augmented (or supported) by quantitative criteria regarding the non-parametric diagnostics after correction for observational biases (Sections 4.2 and 7).

Crucially, we do indeed derive correction matrices, which we apply to the relevant structural estimates, to minimize biases which, depending on PSF size as well as galaxy magnitude, size, shape of light profile, and ellipticity, would otherwise prevent a reliable comparison of the structural properties of galaxies observed in different seeing conditions and lying in different regions of this four-dimensional galaxy parameter space (see Section 6).

As expected, biases in the model-fit parameters are substantially reduced thanks to the treatment of the PSF-blurring effects in these algorithms. Still, some are present even in the model-fit parameters, which may have an impact on some analyses if left uncorrected. Disk properties are well measured and require very modest or no further corrections, as are bulge-to-total ratios, which therefore offer an excellent parameter on which to base a quantitative morphological/structural classification. In contrast, bulge n Sérsic indices and half-light radii are degenerate in some circumstances. This implies that, on global galactic scales, concentration parameter, or n-Sérsic index alone are not a good proxy for bulge-to-disk ratio and thus morphology. Bulges can give large contributions to the total light budget and have large half-light radii, leading to low galaxy concentrations, or, vice-versa, bulges can be very compact and lead to high galaxy concentrations despite a modest contribution to the total light.
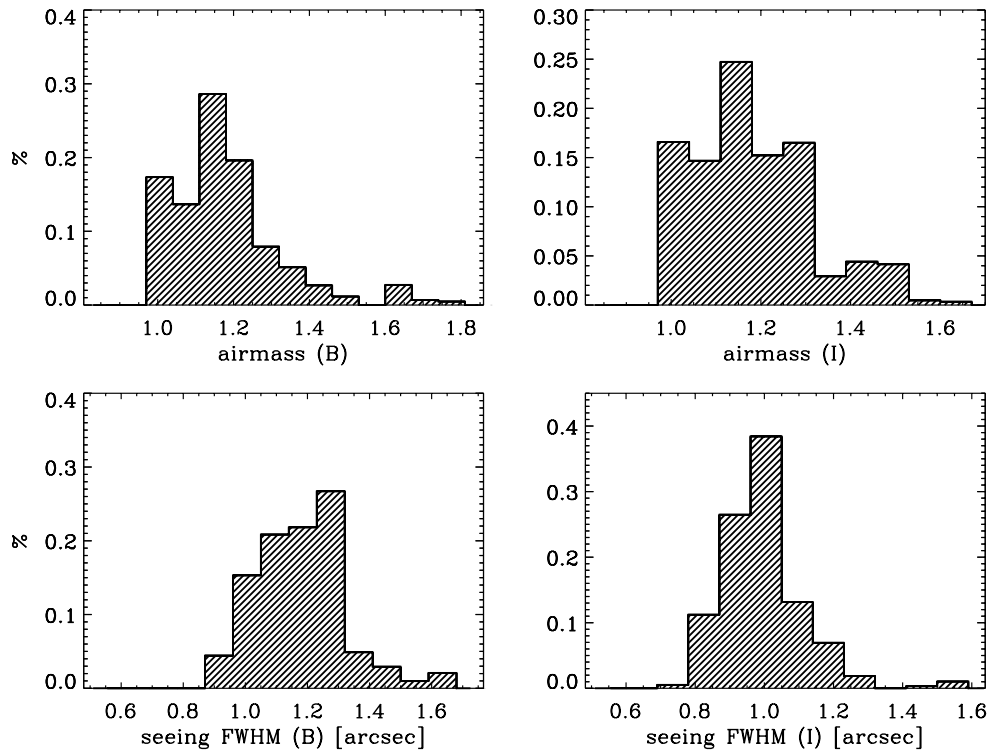
Figure 24. Summary of the observing conditions for the ZENS WFI data. Shown are the distribution of airmass and (instrumental plus atmospheric, i.e., total PSF) seeing values over the targeted fields for the *B* (left panels) and *I* bands (right panels), respectively.

Finally, we particularly warn against using uncorrected non-parametric estimators as galaxy classifiers since, understandably, they suffer from severe observational biases and introduce severe errors in the classifications (see Section 6).

As a first application of our corrected structural measurements, we have studied the variation of concentration in *satellite* galaxies of fixed stellar mass (from Paper III) with morphological type and with the three environments detailed in Paper I, i.e., the mass of the host group halo, the projected group-centric distance, and the density of the LSS cosmic web (Section 8).

We find that the known correlation of satellite concentration with galaxy stellar mass (e.g., Kauffmann et al. 2003) holds at a fixed morphological type. Specifically, there is a genuine increase in concentration with increasing stellar mass for disk satellite galaxies within each separate bin of bulge-dominated galaxies, intermediate-type, and late-type disk morphologies. The slope of the concentration versus galaxy stellar mass relationship flattens from the later to the earlier types (and becomes ∼0 for satellites with an elliptical morphology, which cover a limited range in galaxy stellar mass in our sample). It is not trivial to disentangle, in a physically meaningful way, the contributions of an increasing bulge-to-total ratio with increasing mass and an increasing bulge concentration at fixed bulge-to-total ratio with increasing mass, to the increase in concentration of satellite disk galaxies with increasing stellar mass. This is true even in our study, in which we did indeed base our morphological classification on the bulge-to-total ratio, and thus bulge-to-total variations within each Hubble type should be minimized. There are nevertheless some residual effects, as the median B/T is found to vary in our sample from ∼7% at $10^{10} M_\odot$ to ∼12% at $\sim 10^{10.5} M_\odot$ for late-type disks, and from 59% to 64% between $10^{10} M_\odot$ and $10^{11} M_\odot$ for bulge-dominated disks. Still, for intermediate-type disk satellites in which the bulge-to-total ratio is tightly constrained by firm

lower an upper boundaries by definition, the increase in satellite density with stellar mass can be genuinely ascribed to a ∼30% decrease in the bulge-to-disk size ratio, i.e., to a genuine increase in the concentration of the bulge component at fixed bulge-to-total light ratio. We tentatively assume this as the explanation for the increase of disk satellite concentration with stellar mass at fixed Hubble type, an hypothesis that we will test with further analyses.

When considering the galaxies' environment, we find that, at galaxy stellar mass $\sim 10^{10} M_\odot$ and above, (1) bulge-dominated satellites tend to be marginally more concentrated at low LSS densities and high group-centric distances; and (2) in contrast, disk-dominated satellites are significantly more concentrated in high group masses.

The interpretation of the first weak trend as a hint for an environmental effect is further hampered, at $M \sim 10^{11} M_\odot$, by a higher fraction of S0s relative to bulge-dominated spiral galaxies in low $\delta_{\rm LSS}$ relative to high densities (60% and 0%, respectively in $M_{\rm GROUP} < 10^{13.5} M_\odot$ groups and 58% and 35% over all groups) and in the outskirts relative to the cores of groups (50% and 31% over all groups). This change in morphological mix at the high end of the B/T sequence is consistent with other observational works, which have also reported an increase in the S0 fraction in the outskirts of groups and clusters, although with no distinction between central and satellite galaxies.

The early study of Whitmore et al. (1993) on local cluster reveals a drop in the S0 fraction close to the cluster centers, which they interpret as the outcome of disk galaxies' destruction happening at the cluster cores. The more recent analysis of the morphology–density relation at redshift $0.05 < z < 0.1$ by Goto et al. (2003) shows a depletion of S0 galaxies within 0.3 virial radii and an increase in the early spirals population at the same distances, consistent with the variation we see in our ZENS sample. Also in $z \sim 0.4$ groups Wilman et al. (2009) find
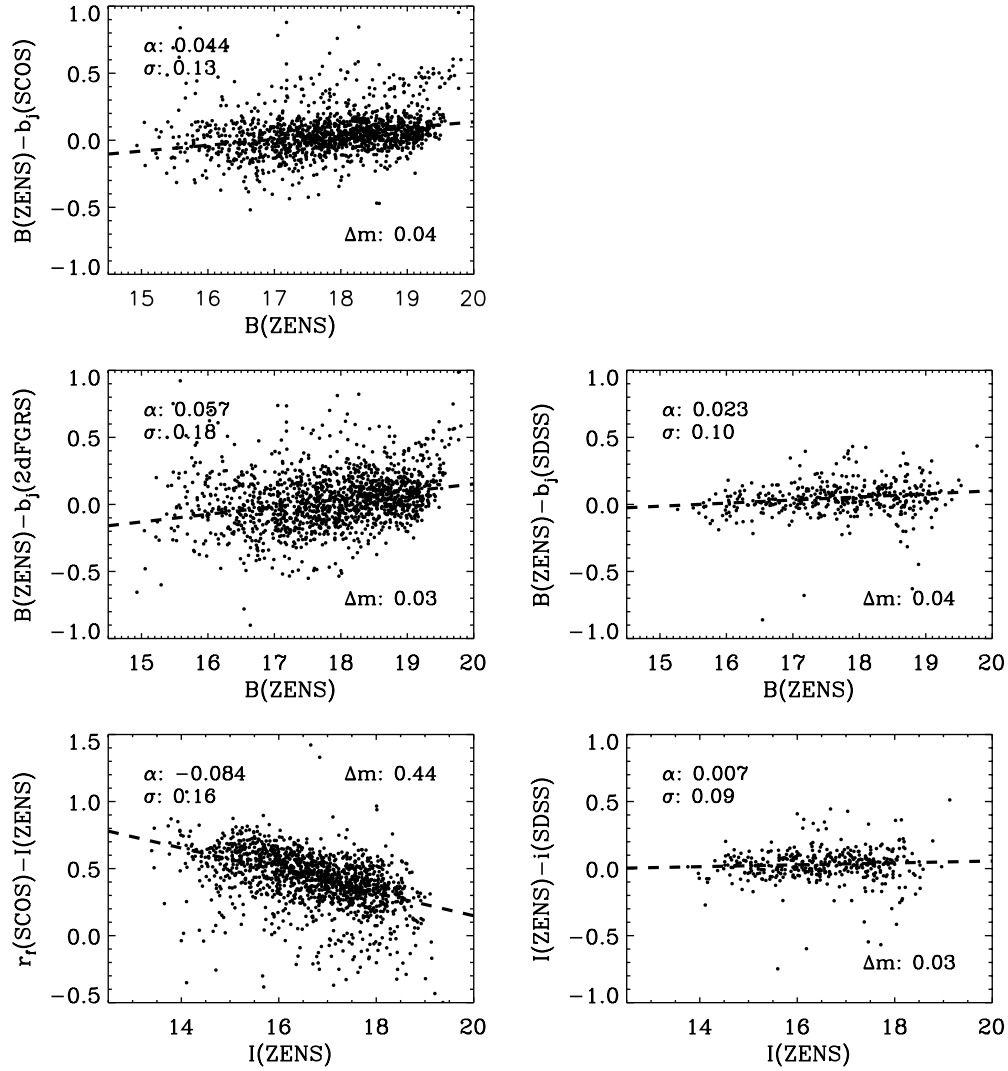
Figure 25. Accuracy of the ZENS WFI photometric calibration. Each panel shows the difference between the ZENS apparent magnitude in either the *B* or *I* band and relevant magnitudes available from the literature: SuperCosmos Survey b_j, 2dFGRS b_j, SDSS-based b_j, SDSS *i*, SuperCosmos Survey r_F. The quantities α and σ are the slope of the best linear robust fit to the data and the dispersion around this relation, respectively. Δm is the median difference between each couple of measurements. All magnitudes are corrected for galactic extinction.
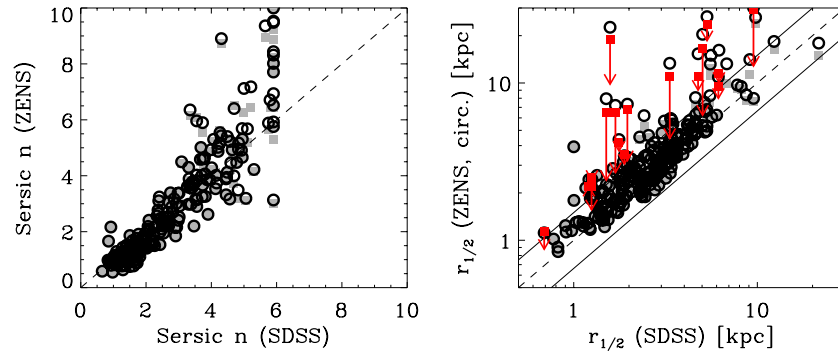
Figure 26. Comparison of Sérsic indices (left) and half-light radii (right) between our single-component *I*-band Sérsic fits and corresponding *i*-band single-component Sérsic parameters from the SDSS NYU-VAGC. To match the previous measurements, which use circular aperture, we plot here post-processing circularized (i.e., $\sqrt{ab}$) half-light radii also for ZENS. Empty circles present the comparison using the corrected ZENS structural parameters (see Section 6.3) while the light gray or dark grey (red in the online version) squares are the original GIM2D measurements prior to such corrections. The dashed line in the right plot is the identity relation; the solid lines indicate a variation of a factor of 1.5. Dark gray squares (red in the online version) highlight galaxies with ZENS Sérsic indices $n > 6$, i.e., the maximum allowed values in the Blanton et al. (2005) SDSS fits. The arrows connect the original (uncorrected) ZENS measurement, performed allowing n to vary freely up to a value of 10, and the half-light radius that is measured imposing $n < 6$, as done in the SDSS fits.

(A color version of this figure is available in the online journal.)
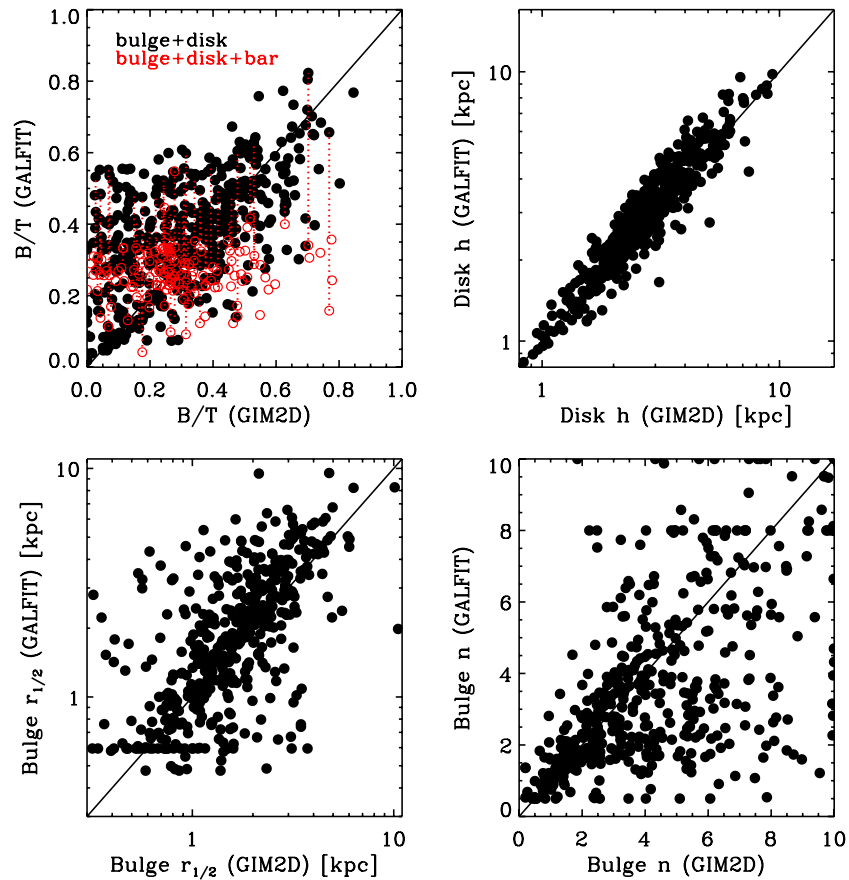
Figure 27. Comparison between the bulge and disk structural parameters obtained with `GALFIT` and `GIM2D`. From top to bottom and from left to right: bulge-to-total ratio, disk scale length, bulge effective radius, and bulge Sérsic index. Shown are only galaxies for which both the `GIM2D` and `GALFIT` models were judged to give reliable fits according to the criteria that we describe in Appendix B.2. The empty gray symbols (red in the online version) in the top left panel show the comparison between the B/T obtained with the simple `GIM2D` bulge+disk decomposition (x-axis) and the `GALFIT` bulge+disk+bar fits (y-axis). The vertical gray (red in the online version) lines connect the B/T obtained by `GALFIT` with the bulge+disk+bar fits or the bulge+disk only fits.

(A color version of this figure is available in the online journal.)

hints for an excess of S0 galaxies at $r \gtrsim 0.3$ Mpc with respect to the group centers, which instead host a higher fraction of late-type disks. These authors furthermore find that the fraction of S0 galaxies in groups is comparable to the one in clusters at the same redshift, suggesting that galaxy pre-processing and S0 formation is effective already at these low densities. The increase of S0 in the outer regions of the groups is particularly interesting, as it is counter to the intuitive idea that gas-rich bulge-dominated spirals may become S0 galaxies as they fall deeper into their group potential wells (see, e.g., Bekki et al. 2002, who find that gas stripping in the group environment is only effective close to the group centers).

Speculating on the above, a possible scenario is that (1) bulge-dominated galaxies are transformed into S0s as soon as disk galaxies enter the group potential, and (2) further stellar evolution within the groups replenished the dried-out disks of S0 galaxies with fresh gas, establishing/restoring in them a bulge-dominated morphology. Note that an increase in the fraction of dusty star-forming galaxies at high densities and close to cluster centers has been observed at low redshift, e.g., Gallazzi et al. (2009) and Mahajan & Raychaudhury (2009). Furthermore, the evidence of polar and extended H I disks around S0s—e.g., van Gorkom et al. (1987), Noordermeer et al. (2005), and Sage & Welch (2006)—may also support this "disk-regrowth" scenario.

The second, statistically more significant trend for $M > 10^{10} M_\odot$ disk-dominated galaxies to have a higher concentration in high-mass ($M > 10^{13.5} M_\odot$) than in lower-mass groups appears to be a genuine environmental effect that should suffer from no morphological complications.

Weinmann et al. (2009) and Guo et al. (2009) found evidence in their SDSS samples that, among galaxies with $C < 3$, satellites are more concentrated than centrals with identical stellar mass. These authors interpret the variation in concentration within the framework of gradual stripping and subsequent quenching of satellite galaxies during infall into the group potential. This is also believed to cause a reddening of the satellite galaxies and a shrinking of their typical sizes. While we postpone an analysis on the subject to a forthcoming paper, here we wish to note that the SDSS studies divide the early- and late-type morphological classes on the basis of a non-corrected concentration criterion ($C < 3$ for late-type and $C > 3$ for early-type galaxies). Comparing their Figure 1 with our Figure 20, we see that $C < 3$ in the SDSS system roughly corresponds to a value of $C = 3.5$–4 in ZENS, as our concentrations show a small offset due to the corrections we applied. As illustrated in Figure 22, a cut at constant concentration subdivides the ZENS galaxy sample into two broad bins in which individual Hubble types are mixed together below the chosen C threshold.
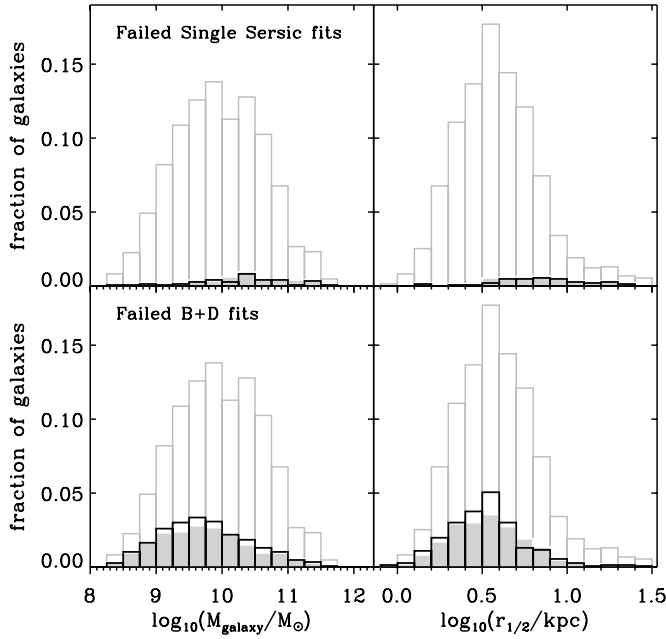
Figure 28. Distribution of galaxy masses and *I*-band corrected sizes (see Section 6) for the total sample of galaxies (empty, light gray histograms) and for galaxies with no reliable GIM2D Sérsic fit (top) or bulge+disk decompositions (bottom). The black histogram is for galaxies with no fit in the *I* band and the filled dark-gray histogram for failed fits in the *B* band. All histograms are normalized to the total number of galaxies in our sample. For galaxies that do not have half-light radii derived from the single Sérsic fits, we use the corrected ZEST+ radii in this figure.

It thus remains an open question whether the difference in concentration between centrals and satellites reported by those authors is the result of a variation in the morphological mix of the central versus satellite populations, or rather a change in the structure of central and satellite galaxies at a fixed morphological type. We will address this question in a later dedicated ZENS analysis.

APPENDIX A

PROPERTIES, REDUCTION, AND PHOTOMETRIC CALIBRATION OF THE WFI *B* AND *I* DATA

Table 3 gives a log of the observing runs for the new ESO/2.2 m *B* and *I* band WFI images. These images were taken with the 4×2 mosaic of $2k \times 4k$ coated CCDs, which provides a scale of $0.''238$ pixel^{-1} and covers a total field of view of $34' \times 33'$, well suited to the typical sizes of the ZENS groups. Each group
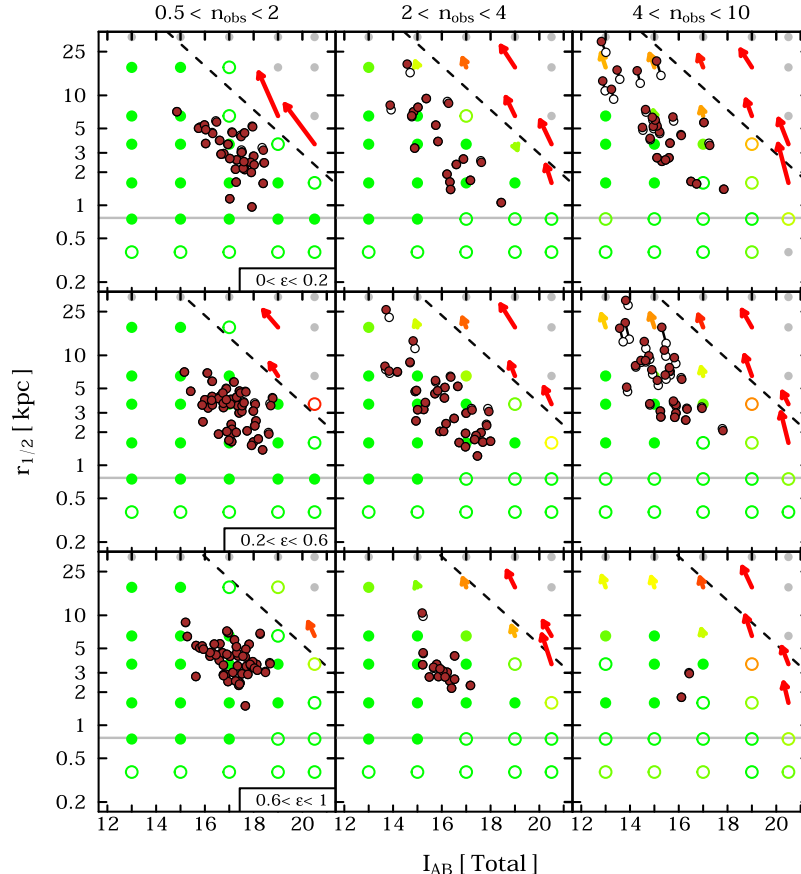
Figure 29. As in Figure 8 but for galaxy models convolved with the best PSF ($0.''7$) measured in the *I* band WFI ZENS images.

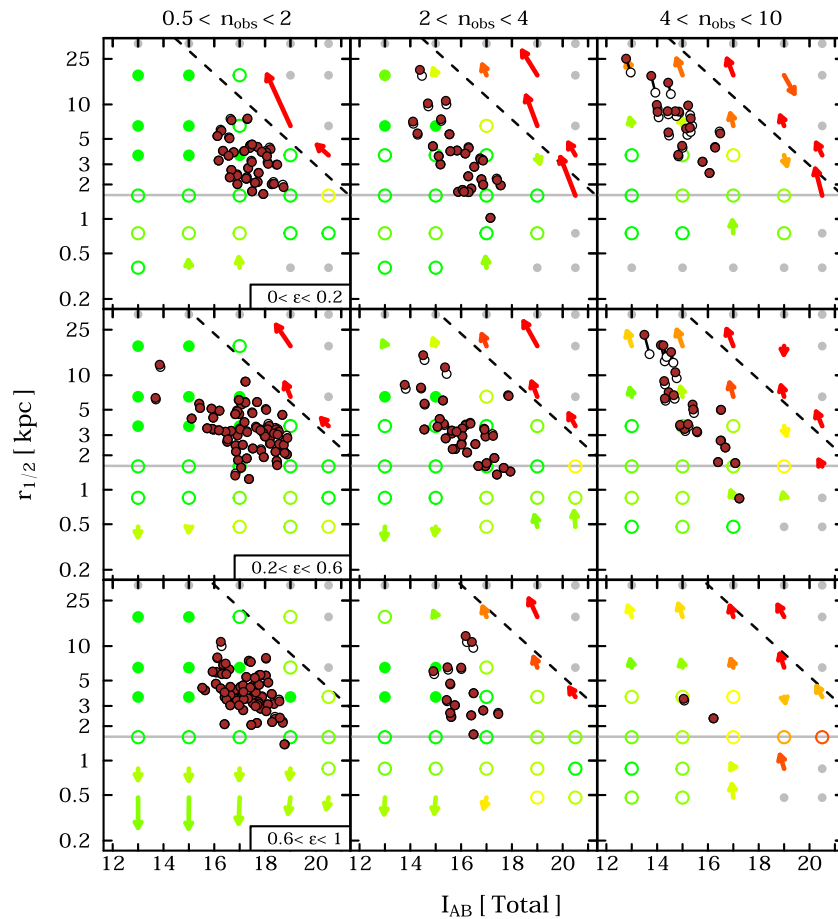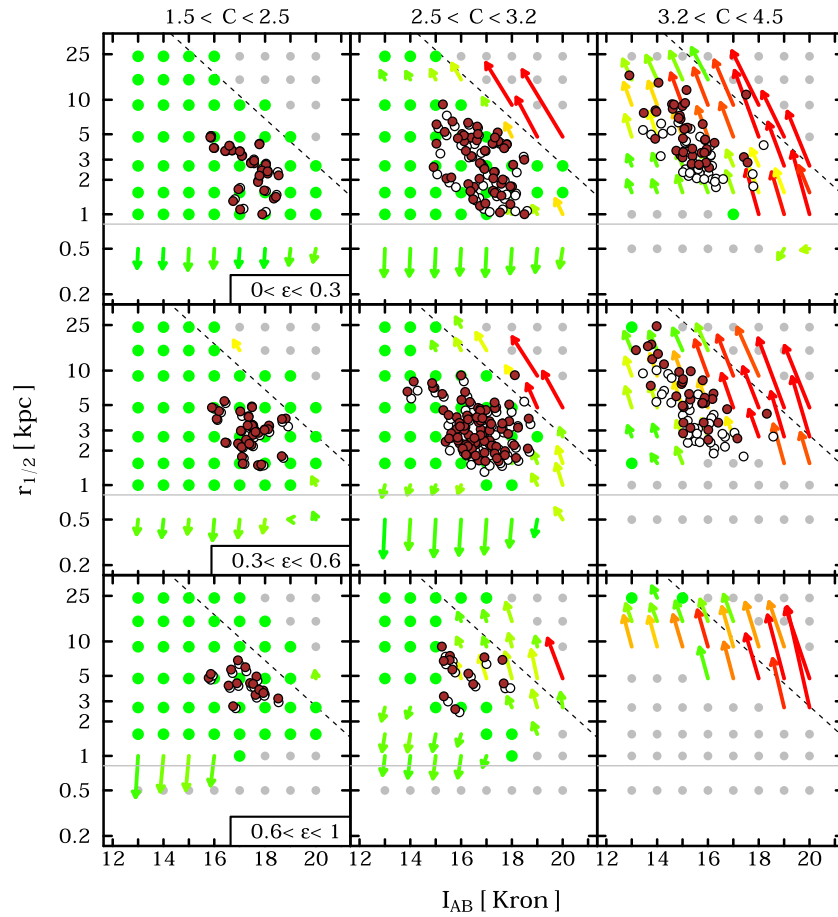(A color version of this figure is available in the online journal.)

Figure 30. As in Figure 8 but for galaxy models convolved with the worst PSF (1″5) measured in the *I* band WFI ZENS images.
(A color version of this figure is available in the online journal.)

Table 3
Log of Observing Runs

Run	Date	Exposure Time (s)	Number of Groups	Program ID	Mode
1	2005 Jan 5–Feb 18	131.917	20	074.B-0570	Service
2	2006 May 1–Dec 23	143.917	50	177.A-0680(A/B)	Service
3	2007 Feb 18–Jul 14	143.917	21	177.A-0680(A/B)	Service
4	2008 Jan 14–Jul 31	143.917	12	177.A-0680(A/B)	Service
5	2008 Oct 30–Nov 5	143.917	25	177.A-0680(C)	Visitor
6	2009 Mar 25–28	143.917	13	177.A-0680(D)	Visitor

Notes. For each set of observations we list the exposure times, the number of observed groups, and the program ID and mode. Sequential numbers in the first columns indicate the run ID.

was observed with five dithered exposures to remove inter-chip gap effects and cosmic rays events; the single exposure times were 132 s for the 2005 runs and 144 s for all other runs. All observations were carried out under clear night conditions. The final seeing after image stacking is typically $\sim 1''$, reaching down for the best runs to $0''7$ and $0''9$ in the *I* and *B* bands, respectively, and, in a few worst cases, degrading to $1''5$ and $1''6$. Figure 24 gives a summary of the airmass and seeing conditions of the WFI observations.

The ZENS detection limits are given by the 1σ background fluctuations in a uniform area of 1 arcsec^2 (18 pixels) and correspond to $\mu(B) = 27.2$ mag arcsec^2 and $\mu(I) = 25.5$ mag arcsec^2 (AB magnitudes). The depth of the WFI *B* and *I* data allow us to robustly quantify the structure of the ZENS galaxies out to at least 2 half-light radii, and to

detect low surface brightness tidal tails and merger-induced features. At the given depth limits and with a total sky coverage of 45 deg^2, ZENS is a relatively deep survey on a relatively large area and thus a valuable data set also for legacy science.

A.1. Data Reduction

The WFI *B* and *I* images were reduced using standard IRAF[9] routines and, in particular, the NOAO mosaic software *MSCRED* was used for most of the processing.

Figure 31. As in Figure 9 but for galaxy models convolved with the best PSF (0.″7) measured in the I band WFI ZENS images.
(A color version of this figure is available in the online journal.)

The bias subtraction involved two steps: each frame was initially subtracted of a bias level using, for each pixel row, the median value of the overscan pixels in the same row. Remaining large-scale features in the bias were further eliminated by subtracting a combined bias image, which was obtained separately for each night by stacking together at least 10 (overscan subtracted) bias frames. Dark current was not subtracted since its value is negligible ($(0.3$–$0.6) \times 10^{-3}$ ADU s^{-1} pixel^{-1}). The images were corrected for pixel-to-pixel variation of the quantum efficiency by dividing them with a twilight flat field, obtained by combining several tens of flat-field exposures acquired throughout the different nights of each observing run. The presence of residual large-scale illumination inhomogeneities was removed with a super flat field obtained from the science exposures themselves stacked together with a 3σ-clipping algorithm to remove all bright sources.

The I-band images were affected by fringing and required intermediate processing before deriving the super-flat images. All the bias-corrected and flat-fielded I frames were combined to obtain an image of the fringing pattern. The large-scale features of the fringing image were removed by subtracting a smoothed version of itself; this produced the final fringe template containing only the signal arising from the fringing itself. The fringing template was then subtracted from the science exposures with an interactive task, allowing us to verify the quality of the correction. These fringing-removed images were finally used to create the super flat field for the red filter.

Further reduction steps were made to correct for detector cosmetic effects, such as bad pixels or hot or dead columns. The five individual reduced images of each group in each filter were stacked together to obtain the final science images that we used in our analysis. From the large group frames we extracted postage stamp images for each of the galaxies of size equal to three Petrosian radii. Sky subtraction was performed locally on the cleaned stamps so as to account for small inhomogeneities in the sky level. Cleaning of the postage stamps involved removing most of the light coming from other galaxies (or from spurious stellar spikes and other contaminations) and substituting an iterated value of the average sky level in the stamp to the relevant pixels. Companion galaxies were identified using SEXTRACTOR as sources above 1.5σ of the sky level and the pixels belonging to these objects were replaced with random blank sky regions. All stamps were furthermore visually inspected to verify the quality of the cleaning process.

A.2. Photometric Calibration

Photometric calibration was performed using Landolt (Landolt 1992) standard stars. Several Landolt fields, with at least 5 standard stars, were observed for each night. Aperture magnitudes for these stars were measured with the IRAF task qphot and used to derive the photometric zero point (ZP) for the two pass bands.
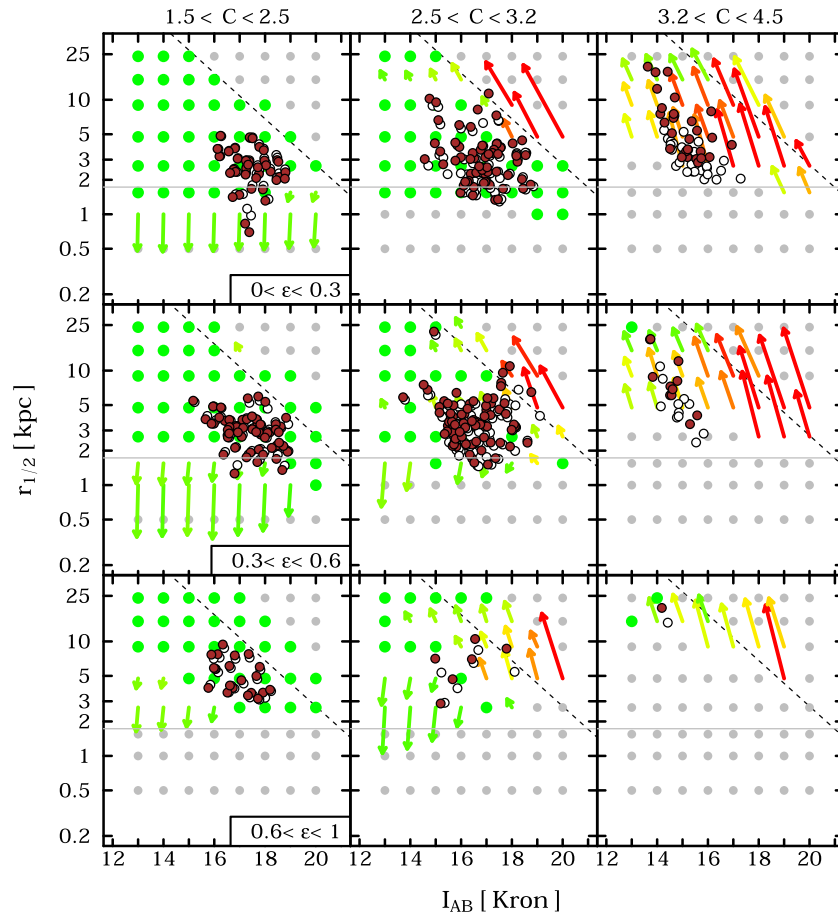
Figure 32. As in Figure 9 but for galaxy models convolved with the worst PSF (1″5) measured in the *I* band WFI ZENS images.
(A color version of this figure is available in the online journal.)

Table 4
Zero Points, Color Terms, and Extinction Coefficients
for the WFI *B* and *I* Filters

Run	Date	ZP_B(AB)	ZP_I(AB)	α_B	α_I	k_B	k_I
1	2005 Jan 5–Feb 18	24.75	23.74	0.215	0	0.22	0
2	2006 May 1–Dec 23	24.75–25.08	23.74–24.0	0.215	0	0.22	0
3	2007 Feb 18–Jul 14	24.85–24.96	23.81–23.90	0.215	0	0.22	0
4	2008 Jan 14–Jul 31	24.53 -24.99	23.74–23.92	0.215	0	0.22	0
5	2008 Oct 30–Nov 5	24.93–24.99	23.89–23.92	0.215	0	0.22	0
6	2009 Mar 25–28	25.00–24.94	23.88–23.98	0.215	0	0.22	0

Notes. The zero points (in the AB system and for magnitudes in ADUs, a term +0.75 must be added to convert to electrons) and other parameters for the photometric calibrations of the observing runs of Table 3. For each run we list the range of measured ZPs. The coefficients α are the color terms in the calibration equations. The airmass extinction coefficients K_B and K_I could not be derived from our own data as the acquired standard stars did not sample a sufficient range of zenith distances. For these quantities we used the latest measurements available on the WFI calibration web page.

We used the following calibration equations between the Landolt *B* and *I* and the WFI instrumental magnitudes b, i: $B = ZP_B + b + \alpha_B(B - V) - k_B X$ and $I = ZP_I + i + \alpha_I(V - I) - k_I X$, respectively. In these calibration equations X is the airmass value at the time of observation and k is the extinction coefficient. ZPs, color terms, and extinction coefficients are presented in Table 4. Since our standard stars were not observed at sufficiently differing airmasses to allow for a sensible extinction correction, magnitudes were airmass-corrected by using the extinction

Table 5
Fraction of Reliable Single Sérsic Fits and Bulge+Disk
Decompositions for Galaxies of Different Morphological Types

Type	Reliable Single Sérsic Fits	Reliable Bulge+Disk Fits
B-Band	Total (96%)	Total (81%)
Elliptical	98%	. . .
S0	95%	81%
Bulge-dom. spiral	97%	76%[a]
Intermediate spiral	94%	92%
Late spiral	96%	74%[b]
I-Band	Total (96%)	Total (77%)
Elliptical	100%	. . .
S0	95%	74%
Bulge-dom. spiral	97%	69%[a]
Intermediate spiral	94%	90%
Late spiral	97%	70%[b]

Notes. The fraction of reliable single-Sérsic and bulge+disk decompositions (the latter obtained either with GIM2D or with GALFIT) for each morphological type, separately for the *B* and *I* bands. Ellipticals are by definition galaxies very well fit by a single-Sérsic component only, whose *n* index is >3.
[a] If excluding the merging galaxies for which the decomposition is made difficult by the strong contamination from the companion and the generally disturbed morphology, the fractions increase to 86% and 81% for the *B* and *I* bands respectively.
[b] In the fraction of failed bulge+disk decompositions we include those galaxies in which the formal Sérsic-bulge profiles dominates at all radii with an *n* < 1.5. However, these failed disk+bulge decompositions identify good disk-dominated cases; these are 6% and 10% of the late-type disks in the *B* and *I* bands, respectively.
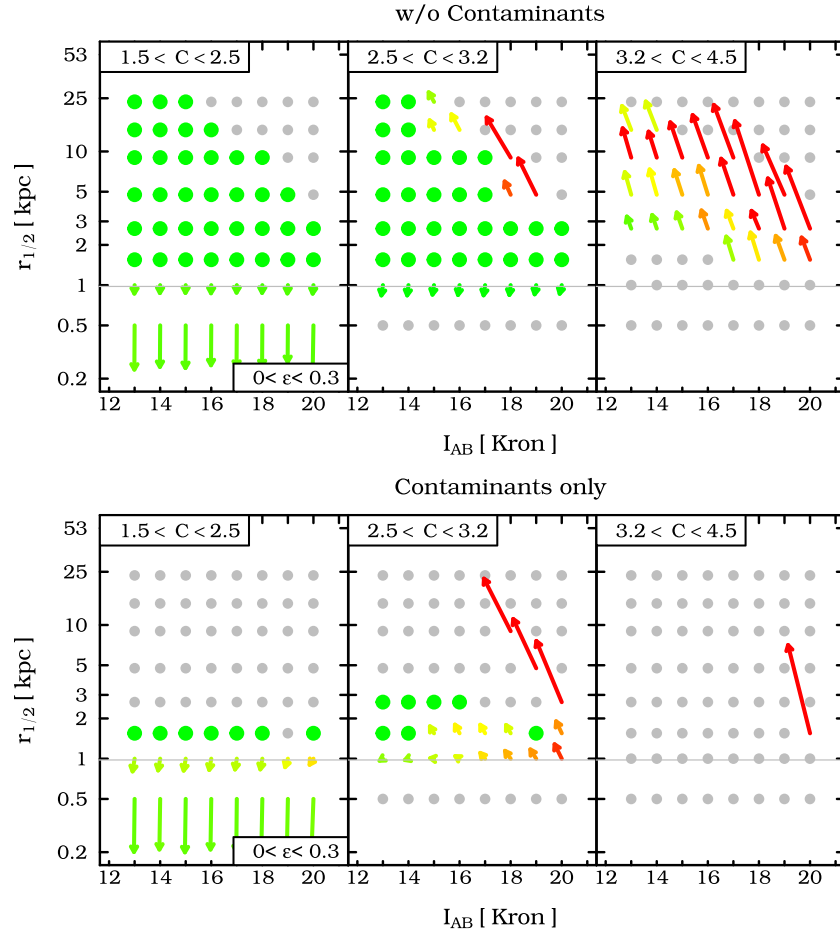
Figure 33. Comparison between the size–magnitude correction grid obtained from galaxies whose intrinsic parameters lie within the same $\epsilon - C$ bin (upper panels, "without contaminants"), and from galaxies with ϵ and/or C values outside of the measured bin, which are scattered into the latter by measurements errors (lower panels; "contaminants only"). The comparison is shown for the lowest ellipticity bin, which suffers from the highest contamination of scattered galaxies into low concentration bins, and for the median PSF FWHM in the WFI ZENS data; similar results hold for all PSF sizes. Corrections for sizes and magnitudes obtained from "indigenous" and "scattered" models are well in agreement with each other, indicating that our correction maps do not depend significantly on the precise way we populate our simulation grid.

(A color version of this figure is available in the online journal.)

coefficients given on the WFI website[10] as a reference. All magnitudes are calibrated onto an extra-atmospherical airmass of zero.

Although there is no clear color dependence of the calibration for the *I* filter ($\alpha_I = 0$), it is necessary to correct for a color term ($\alpha_B = 0.215$) in the case of the *B* band. We also found that the ZP points themselves show a shift over the different observing runs, even though the slope of the calibration remains constant (most likely be due to different CCD/ambient conditions during the observations). For this reason, we calibrated each night separately, fixing the slope of the color contribution to the well-established common value for all the nights while using the night-by-night determined ZPs for each set of observations.

The Landolt system is tied to the standard Johnson-Cousin system that uses Vega for reference; we thus converted our magnitudes to the AB system (Oke 1974) through the following procedure. For the *B* band, we found the ZP corresponding to an object with zero color in AB in the $ZP - (B - V)$ relation and used this value as our final calibration factor for the blue filter. As mentioned before, the color term was negligible for the *I* band and thus it was not possible to apply such method. In this case the

following transformation was applied: $m_{AB} = m + m_{AB}(Vega)$. We computed the conversion factor using the SYNPHOT IRAF package (see also Fukugita et al. 1995) and found it to be $I_{AB}(Vega) = 0.45$. The values for the ZP we find are in good agreement with those reported on the WFI calibration web-page.

We assessed the robustness of our calibration by comparing the magnitudes obtained for the stars in the ZENS fields, as well as for the ZENS galaxies with the others available from the literature. For the ZENS galaxies we used the magnitudes obtained with the SExtractor (Bertin & Arnouts 1996) software and determined from the flux curve of growth inside a Kron-like elliptical aperture (MAG_AUTO in the code). The Kron (1980) aperture radius correspond to 2.5 times the radius of the first image moment. All magnitudes are corrected for galactic absorption using the dust maps of Schlegel et al. (1998) and the Cardelli et al. (1989) dust law. As reference values we consider the 2dFGRS b_j, the SuperCosmos Survey b_j and r_F (Hambly et al. 2001), and the SDSS *i* and b_j magnitudes (Abazajian et al. 2009). The latter is derived as in Norberg et al. (2002), using the relation $b_j = g + 0.155 + 0.152 \times (g - r)$.

We show in Figure 25 the comparison between the derived ZENS magnitudes and the published ones. We have a good

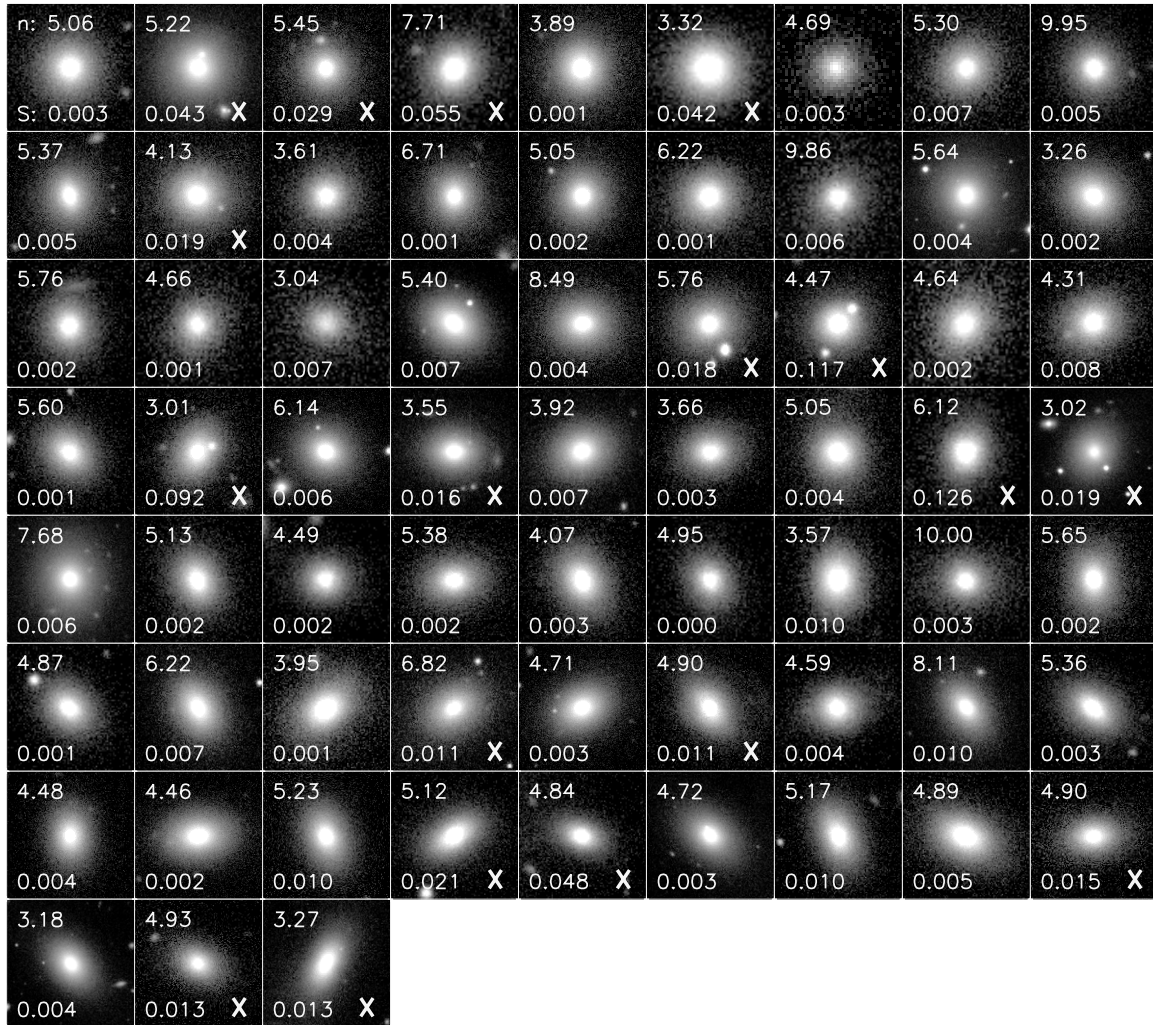**Figure 34.** *I*-band stamp images of ZENS galaxies classified as ellipticals. Galaxies are ordered from top-left to bottom-right by increasing ellipticity. The criteria defining galaxies falling into the elliptical class are given in Figure 18. Specifically, elliptical galaxies have surface brightness profiles perfectly fitted by a single-component Sérsic profile with $n > 3$, as shown in Figure 35, and *B*-band smoothness $S_{B\text{-band}} < 0.01$. The value of the corrected Sérsic index n (top left) and *B*-band smoothness (bottom left) is indicated in each stamp. There are some exceptions in which we maintain an elliptical classification despite the galaxy failing the $S_{B\text{-band}}$ criterion. These galaxies are marked with a white $\times$ on the image; in a large fraction of them, the increased smoothness is associated with a bright star cluster or small galaxy clearly visible in the stamps. For the other such galaxies, our visual inspection did not detect any clear substructure that would suggest a different classification. The surface brightness profiles obtained from the GIM2D fits of all the elliptical galaxies are shown in Figure 35, and show that these systems are genuine single-Sérsic ($n > 3$) galaxies. This condition, together with the absence of a faint disk in the residual images, was given priority in the classification relative to the smoothness criterion.

agreement with the SuperCosmos values (within a standard deviation of $\sigma = 0.1$ mag), which is better than with the 2dFGRS one ($\sigma = 0.16$ mag). This is very consistent with the quoted photometric errors of the 2dFGRS (b_j magnitudes, 0.15 mag) and SuperCosmos magnitudes (0.1 mag). We mention that our *B* measurements show a small non-linearity with respect to both the SuperCosmos data and 2dFGRS b_j magnitudes. This non-linearity is, however, absent when we compare with SDSS photometry, which is available for a subset of our galaxies. With the exception of the expected shift between the SuperCosmos r passband ($r_F(\text{SCOS})$) and the ZENS *I* passband, the median magnitude offsets in the relevant comparisons are small at the level of ~2%.

We remark that in deriving galaxy stellar masses and other photometry-inferred parameters in Paper III, the ZEBRA+ software (Feldmann et al. 2006; Oesch et al. 2010) was first run in "photometry-check mode," to detect residual offsets from the individual passbands; no offsets were found for the WFI *B* and *I* passbands.

APPENDIX B

QUALITY-CONTROL CHECKS FOR THE GIM2D MODEL FITS

B.1. Comparison with Previous Works

For a number of galaxies in our sample, the SDSS New York University Value-Added Galaxy Catalog (NYU-VAGC; Blanton et al. 2005) provides half-light radii and indices n from single-component Sérsic fits to the azimuthally averaged surface brightness profiles. We thus compare in Figure 26 our own best fit parameters for the single component fits, both *prior to and after* the application of our corrections described in Section 6.3 with these previously published data. To match the VAGC definition, we *circularize* in post-processing mode, using the galaxies' ellipticities, our fiducial major-axis size estimates based on elliptical apertures. As illustrated in the figure, the agreement between the two sets of measurement is generally good. Only about 5% of the galaxies show in ZENS
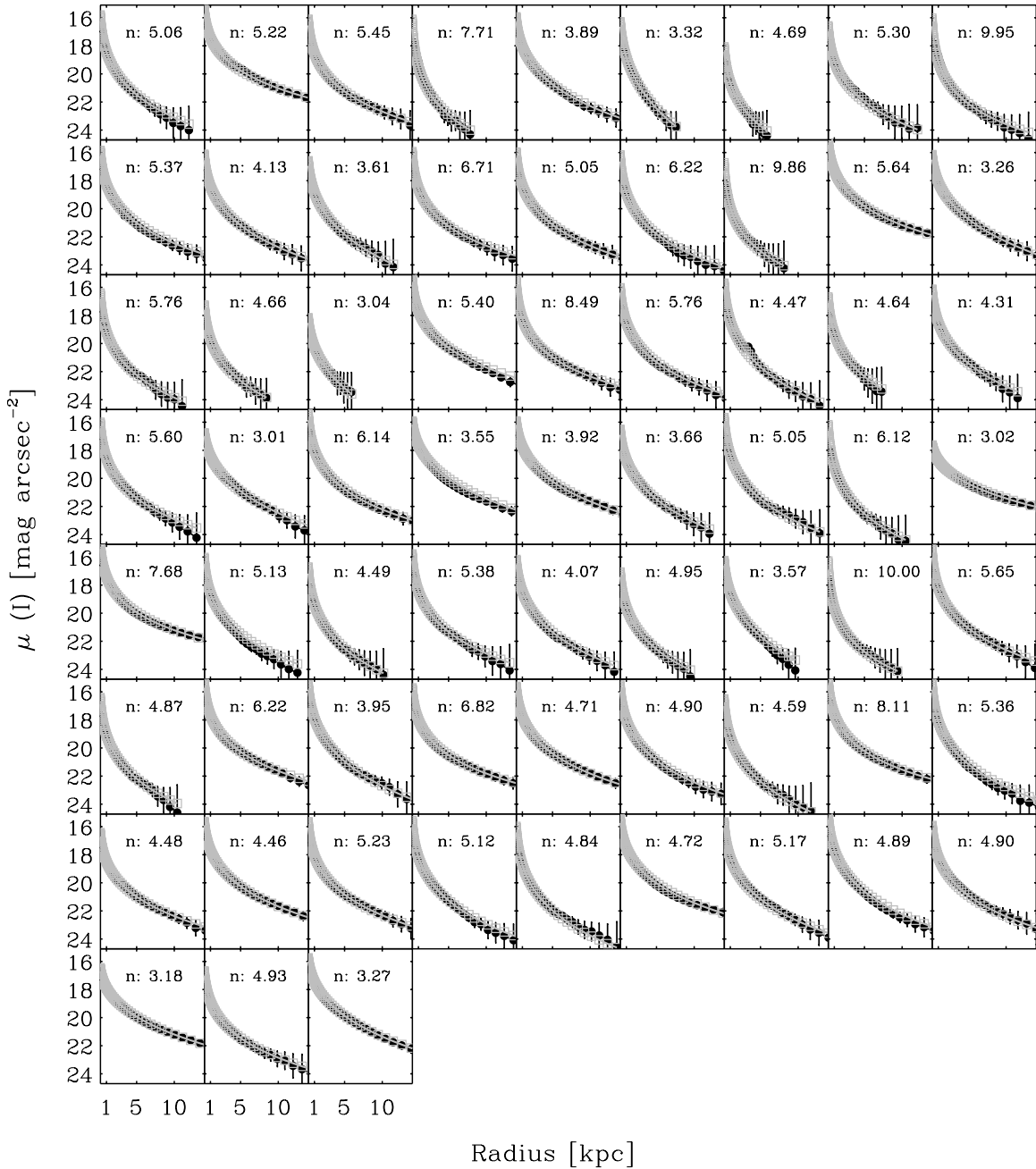
Figure 35. *I*-band surface brightness profiles and best fit single-Sérsic profiles for galaxies classified as ellipticals. The filled black points with error bars are the surface brightness profiles from the ELLIPSE isophote fits, while the gray empty squares show the single-Sérsic GIM2D models. Galaxies classified as ellipticals are required to be well fitted by a single Sérsic component with $n > 3$ from the inner galaxy regions out to the outermost measured points. Each panel shows the value of the Sersic index of these single-component fits.

larger half-light radii and Sérsic indices than those measured in SDSS. Regarding the differences in Sérsic index, we note that the SDSS fits have a maximum $n = 6$, whereas for the ZENS sample we allowed n to vary up to $n = 10$. Indeed, the most discrepant galaxies in the n-comparison plot are those that have reached the saturation value of $n \sim 6$ in the SDSS analysis (left panel in the figure). These same galaxies are actually that also many of those show a large difference in the half-light radius comparison plot (red-filled squares in the right panel of Figure 26). Part of the observed discrepancy in the radii is thus likely caused by the different n values in the ZENS and SDSS fits. To test this directly, we refitted these galaxies (including other galaxies that have $n > 6$ in ZENS but $n < 6$ in the SDSS

fits) by imposing a maximum $n = 6$ value for the Sérsic index in their single-component surface brightness fits, as done in the SDSS analysis. The red arrows in the right panel of the figure show the differences in $r_{1/2}$ that result from constraining the fits to a maximum $n = 6$ value. These differences highlight the interdependence of the derived parameters in such kind of fits and the systematic errors that such interdependence might introduce. Finally, we note that many of the ZENS galaxies whose nominal single-component size estimates are substantially larger than the SDSS size estimates are those galaxies that were already flagged in our ZENS catalog as having a problematic single-component size estimate in the analysis of Section 4.2.1 (filled red squares in the right panel of Figure 26). These galaxies were found to have
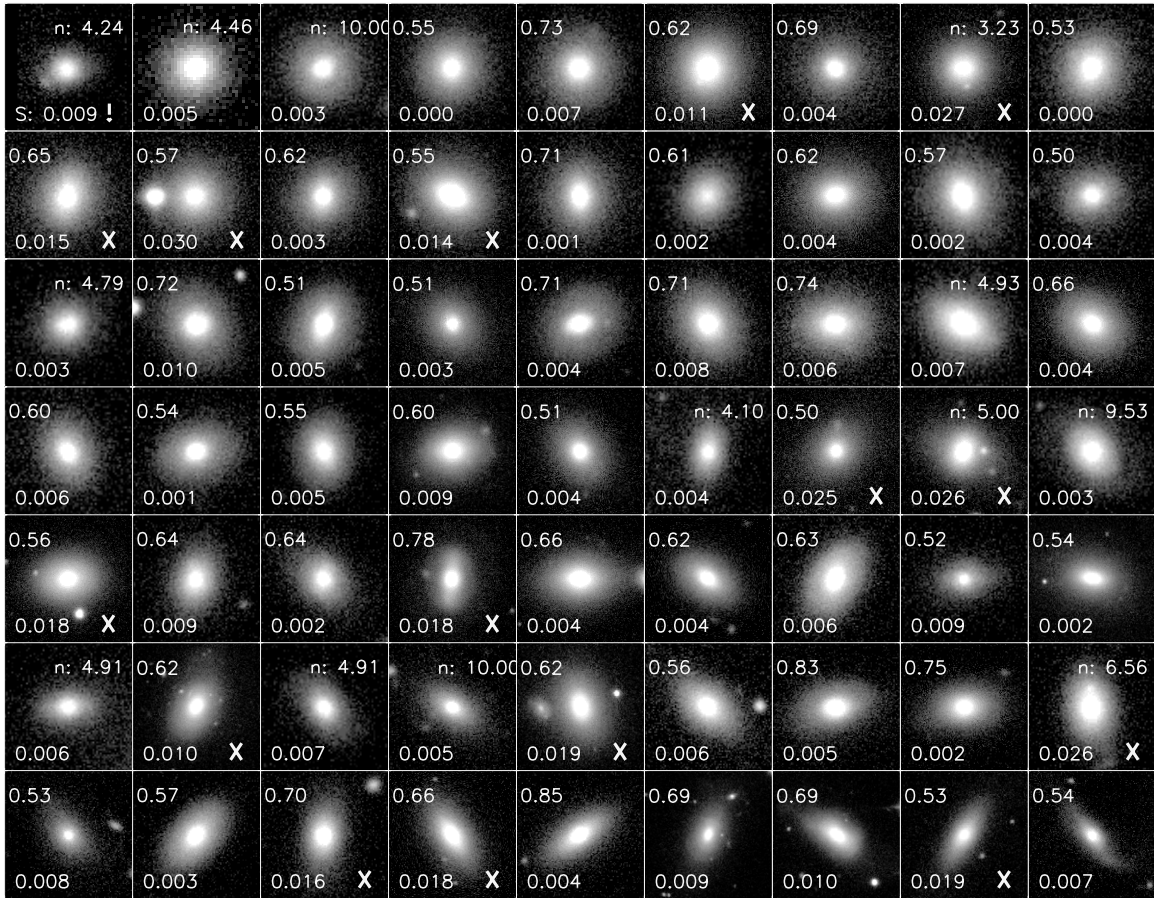
Figure 36. *I*-band postage-stamp images of ZENS galaxies classified as S0s. Galaxies are ordered from top-left to bottom-right by increasing ellipticity. These galaxies are defined to have *I*-band $B/T > 0.5$ (or either *I*-band $n > 2.5$ or $C > 3.3$, when no B/T decomposition is available) and *B*-band smoothness index $S_{B\text{-band}} < 0.01$ (unless faint spiral arms are visible, in which case the galaxy is classified as a bulge-dominated spiral, or, in contrast, the smoothness is evidently boosted by, e.g., bright star-clusters or small companion galaxies, etc., in which case the galaxy is kept in the S0 class). The values of B/T (top left) and smoothness (bottom left) are indicated in the stamps. For those S0 galaxies with no reliable bulge+disk decomposition, we report the value of the corrected Sérsic index or corrected concentration (if also no single-component index n is available; top left). Also in this class there are a few exceptions, which are highlighted with a white $\times$, i.e., galaxies with $S(B) > 0.01$, as for the ellipticals, in 10 out of 13 of which a bright star-cluster/companion is again the reason for the increase in $S_{B\text{-band}}$; in one other case, the boosted value of B smoothness is associated with residuals due to the gaps in the WFI detectors. Two remaining galaxies are moderately inclined systems but do not show any visible dust lane; for this reason they are included in the S0 sample. One galaxy marked with a "*" lies close to the edges of the WFI camera, thus *B*-band observations are available but not the *I*-band ones. The classification for this galaxy is based on the *B*-band parameters.

substantially larger half-light radii from their single-component fits than from their double-component fits. This evidence, and a visual inspection of the data and models, motivated our choice to adopt the double-component half-light radii as our fiducial size estimates in ZENS (Section 4.2.1).

B.2. Validation of the GIM2D Bulge+Disk Models

Caution should be exercised in using blindly the GIM2D double-component results as a number of factors can produce profiles that do not correspond to a meaningful bulge+disk decomposition (see also Allen et al. 2006 for an extensive discussion on this issue). For this reason, all residuals images, models, and profiles obtained from GIM2D were visually inspected to look for possible failure of the fitting algorithm and to identify physically reasonable double-component models. As in Allen et al. (2006), we analyze the radial surface brightness profiles of bulges and disks to identify problematic models which would not be recognized as unphysical by simply looking at the fit χ^2 or at residual images. To this purpose we analyzed the surface-brightness profiles of the bulge and disk along both the semi-major and semi-minor axis; given that the two components can

be twisted by several degrees, this allow us to make a consistent comparison.

For all galaxies for which we attempted a (Sérsic-profile bulge plus exponential-profile disk) decomposition, i.e., all galaxies which are not classified as ellipticals or irregulars, we classify the double-component model fits into the following categories.

1. Bona-fide bulge+disk decompositions. These models have to satisfy the following criteria: the bulge dominates the light in the inner regions and the disk component dominates at large radii; furthermore, the bulge half-light radius has to be smaller than the disk half-light radius. In the *B* and *I* bands, precisely 51% and 61% of the galaxies in our sample fall into this class.

2. Another 20% and 10% of *B* and *I* models are classified as "pure" (bulge-less) disks ($B/T = 0$).

3. For the remaining $\sim$30% of disk galaxies, the bulge+disk decompositions failed to match either of the above categories. We separate a few cases within this class. In about 7% of such galaxies, the bulge component always dominates the surface brightness profile. These models are not necessarily unphysical decompositions: some galaxies that fall in this category have a Sérsic indices $n < 1.5$ and are
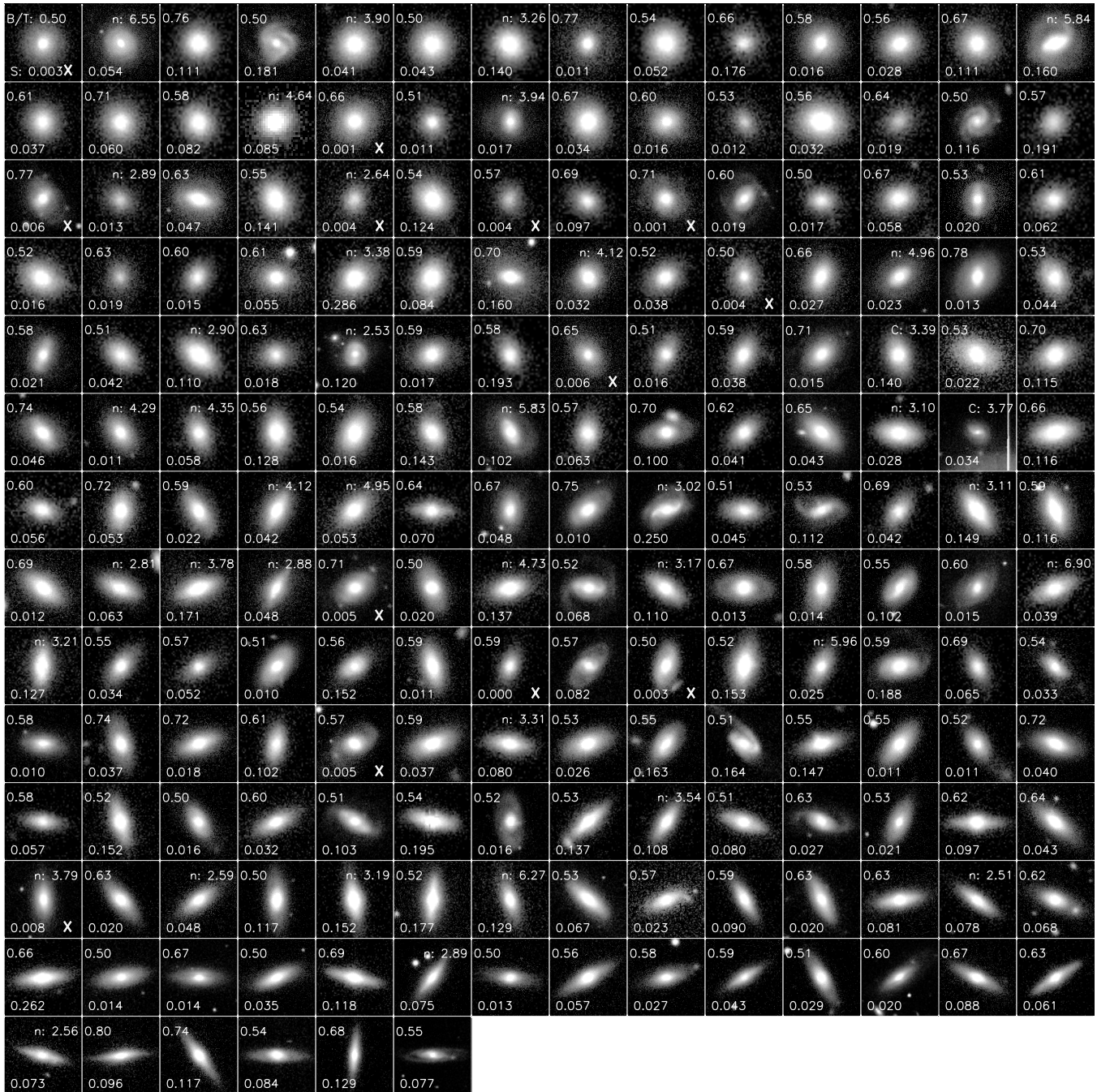
Figure 37. *I*-band postage-stamp images of ZENS galaxies classified as bulge-dominated spiral galaxies. Galaxies are ordered from top-left to bottom-right by increasing ellipticity. These galaxies have *I*-band $B/T > 0.5$ (or *I*-band $n > 2.5$, when no B/T decompositions are available, or $C > 3.3$ if also the latter is missing) and either *B*-band smoothness parameter $S_{B\text{-band}} > 0.01$ or visible spiral arms. Numbers on the stamp are as in Figure 36. The crosses highlight those galaxies which have $S_{B\text{-band}} < 0.01$ but visual inspection reveals faint spiral arms.

simply disk-dominated galaxies. GIM2D hence correctly recovers the information that the structure is dominated by the disk component. Nonetheless the B/T ratio is not considered valid.

We consider instead as truly unphysical those fits ($\sim$23%) which result in a disk half-light radius that is smaller than the bulge's half-light radius and/or in which the disk and bulge profiles are "inverted," i.e., the disk dominates in the inner regions and the bulge dominates in the outer regions. Also unphysical were judged those fits in which the bulge and disk surface brightness radial profiles cross twice (again, see also Allen et al. 2006).

We re-fitted all these problematic cases with the software GALFIT (Peng et al. 2002), which allows for more stringent constraints on the input parameter. As initial guesses for the galaxy sizes, position angles, ellipticity and magnitudes we used the values obtained from SExtractor.

We were able to recover 30% of the previously classified "unphysical" fits. For a total of 19% (*B* band) and 23% (*I* band) of ZENS disk galaxies, however, GALFIT also did not converge to a physical bulge+disk decomposition. The fraction of successful bulge+disk decompositions for each morphological class are summarized in Table 5. The largest formal failure rate is observed for the late-type
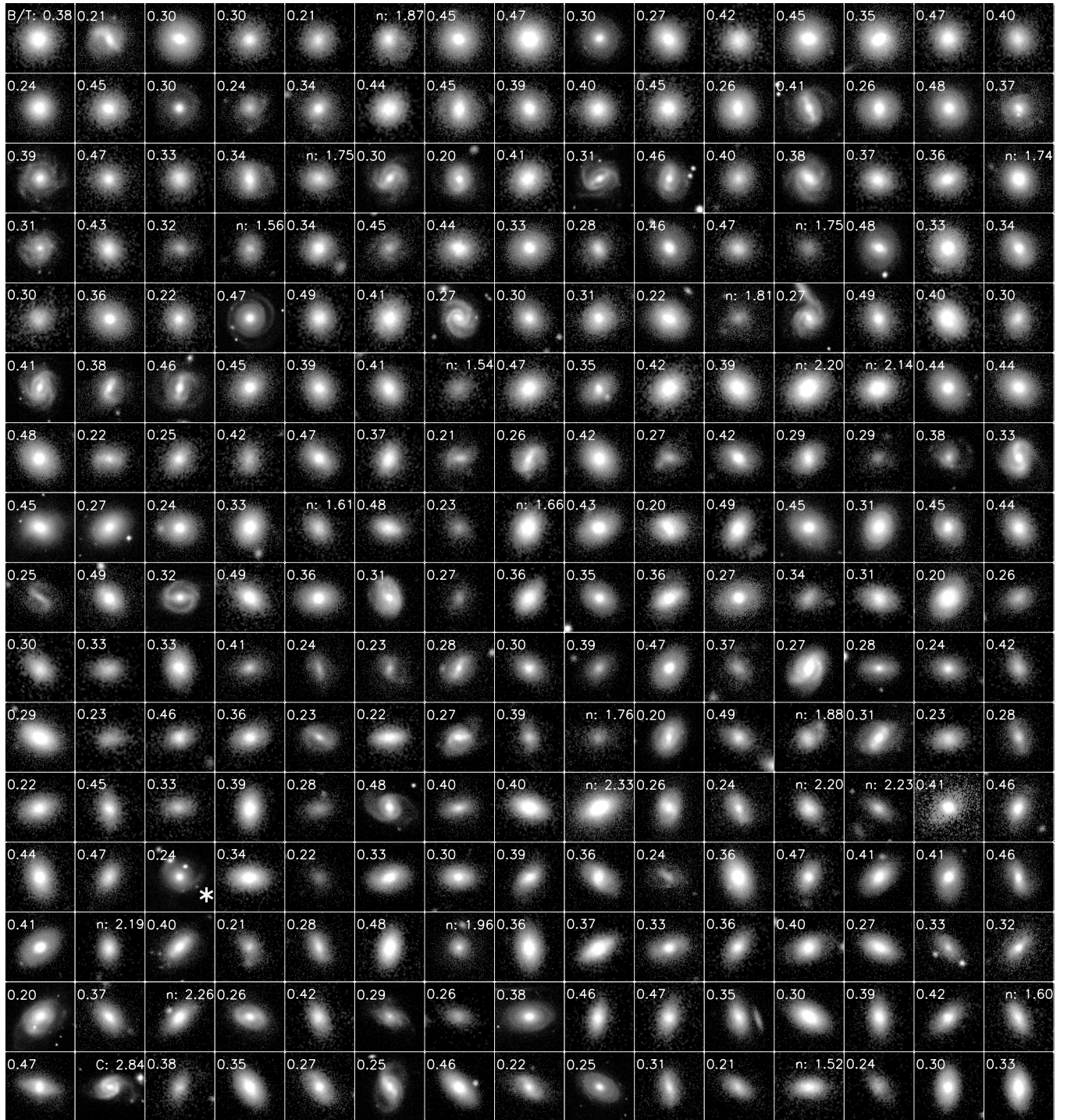
Figure 38. *I*-band postage-stamp images of ZENS galaxies classified as intermediate-type disks. Galaxies are ordered from top-left to bottom-right by increasing ellipticity. To fall into this class, galaxies must have *I*-band $0.2 < B/T < 0.5$ or, alternatively, $1.5 < n < 2.5$, when no valid bulge+disk decomposition is available (or $2.8 < C < 3.3$ if the Sérsic index is also missing). Numbers on the images are the B/T ratios of each galaxy or the Sérsic index (or concentration parameter) when no B/T (and also no n) is available. Stamp images marked with an asterisk are for those galaxies that have low M_{20} indices and thus lie outside the global relations in the bottom panels of Figure 19. One galaxy marked with a "*" lies close to the edges of the WFI camera, thus *B*-band observations are available but not the *I*-band ones. The classification for this galaxy is based on the *B*-band parameters.

disks, as in this case many fit result in a dominating Sérsic-bulge profile with $n < 1.5$, as mentioned before. These are meaningful fits, but not meaningful bulge+disk decompositions; these systems are considered to be single-component, disk-dominated galaxies. Excluding these late-type disks, galaxies that do not have bulge+disk decompositions in

either one or both filters comprise up to ∼20% of the S0-to intermediate-type disk sample.

In ∼17% of galaxies belonging to genuine bulge+disk decompositions, the `GIM2D` fits result in rather elongated bulges ($0.6 < \epsilon < 0.7$). A closer inspection showed that a good fraction
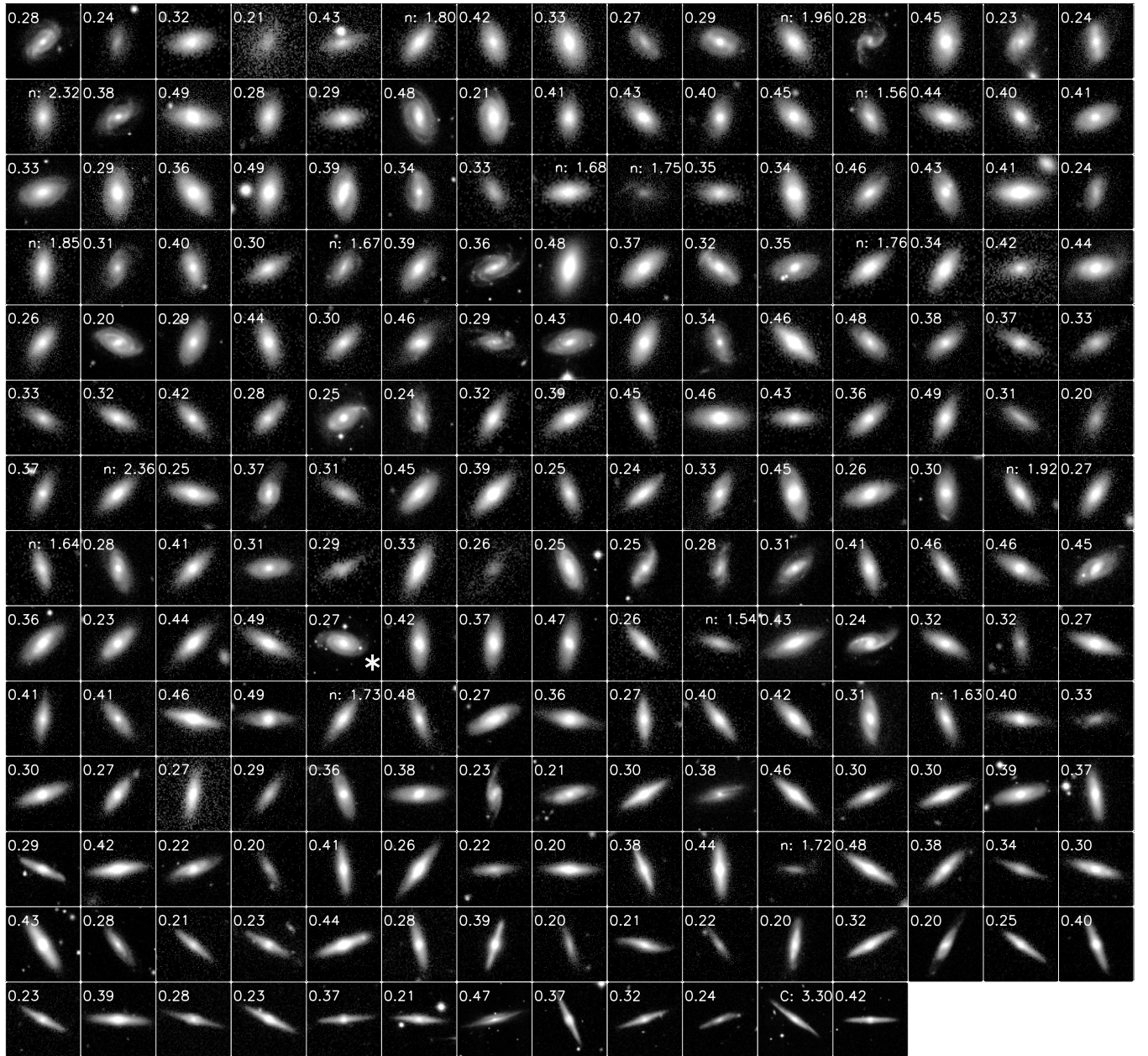
Figure 38. (Continued)

of these models are associated to galaxies classified as barred disks. In a few other cases, a resolved bar is not observed and hence these central structures may either be unresolved bars or truly flattened bulges (although we ourselves wonder whether such distinction is meaningful, not only from a descriptive but also from a physical perspective).

B.3. The Impact on the Bulge+Disk Fits of a Bar Component: Comparisons with Bulge+Disk+Bar Fits

It has been argued that neglecting the bar component when modeling the light profile can affect the best fit parameters and cause an over-estimation of the bulge-to-total ratio of a factor of two to four, and an artificial increase of bulge effective radii (Laurikainen et al. 2005; Gadotti 2008; Weinzirl et al. 2009).

To test the importance of such an effect in our sample, we carried out on those galaxies classified as barred in Section 3.1 a bulge+disk+bar decomposition with the GALFIT software by

modeling the bar with a Sérsic profile having $n < 1$. The addition of a third component can introduce further degrees of degeneracy: applying only broad constraints on the bar structural properties resulted in a high fraction of unphysical models. For this reason we used the results of the ELLIPSE isophotal analysis to constrain the bar structural parameters, when available, and to stick to bulge+disk only fits (without a bar component) for galaxies without this a priori information. Given possible degeneracies between bulge and bar components, when appropriate we will discuss our results with and without those GIM2D fits that result in very elongated bulge components.

Specifically, for galaxies with an ELLIPSE isophotal fits, we used the bar size, ellipticity, and position angle measured in Section 3.1 as initial guesses for the fits. Furthermore we imposed the bar half-light radius to be within $\pm 50\%$ of the size measured with the ELLIPSE method, and at the same time, to be larger than the bulge $r_{1/2}$ and smaller than the
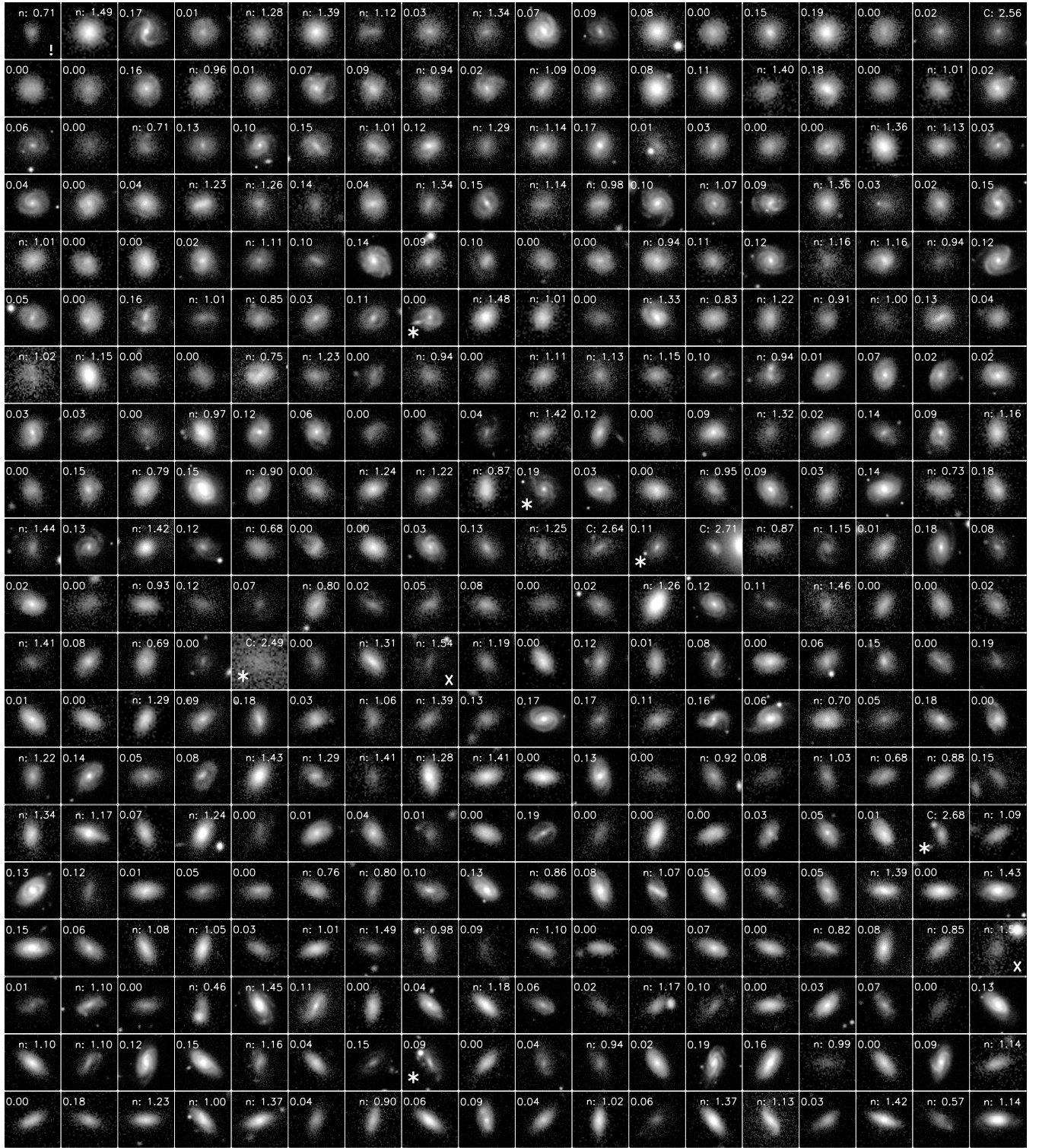
Figure 39. *I*-band postage-stamp images of ZENS galaxies classified as late-type galaxies. Galaxies are ordered from top-left to bottom-right by increasing ellipticity. To fall into this class galaxies must have *I*-band $B/T < 0.2$ or $n < 1.5$ (or $C < 2.8$ if also the Sérsic index is missing) when no valid bulge+disk decomposition is available. As in Figure 38, outliers in the bottom panels of Figure 19 are marked with an asterisk. Two galaxies with high concentration, highlighted with an "X", were kept in this class after further visual inspection.

disk scale length. This avoids the inversion of the disk and bar components or fitting a spurious "nuclear" bar. Likewise, we limited isophotal twists between the bulge and the bar to be within 15° and also imposed a minimum Sérsic index of $n > 1.5$ and a maximum ellipticity of $\epsilon_{bulge} < 0.4$ to the bulge. Extensive tests validated the effectiveness of these constraints, leading to

reliable fits when the extra degrees of freedom introduced by the bar parameters are allowed in the fits.

The results are presented in the top right panels of Figure 27 (red points). Consistently with previous work, comparing the GIM2D B/T ratios with those obtained from the bulge+disk+bar GALFIT fits, we find that the latter tend to be
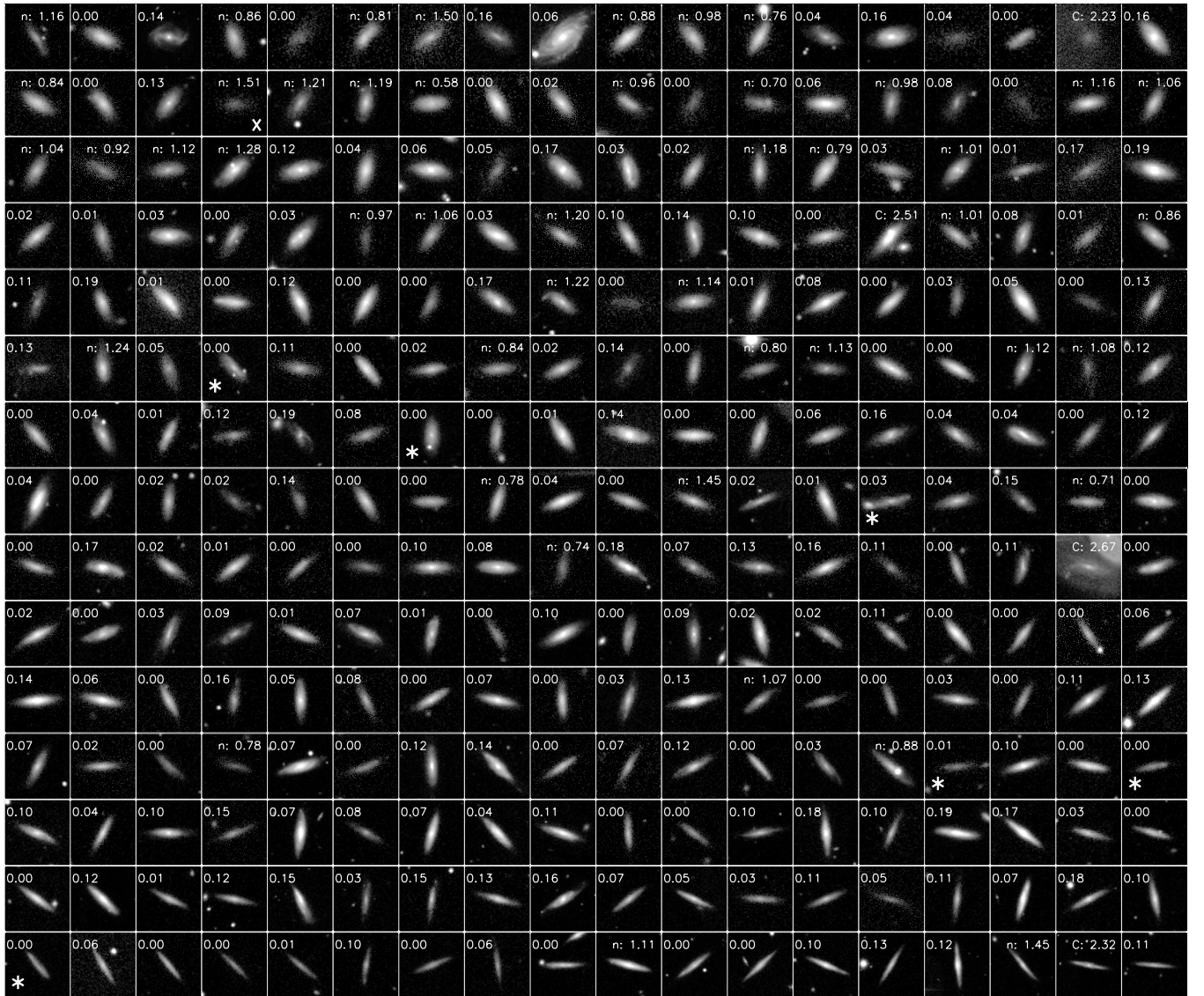
Figure 39. (Continued)

typically smaller, although exceptions are present. Only in ~10% of the cases the difference is of a factor of ~2 or larger. For most of the galaxies, the difference in the final parameters are quite modest, with an average difference of $\Delta B/T = 0.05$. In several cases, fitting a bar also brings the GALFIT B/T values in better agreement with those derived with GIM2D, indicating that the algorithms involved in the derivation of the B/T value in GIM2D are less sensitive to the presence of a bar component. We thus conclude that (1) adding the bar component may no doubt be relevant in some analyses of our barred sample, for which we will utilize the bulge+disk+bar decompositions; (2) the bulge+disk GIM2D fits return generally robust descriptions of these galactic subcomponents, and thus we assume these fits as our fiducial two-component description of the galaxy light distributions.

B.4. A Code versus Code Comparison

We furthermore tested the general consistency between the parameters obtained with bulge+disk fits performed respectively with GALFIT and GIM2D. Specifically, we ran bulge+disk

GALFIT decompositions on all disk galaxies with available GIM2D models (independent of the availability of the ELLIPSE isophotal profiles), and compared with each other the best fit parameters obtained with the two independent codes. This is illustrated in the four panels of Figure 27 (black points) for galaxies with reliable GALFIT and GIM2D fits (see above). The relations shown in the figure are consistent with what we expect from the discussion presented in Section 6.6: the disk scale length is the most robustly determined parameter with little scatter among the two measurements, whereas the bulge structural properties are subject to the largest discrepancies. The B/T ratios obtained by the two codes on average agree reasonably well. The discrepancies observed in B/T in a minority of cases is mostly caused by the differences in the bulge structural parameters. We note that we found a general tendency to associate low Sérsic indices ($n < 1.5$), to the bulge component in the GALFIT fits. This is particularly true for disk-dominated galaxies (these galaxies have single Sérsic indices $n < 1.5$), for which GALFIT often converges to a double component solution with $B/T > 0.4$ but $n < 1.5$. Such bulges furthermore have elongations and sizes similar to that of the disk. In these cases, GIM2D instead produces
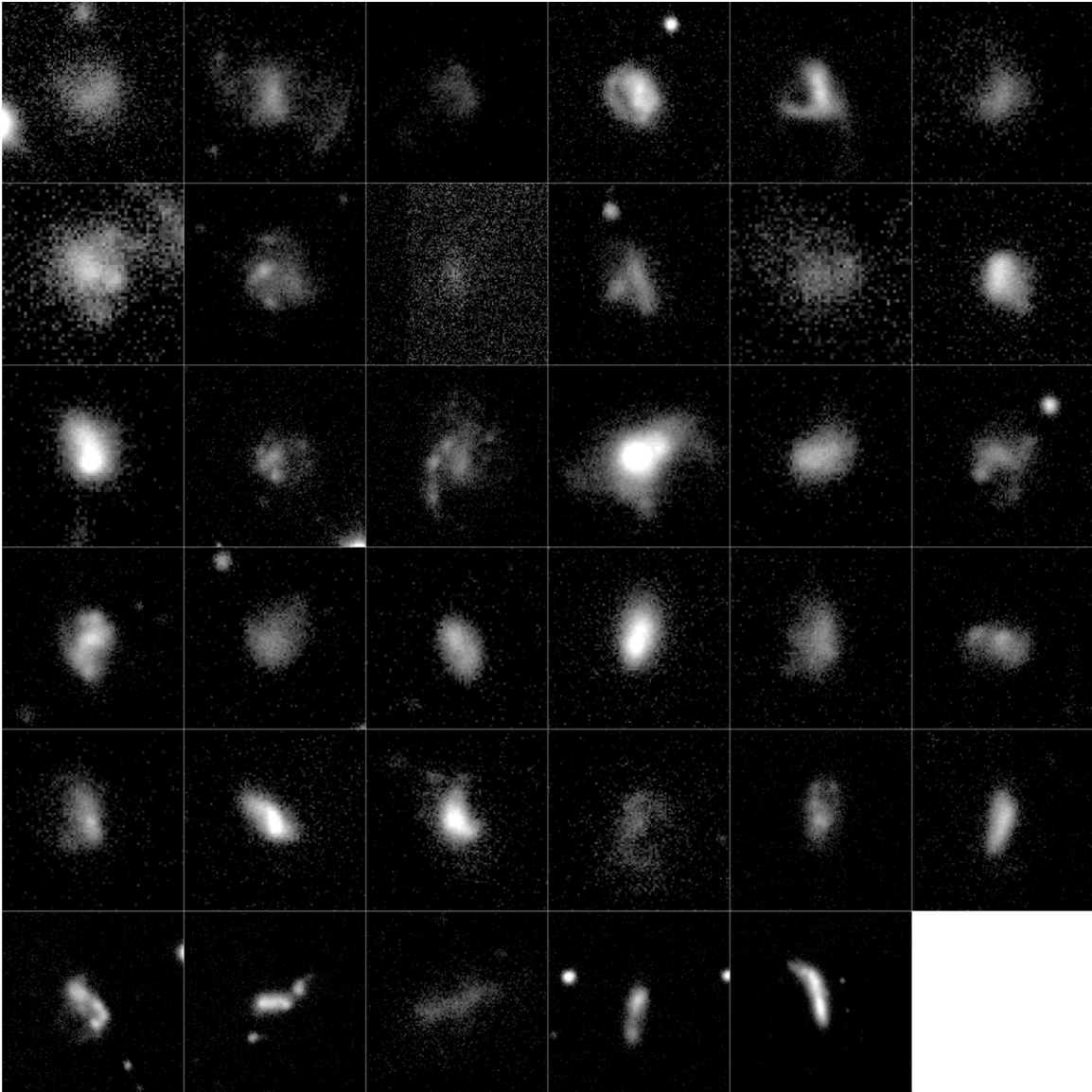
45

Figure 40. *B*-band postage-stamp images of ZENS galaxies classified as irregular/interacting systems. These galaxies were visually identified as systems with disturbed morphologies.

a model that is either a pure disk ($B/T = 0.0$) or very close to it ($B/T < 0.2$). Such GALFIT fits were flagged as not being reliable and are not plotted in Figure 27. In our studies we will adopt as our fiducial bulge+disk decompositions those derived with GIM2D; we flag however in our catalog individual galaxies with substantially different (and yet both formally valid) GIM2D and GALFIT fits so to be able to test our results concerning the properties of bulges and disks against these uncertainties.

B.5. Properties of Galaxies with No Reliable GIM2D Fits

As discussed in Section 4, reliable Sérsic fits and bulge+disk decompositions are not available for some galaxies in our sample (see also Appendix B.2). We inspected whether the galaxies that remained without either or both analytical fits were somehow a biased component of our ZENS sample (apart from having a more complex light distribution on average, as expected). Figure 28 shows the distributions of galaxy masses and *I*-band half-light radii for such galaxies with no GIM2D models. For galaxies without any (single- and double-component) size

measurements, we use the ZEST+ radii, *corrected* as described in Section 6.3. To establish the presence/absence of possible biases, we also show the global distributions of masses and sizes of galaxies with reliable analytical fits for comparison. A summary of the fraction of failed models for each morphological type is given in Table 5.

Galaxies with no single Sérsic fits tend to populate the high mass/radius tail of the distributions and their incidence is highest for intermediate-type disks. For these galaxies we will use in our ZENS analyses the corrected ZEST+ sizes, which, on the remaining galaxies, we have shown to be in excellent agreement with the (corrected) sizes derived from the analytical fits. Only 4% of galaxies are in this category. We hence reckon that the impact on the final results will be in negligible any case. Although the overall success of the bulge+disk decompositions is lower than the success rate of the single-component fits (see Table 5), galaxies with no bulge and disk parameters are more uniformly distributed in mass and size relative to the global ZENS population. It is thus reasonable to assume that the
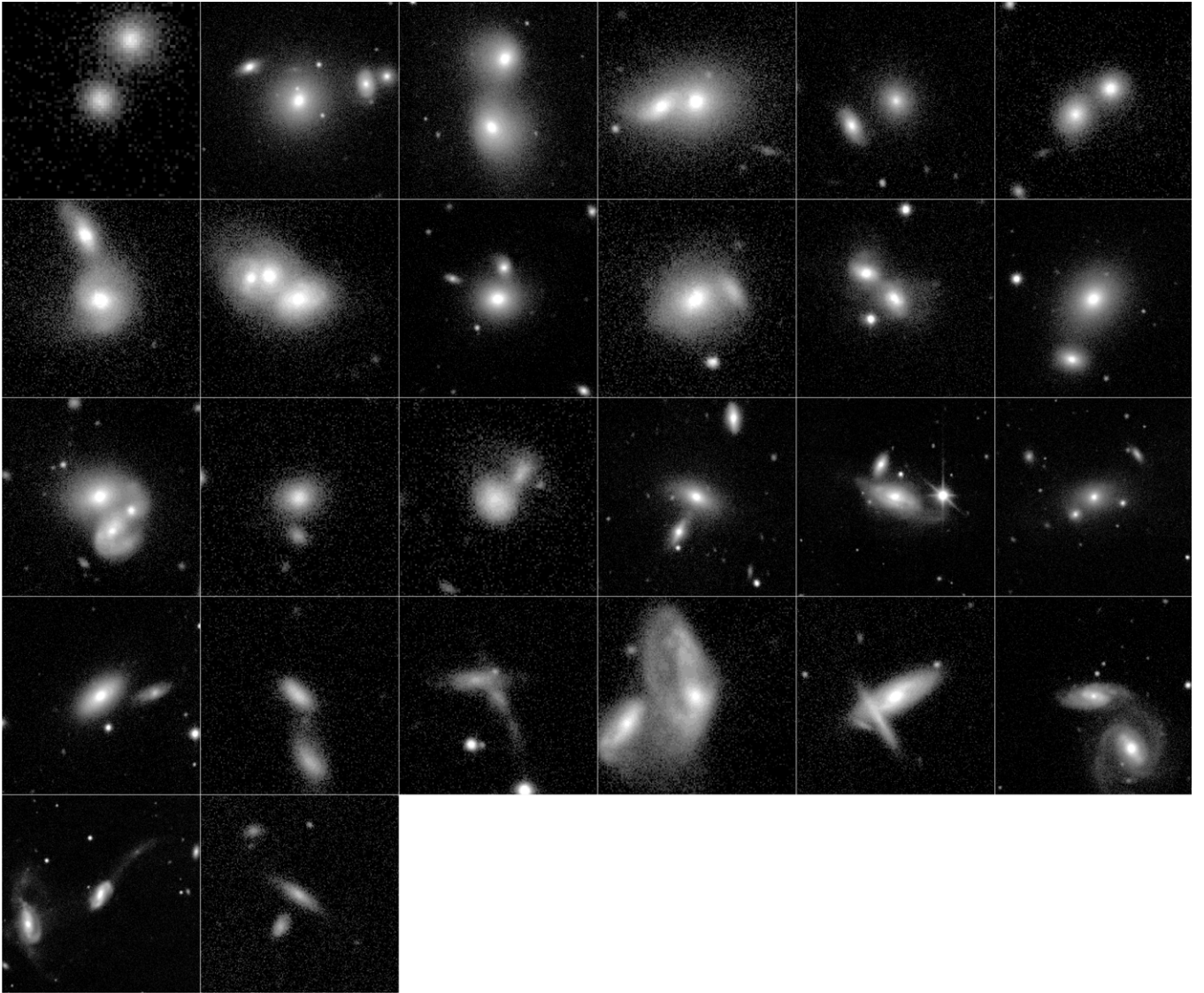
Figure 41. *I*-band postage-stamp images of the ZENS galaxy-pairs that are plausibly undergoing a merger.

exclusion of these galaxies from analysis based on bulge/disk parameters will lower the statistical significance of the results, but should not introduce strong biases.

APPENDIX C

CORRECTION MAPS FOR SIZES AND MAGNITUDES: VARIATIONS WITH PSF SIZE AND ROBUSTNESS TOWARD CONTAMINANTS

C.1. Correction Maps Obtained for the Best and Worst PSF

Correction maps for sizes and magnitudes, similar to those shown in the main text in Section 6 for the median PSF-FWHM of the ZENS WFI *I* images, are shown here for the two "bracketing"—i.e., the best and the worst—PSF FWHM values in our data set. A comparison of the corresponding correction maps derived for the three different PSF sizes clearly shows the major impact of PSF-blurring in the (uncorrected) structural measurements. The implementation of our correction maps rends all measurements comparable onto a consistently calibrated grid.

C.2. The Effect of Contaminants on the Derivation of the Corrections

As commented in Section 6 for the ZEST+ measurements, there are regions of the observed C-ϵ-mag-$r_{1/2}$ hyper-plane that are highly degenerate: they can be populated by models with intrinsic parameters that originate in that same region of parameter space, as well as by models with very different "intrinsic" ellipticity or concentration, which are scattered into that given bin by observational errors. It is thus important to verify that the size and magnitude corrections that we infer in these regions of parameter space are not strongly dependent on the precise way in which we populate the input grid of simulated models. If this were the case and without a priori knowledge of the relative fraction of the two populations in the real Universe, the derivation of the corrections in the parameter space would be affected by biases introduced by the precise choice of the simulation grid. To assess whether our corrections suffer from this problem, we calculated the corrections in these "troublesome" grid points by using only those models with original, intrinsic $\epsilon - C$ values in that same bin, and, for comparison, using only models that were

originated in a different $\epsilon - C$ bin and were scattered into that bin by measurement errors. In many cases we found that both model samples gave consistent results for the corrections to the magnitude and sizes, which we could then use for our real galaxies. This is illustrated in Figure 33 for the lowest ellipticity bin, which is also the one with the highest contamination, and for models convolved with the typical I-band PSF. The corrections derived with the two sub samples are reassuringly very similar over a wide arc of size–magnitude space (and thus very similar to the global corrections presented in Figure 9). We therefore argue that our implementation of the correction scheme of Section 6.3 is free from biases introduced by the choice of the simulation grid.

APPENDIX D

ZENS GALAXIES SPLIT IN THEIR MORPHOLOGICAL CLASSES

Finally, we show the postage-stamp images of the ZENS galaxies, split according to their morphological type. The relevant structural parameters characterizing each type are indicated on top of each stamp image. The $n > 3$ single-component profiles that *define* our elliptical galaxy samples are also shown.

REFERENCES

Abazajian, K. N., Adelman-McCarthy, J. K., Agüeros, M. A., et al. 2009, ApJS, 182, 543
Abraham, R. G., & Merrifield, M. R. 2000, AJ, 120, 2835
Abraham, R. G., Merrifield, M. R., Ellis, R. S., Tanvir, N. R., & Brinchmann, J. 1999, MNRAS, 308, 569
Abraham, R. G., Tanvir, N. R., Santiago, B. X., et al. 1996, MNRAS, 279, L47
Abraham, R. G., van den Bergh, S., & Nair, P. 2003, ApJ, 588, 218
Aguerri, J. A. L., Méndez-Abreu, J., & Corsini, E. M. 2009, A&A, 495, 491
Allen, P. D., Driver, S. P., Graham, A. W., et al. 2006, MNRAS, 371, 2
Bailin, J., & Harris, W. E. 2008, ApJ, 681, 225
Balcells, M., Graham, A. W., Domínguez-Palmero, L., & Peletier, R. F. 2003, ApJL, 582, L79
Baldry, I. K., Balogh, M. L., Bower, R. G., et al. 2006, MNRAS, 373, 469
Balogh, M. L., Morris, S. L., Yee, H. K. C., Carlberg, R. G., & Ellingson, E. 1997, ApJL, 488, L75
Bamford, S. P., Nichol, R. C., Baldry, I. K., et al. 2009, MNRAS, 393, 1324
Barazza, F. D., Jogee, S., & Marinova, I. 2008, ApJ, 675, 1194
Barden, M., Rix, H.-W., Somerville, R. S., et al. 2005, ApJ, 635, 959
Barnes, J. E. 1988, ApJ, 331, 699
Beckman, J. E., Peletier, R. F., Knapen, J. H., Corradi, R. L. M., & Gentet, L. J. 1996, ApJ, 467, 175
Bekki, K., Couch, W. J., & Shioya, Y. 2002, ApJ, 577, 651
Bender, R., Doebereiner, S., & Moellenhoff, C. 1988, A&AS, 74, 385
Benítez, N., Ford, H., Bouwens, R., et al. 2004, ApJS, 150, 1
Bernardi, M., Shankar, F., Hyde, J. B., et al. 2010, MNRAS, 404, 2087
Bernstein, R. A., Freedman, W. L., & Madore, B. F. 2002a, ApJ, 571, 56
Bernstein, R. A., Freedman, W. L., & Madore, B. F. 2002b, ApJ, 571, 107
Bertin, E., & Arnouts, S. 1996, A&AS, 117, 393
Blanton, M. R., & Berlind, A. A. 2007, ApJ, 664, 791
Blanton, M. R., Hogg, D. W., Bahcall, N. A., et al. 2003, ApJ, 594, 186
Blanton, M. R., Schlegel, D. J., Strauss, M. A., et al. 2005, AJ, 129, 2562
Buta, R., Vasylyev, S., Salo, H., & Laurikainen, E. 2005, AJ, 130, 506
Byun, Y. I., Freeman, K. C., & Kylafis, N. D. 1994, ApJ, 432, 114
Cameron, E., Carollo, C. M., Oesch, P., et al. 2010, MNRAS, 409, 346
Cameron, E., & Driver, S. P. 2007, MNRAS, 377, 523
Cameron, E., & Driver, S. P. 2009, A&A, 493, 489
Caon, N., Capaccioli, M., & D'Onofrio, M. 1993, MNRAS, 265, 1013
Cardelli, J. A., Clayton, G. C., & Mathis, J. S. 1989, ApJ, 345, 245
Carollo, C. M. 1999, ApJ, 523, 566
Carollo, C. M., Bschorr, T. J., Renzini, A., et al. 2013a, ApJ, 773, 112
Carollo, C. M., Cibinel, A., Lilly, S. J., et al. 2013b, ApJ, in press (Paper I)
Carollo, C. M., Danziger, I. J., Rich, R. M., & Chen, X. 1997a, ApJ, 491, 545
Carollo, C. M., Franx, M., Illingworth, G. D., & Forbes, D. A. 1997b, ApJ, 481, 710

Carollo, C. M., Scarlata, C., Stiavelli, M., Wyse, R. F. G., & Mayer, L. 2007, ApJ, 658, 960
Carollo, C. M., Stiavelli, M., & Mack, J. 1998, AJ, 116, 68
Carollo, C. M., Stiavelli, M., de Zeeuw, P. T., & Mack, J. 1997c, AJ, 114, 2366
Carollo, C. M., Stiavelli, M., de Zeeuw, P. T., Seigar, M., & Dejonghe, H. 2001, ApJ, 546, 216
Cibinel, A., Carollo, C. M., Lilly, S. J., et al. 2013, ApJ, in press (Paper III)
Colless, M., Dalton, G., Maddox, S., et al. 2001, MNRAS, 328, 1039
Colless, M., Peterson, B. A., Jackson, C., et al. 2003, arXiv:astro-ph/0306581
Combes, F., Debbasch, F., Friedli, D., & Pfenniger, D. 1990, A&A, 233, 82
Conselice, C. J. 2003, ApJS, 147, 1
Cooper, M. C., Newman, J. A., Madgwick, D. S., et al. 2005, ApJ, 634, 833
Côté, P., Ferrarese, L., Jordán, A., et al. 2007, ApJ, 671, 1456
Courteau, S., de Jong, R. S., & Broeils, A. H. 1996, ApJL, 457, L73
Cunow, B. 2001, MNRAS, 323, 130
Debattista, V. P., Carollo, C. M., Mayer, L., & Moore, B. 2004, ApJL, 604, L93
Debattista, V. P., Mayer, L., Carollo, C. M., et al. 2006, ApJ, 645, 209
de Jong, R. S. 1996, A&AS, 118, 557
Dekel, A., Birnboim, Y., Engel, G., et al. 2009a, Natur, 457, 451
Dekel, A., Sari, R., & Ceverino, D. 2009b, ApJ, 703, 785
De Propris, R., Colless, M., Driver, S. P., et al. 2003, MNRAS, 342, 725
de Souza, R. E., Gadotti, D. A., & dos Anjos, S. 2004, ApJS, 153, 411
de Vaucouleurs, G. 1963, ApJS, 8, 31
Disney, M. J. 1976, Natur, 263, 573
Dressler, A. 1980, ApJ, 236, 351
Driver, S. P., Popescu, C. C., Tuffs, R. J., et al. 2007, MNRAS, 379, 1022
Driver, S. P., Popescu, C. C., Tuffs, R. J., et al. 2008, ApJL, 678, L101
Eke, V. R., Baugh, C. M., Cole, S., et al. 2004a, MNRAS, 348, 866
Eke, V. R., Frenk, C. S., Baugh, C. M., et al. 2004b, MNRAS, 355, 769
Einasto, M., Einasto, J., Tago, E., et al. 2007, A&A, 464, 815
Erwin, P. 2005, MNRAS, 364, 283
Fall, S. M., & Efstathiou, G. 1980, MNRAS, 193, 189
Feldmann, R., Carollo, C. M., Porciani, C., et al. 2006, MNRAS, 372, 565
Feldmann, R., Mayer, L., & Carollo, C. M. 2008, ApJ, 684, 1062
Ferrarese, L., van den Bosch, F. C., Ford, H. C., Jaffe, W., & O'Connell, R. W. 1994, AJ, 108, 1598
Fisher, D. B., & Drory, N. 2008, AJ, 136, 773
Forbes, D. A., & Thomson, R. C. 1992, MNRAS, 254, 723
Franx, M., Illingworth, G., & Heckman, T. 1989, AJ, 98, 538
Fukugita, M., Shimasaku, K., & Ichikawa, T. 1995, PASP, 107, 945
Gadotti, D. A. 2008, MNRAS, 384, 420
Gallazzi, A., Bell, E. F., Wolf, C., et al. 2009, ApJ, 690, 1883
Goto, T., Yamauchi, C., Fujita, Y., et al. 2003, MNRAS, 346, 601
Graham, A. W. 2001, AJ, 121, 820
Graham, A. W., & Driver, S. P. 2005, PASA, 22, 118
Graham, A. W., Driver, S. P., Petrosian, V., et al. 2005, AJ, 130, 1535
Graham, A. W., Erwin, P., Trujillo, I., & Asensio Ramos, A. 2003, AJ, 125, 2951
Graham, A. W., & Guzmán, R. 2003, AJ, 125, 2936
Graham, A. W., & Worley, C. C. 2008, MNRAS, 388, 1708
Guo, Y., McIntosh, D. H., Mo, H. J., et al. 2009, MNRAS, 398, 1129
Hambly, N. C., MacGillivray, H. T., Read, M. A., et al. 2001, MNRAS, 326, 1279
Hansen, S. M., Sheldon, E. S., Wechsler, R. H., & Koester, B. P. 2009, ApJ, 699, 1333
Häussler, B., McIntosh, D. H., Barden, M., et al. 2007, ApJS, 172, 615
Hogg, D. W., Blanton, M. R., Eisenstein, D. J., et al. 2003, ApJL, 585, L5
Hopkins, P. F., Cox, T. J., Dutta, S. N., et al. 2009, ApJS, 181, 135
Immeli, A., Samland, M., Gerhard, O., & Westera, P. 2004, A&A, 413, 547
Impey, C., & Bothun, G. 1997, ARA&A, 35, 267
Janowiecki, S., Mihos, J. C., Harding, P., et al. 2010, ApJ, 715, 972
Jedrzejewski, R. I. 1987, MNRAS, 226, 747
Kauffmann, G., Heckman, T. M., White, S. D. M., et al. 2003, MNRAS, 341, 54
Kawata, D., Mulchaey, J. S., Gibson, B. K., & Sánchez-Blázquez, P. 2006, ApJ, 648, 969
Kimm, T., Somerville, R. S., Yi, S. K., et al. 2009, MNRAS, 394, 1131
Knapen, J. H., Shlosman, I., & Peletier, R. F. 2000, ApJ, 529, 93
Knobel, C., Lilly, S. J., Kovac, K., et al. 2013, ApJ, 769, 24
Kormendy, J. 1979, ApJ, 227, 714
Kormendy, J., Fisher, D. B., Cornell, M. E., & Bender, R. 2009, ApJS, 182, 216
Kormendy, J., & Kennicutt, R. C., Jr. 2004, ARA&A, 42, 603
Kron, R. G. 1980, ApJS, 43, 305
Lackner, C. N., & Gunn, J. E. 2012, MNRAS, 421, 2277
Landolt, A. U. 1992, AJ, 104, 340
Lauer, T. R., Ajhar, E. A., Byun, Y.-I., et al. 1995, AJ, 110, 2622
Laurikainen, E., Salo, H., & Buta, R. 2005, MNRAS, 362, 1319

Laurikainen, E., Salo, H., Buta, R., & Knapen, J. H. 2007, MNRAS, 381, 401
Lewis, I., Balogh, M., De Propris, R., et al. 2002, MNRAS, 334, 673
Lintott, C. J., Schawinski, K., Slosar, A., et al. 2008, MNRAS, 389, 1179
Lotz, J. M., Primack, J., & Madau, P. 2004, AJ, 128, 163
Mahajan, S., & Raychaudhury, S. 2009, MNRAS, 400, 687
Malin, D. F., & Carter, D. 1980, Natur, 285, 643
Malin, D. F., & Carter, D. 1983, ApJ, 274, 534
Maller, A. H., Berlind, A. A., Blanton, M. R., & Hogg, D. W. 2009, ApJ, 691, 394
Marleau, F. R., & Simard, L. 1998, ApJ, 507, 585
Meert, A., Vikram, V., & Bernardi, M. 2013, MNRAS, 433, 1344
Menéndez-Delmestre, K., Sheth, K., Schinnerer, E., Jarrett, T. H., & Scoville, N. Z. 2007, ApJ, 657, 790
Mihos, J. C., & Hernquist, L. 1994, ApJL, 437, L47
Mihos, J. C., & Hernquist, L. 1996, ApJ, 464, 641
Möllenhoff, C., Popescu, C. C., & Tuffs, R. J. 2006, A&A, 456, 941
Mosleh, M., Williams, R. J., & Franx, M. 2013, arXiv:1302.6240
Muldrew, S. I., Croton, D. J., Skibba, R. A., et al. 2012, MNRAS, 419, 2670
Naab, T., & Burkert, A. 2003, ApJ, 597, 893
Naab, T., Burkert, A., & Hernquist, L. 1999, ApJL, 523, L133
Nair, P. B., & Abraham, R. G. 2010a, ApJS, 186, 427
Nair, P. B., & Abraham, R. G. 2010b, ApJL, 714, L260
Noordermeer, E., van der Hulst, J. M., Sancisi, R., Swaters, R. A., & van Albada, T. S. 2005, A&A, 442, 137
Norberg, P., Cole, S., Baugh, C. M., et al. 2002, MNRAS, 336, 907
Norman, C. A., Sellwood, J. A., & Hasan, H. 1996, ApJ, 462, 114
Oesch, P. A., Carollo, C. M., Feldmann, R., et al. 2010, ApJL, 714, L47
Oke, J. B. 1974, ApJS, 27, 21
Pannella, M., Hopp, U., Saglia, R. P., et al. 2006, ApJL, 639, L1
Peng, C. Y., Ho, L. C., Impey, C. D., & Rix, H.-W. 2002, AJ, 124, 266
Peng, Y., Lilly, S. J., Renzini, A., & Carollo, M. 2012, ApJ, 757, 4
Peng, Y.-j., Lilly, S. J., Kovač, K., et al. 2010, ApJ, 721, 193
Porter, S. C., Raychaudhury, S., Pimbblet, K. A., & Drinkwater, M. J. 2008, MNRAS, 388, 1152
Refregier, A. 2003, MNRAS, 338, 35
Rix, H.-W., Barden, M., Beckwith, S. V. W., et al. 2004, ApJS, 152, 163
Sage, L. J., & Welch, G. A. 2006, ApJ, 644, 850
Saglia, R. P., Bertschinger, E., Baggley, G., et al. 1993, MNRAS, 264, 961
Scarlata, C., Carollo, C. M., Lilly, S., et al. 2007, ApJS, 172, 406

Schlegel, D. J., Finkbeiner, D. P., & Davis, M. 1998, ApJ, 500, 525
Schweizer, F. 1979, ApJ, 233, 23
Schweizer, F., Seitzer, P., Faber, S. M., et al. 1990, ApJL, 364, L33
Scodeggio, M., Gavazzi, G., Franzetti, P., et al. 2002, A&A, 384, 812
Scoville, N., Aussel, H., Brusa, M., et al. 2007, ApJS, 172, 1
Sersic, J. L. 1968, Atlas de Galaxies Australes (Cordoba: Observatorio Astronomico)
Shao, Z., Xiao, Q., Shen, S., et al. 2007, ApJ, 659, 1159
Shen, S., Mo, H. J., White, S. D. M., et al. 2003, MNRAS, 343, 978
Sheth, K., Elmegreen, D. M., Elmegreen, B. G., et al. 2008, ApJ, 675, 1141
Simard, L., Willmer, C. N. A., Vogt, N. P., et al. 2002, ApJS, 142, 1
Tal, T., van Dokkum, P. G., Nelan, J., & Bezanson, R. 2009, AJ, 138, 1417
Toomre, A. 1977, Evolution of Galaxies and Stellar Populations (New Haven, CT: Yale Univ. Observatory), 401
Trujillo, I., Aguerri, J. A. L., Cepa, J., & Gutiérrez, C. M. 2001, MNRAS, 328, 977
Trujillo, I., Erwin, P., Asensio Ramos, A., & Graham, A. W. 2004, AJ, 127, 1917
Tuffs, R. J., Popescu, C. C., Völk, H. J., Kylafis, N. D., & Dopita, M. A. 2004, A&A, 419, 821
van den Bosch, F. C., Aquino, D., Yang, X., et al. 2008, MNRAS, 387, 79
van der Wel, A. 2008, ApJL, 675, L13
van Dokkum, P. G. 2005, AJ, 130, 2647
van Gorkom, J. H., Schechter, P. L., & Kristian, J. 1987, ApJ, 314, 457
Vulcani, B., Poggianti, B. M., Aragón-Salamanca, A., et al. 2011, MNRAS, 412, 246
Weinmann, S. M., Kauffmann, G., van den Bosch, F. C., et al. 2009, MNRAS, 394, 1213
Weinmann, S. M., van den Bosch, F. C., Yang, X., & Mo, H. J. 2006, MNRAS, 366, 2
Weinzirl, T., Jogee, S., Khochfar, S., Burkert, A., & Kormendy, J. 2009, ApJ, 696, 411
White, S. D. M., & Rees, M. J. 1978, MNRAS, 183, 341
Whitmore, B. C., & Gilmore, D. M. 1991, ApJ, 367, 64
Whitmore, B. C., Gilmore, D. M., & Jones, C. 1993, ApJ, 407, 489
Wilman, D. J., Oemler, A., Jr., Mulchaey, J. S., et al. 2009, ApJ, 692, 298
Wilman, D. J., Zibetti, S., & Budavári, T. 2010, MNRAS, 406, 1701
Woo, J., Dekel, A., Faber, S. M., et al. 2013, MNRAS, 428, 3306
Wyse, R. F. G., Gilmore, G., & Franx, M. 1997, ARA&A, 35, 637
York, D. G., Adelman, J., Anderson, J. E., Jr., et al. 2000, AJ, 120, 1579
Zamojski, M. A., Schiminovich, D., Rich, R. M., et al. 2007, ApJS, 172, 468